

**Centro de Investigación Científica y de Educación  
Superior de Ensenada, Baja California**



---

**Doctorado en Ciencias  
en Ciencias de la Tierra  
con orientación en Geofísica Aplicada**

---

**Merging land and marine controlled-source electromagnetic  
methods and a physical model for the elusive airwave**

Tesis  
para cubrir parcialmente los requisitos necesarios para obtener el grado de  
Doctor en Ciencias

Presenta:

**Armando Calderón Moctezuma**

Ensenada, Baja California, México  
2017

Tesis defendida por  
**Armando Calderón Moctezuma**

y aprobada por el siguiente Comité

---

**Dr. Luis Alonso Gallardo Delgado**  
Codirector de Tesis

---

**Dr. Enrique Gómez Treviño**  
Codirector de Tesis

**Dr. Jonás de Dios De Basabe Delgado**

**Dr. Antonio González Fernández**

**Dr. Peter Wolfgram**



---

**Dr. Juan García Abdeslem**  
Coordinador del Posgrado en Ciencias de la Tierra

---

**Dra. Rufina Hernández Martínez**  
Directora de Estudios de Posgrado

Resumen de la tesis que presenta **Armando Calderón Moctezuma** como requisito parcial para la obtención del grado de Doctor en Ciencias de la Tierra con orientación en Geofísica Aplicada.

## **Unificando los métodos electromagnéticos marinos y terrestres de fuente controlada y un modelo físico para la elusiva onda de aire.**

Resumen aprobado por:

---

Dr. Enrique Gómez Treviño  
Codirector de Tesis

---

Dr. Luis Alonso Gallardo Delgado  
Codirector de Tesis

La reciente aplicación de los métodos electromagnéticos de fuente controlada (CSEM) en ambientes marinos para detectar depósitos de hidrocarburos ha desatado una gran cantidad de investigaciones sobre el tema. Muchas de estas investigaciones han evolucionado independientemente de los primeros desarrollos de CSEM en tierra. En particular, se han introducido nuevos conceptos para tener en cuenta los efectos producidos por la presencia del mar. Tal es el caso de la onda de aire, que presumiblemente dificulta la detección de depósitos de hidrocarburos en aguas someras. Este concepto en particular ha creado confusión en la literatura. El objetivo del presente trabajo es demostrar que los datos CSEM terrestres y marinos coinciden en un punto de encuentro en cero profundidad de agua. El análisis separa las contribuciones del mar y del subsuelo usando una integral en el dominio de la profundidad. Las contribuciones relativas del mar y del subsuelo son inspeccionadas, tanto lateral como verticalmente, para todas las separaciones relevantes entre la fuente y el receptor, así como para diferentes profundidades del piso marino y para cuando el mar desaparece. Se halló que las clásicas cuatro zonas identificadas en los datos de CSEM marino también se encuentran presentes en los datos de CSEM de tierra y que existe una transición suave. En función de la distancia de la fuente las cuatro zonas aparecen como sigue. Primero se manifiestan los efectos de corriente directa, que son compartidos tanto por el mar como por el subsuelo. Después continúa la zona de inducción que es dominada por las contribuciones de las formaciones subyacentes. La tercera zona, la cual corresponde a la onda de aire es dominada en gran medida por las contribuciones del mar. En esta zona la contribución del subsuelo es pequeña, pero esto ocurre porque hay contribuciones positivas y negativas que tienden a cancelarse mutuamente. La cuarta y última zona es una asintótica onda plana. En general se observa que el efecto de la capa resistiva crece para aguas poco profundas, mientras que el efecto del mar no lo hace. Este efecto de mar es nulo cuando los métodos de CSEM marino y terrestres se encuentran a una profundidad de cero metros. Esto más adelante es ilustrado identificando la onda de aire con la densidad superficial de carga en la superficie del mar a medida que este disminuye.

**Palabras clave:** CSEM, Electromagnéticos de fuente controlada, onda de aire, detectabilidad, separación de campos.

Abstract of the thesis presented by **Armando Calderón Moctezuma** as a partial requirement to obtain the Doctor of Science degree in Earth Sciences with orientation in Applied Geophysics

## **Merging land and marine controlled-source electromagnetic methods and a physical model for the elusive airwave**

Abstract approved by:

---

Dr. Enrique Gómez Treviño  
Thesis Co-director

---

Dr. Luis Alonso Gallardo Delgado  
Thesis Co-director

The recent application of controlled-source electromagnetic (CSEM) methods in marine environments to detect hydrocarbon reservoirs has resulted in an increased amount of research on the subject. Many of these investigations have grown independently from the earlier developments in land CSEM. In particular, new concepts have been introduced to account for special effects produced by the presence of the sea, which were unheard of in the early developments. Such is the case of the airwave that presumably hampers the detection of hydrocarbon reservoirs in shallow waters. This concept in particular has created confusion in the literature. The objective of the present work is to show that land and marine CSEM merge at their meeting point of zero water depth. The analysis splits the marine CSEM data into sea and sub-seafloor contributions in the marine CSEM data using an integral representation over the depth domain. The relative contributions from the sea and from the sub-seafloor obtained from the splitting are inspected, both laterally and vertically, for all the relevant offsets or separations between source and receiver, for several water depths to no sea at all. It was found that all of the four classical zones identified in marine CSEM data are already present in land CSEM data, and that there is a smooth transition between them. As a function of offsets, the four zones are as follows. Firstly, for short offsets the direct-current effects, which are shared by both the sea and the sub-seafloor. The induction zone is next and is dominated by contributions from the underlying formations. The third zone, which corresponds to the airwave, is largely dominated by contributions from the sea. The overall contribution from the sub-seafloor is small in this zone but this is because there are positive and negative contributions that tend to cancel each other. The fourth and last zone is an asymptotic plane-wave. In general, it is observed that the effect of the resistive layer grows for shallow waters confirms a recent finding; however, the effect of the sea as also growing is not. The effect of the sea is nil at the meeting point at zero water depth for land and marine CSEM. This is further illustrated by identifying the airwave with the surface density of charge over the sea surface as the sea thins out.

**Keywords:** CSEM method, land, marine, airwave, detectability, splitting fields.

## Dedication

I dedicate my dissertation work to my beloved parents, Armando Calderón and Inés Moctezuma, whose inherited me their legacy of struggling and striving. And for their uncountable words of encouragement and support.

I also dedicate this work to my sister Aurea for her love and advices, her husband Adán and that little person named Emmanuel who has filled our lives with love and joy.

I dedicate this work my brother Ángel, the next master of health sciences (I'm proud of you).

I want to dedicate this thesis to my beloved girlfriend Marianggy, for staying with love and support in the most difficult part of the thesis process. I also dedicate this thesis to her brother Fernando and her parents, Mr. Alfredo and Mrs. Cecilia.

## Acknowledgments

I would like to express my acknowledgments to CONACYT for support this work with the scholarship number 225060. I also thank CICESE that provided the support to present my Ph.D research.

Thanks to CeMIE-Geo for the three months of terminal scholarship (CONACYT project number 207032). And my acknowledgments to the super computer Lamb from the Laboratory of numerical simulation, modeling and visualization of CEMIEGeo.

To the first persons that, I would like to express my sincere gratitude is to my advisors, Dr. Enrique Gómez Treviño and Dr. Luis Alonso Gallardo Delgado for the continuous support of my Ph.D study and research, for his patience, motivation, and immense knowledge. His guidance helped me in all the time of research and writing of this thesis.

Besides my advisors, I would like to thank the rest of my thesis committee: Dr. Peter Wolfgram for his insightful comments and encouragement; Dr. Antonio Fernández for the comments and disposition; and Dr. Jonás de Basabe because without him, I would never have learned about seismic modeling, he always incited me to widen my research.

My sincere thanks also goes to Dr. Mrinal Sen, who provided me an opportunity to joining to his teamwork at the UTIG in Texas and share a little of his immense knowledge and expertise.

I should like to express my thanks to Nelly Ramirez because in the beginning she inspired me and pushed me to go on this way.

I thank, the continuous words of “encouragement” of my friends Ismael Velazquez and Román Manjarrez.

I would like to thanks to Dr. Valentina Castellanos and Dr. Efraín Gómez for their support and friendship, as well as, to the next doctors of sciences: Yunuhen Muñiz, Olaf Cortés and Mario A. Fuentes. We are so close to our goal.

Thanks to all the person that I meet in this part of my live and I consider as friends: Ana Cupul, Javier Avendaño, Enrique Pérez and Olivia, Diana Trujillo, to the master Javier Alonso, Cynthia Echaui, Jackeline, Gloria E. Sánchez, Estrella Aguilar, Rocío Arellano, Abel Gutiérrez, Radha Flores, Brenda Anda, Beatriz Valdes, Daniela Tazzo, Claudia Quinteros, Salvador García, Jonathan Carrillo, Omar Hernández, Francisco del Toro, Florian Newman, Adrian Misael, Paul Calderón, José Serrano, Lenin Ávila and many others that now I don't remember.

To the staff of the posgrate of Earth Science: Dr. Juan García and LD. Ana Rosa Soto.

Last but not the least, I would like to thank to my family: uncles, aunts and cousins.

Thanks for all your encouragement!

## Contents

	Page
Abstract in spanish.....	ii
Abstract in english.....	iii
Dedication.....	iv
Acknowledgements.....	v
Figure list.....	ix
<b>Chapter 1. Introduction</b>	
1.1 Background.....	1
1.2 Hypothesis.....	3
1.3 Objetives.....	3
1.3.1 General objective .....	3
1.3.2 Specific objetives.....	3
<b>Chapter 2. The splitting concept using Fréchet derivative</b>	
2.1 Introduction.....	4
2.2 The integral representation.....	4
2.3 Significance of the integral representation.....	6
2.4 Computation of the integral representation.....	7
2.5 Accuracy of the integral representation.....	8
2.6 The role of the derivative with respect to frequency.....	11
2.7 Conclusion.....	11
<b>Chapter 3. Improving and assessing detectability definitions</b>	
3.1 Introduction.....	13
3.2 Using splitting for new definitions.....	13
3.3 Performance of new definitions for different water depths.....	14
3.4 Performance of new definitions for shallow waters.....	17
3.5 The shallow sea as a secondary source.....	19
3.6 A contradiction: Shallow waters are best for <i>detectability</i> .....	22
3.7 Conclusion.....	23

**Chapter 4. Understanding the effects of the sea**

4.1 Introduction.....	24
4.2 The sea.....	25
4.3 The sub-seafloor.....	28
4.4 The sea and the resistive layer.....	29
4.5 The transition sea to land.....	35
4.6 Conclusion.....	37

**Chapter 5. Controversy and the physical nature of the airwave**

5.1 Introduction.....	39
5.2 Deep waters as the reference.....	39
5.3 Shallow waters as the reference .....	41
5.4 Deep versus shallow waters.....	42
5.5 Electric charges on the Surface of the sea: the actual airwave.....	43
5.6 Conclusion.....	46

**Chapter 6. Conclusions**

6.1 Conclusions.....	47
6.2 Future work.....	48

<b>References.....</b>	<b>49</b>
------------------------	-----------

**Appendix A**

<b>Appendix A1</b> Justification of Appendix A.....	<b>53</b>
<b>Appendix A2</b> 3D CSEM forward modeling.....	<b>54</b>
A2.1 Approach to the problem.....	54
A2.2 Primary electric field calculation.....	54
A2.3 Averaging formula.....	55
A2.4 Catmull-Rom spline interpolation.....	56
A2.5 The finite difference approximation.....	57
A2.6 Results of 3D forward modeling.....	58
<b>Appendix A3</b> Sensitivity in the CSEM data.....	<b>60</b>
<b>Appendix A4</b> 3D Seismic forward modeling.....	<b>62</b>

A4.1 Approach to the problem.....	62
A4.2 The finite difference approximation.....	63
A4.3 Stability parameter.....	63
A4.4 Averaging formula.....	64
A4.5 Boundary condtions.....	64
A4.6 Catmull-Rom spline interpolation.....	66
A4.7 Results of seismic forward modeling.....	67
<b>Appendix A5</b> Seismic sensitivity kernels.....	69
<b>Appendix A6</b> Inverse problem statement.....	74
A6.1 Objective function.....	74
A6.2 Seafloor topography.....	75
A6.3 Objective function solver.....	76
A6.4 Test of CG algorithm.....	78
A6.5 Smoothness term test.....	78
A6.6 Conjunction term test.....	79
<b>Appendix B</b> Boundary Conditions on the interface.....	87

## List of figures

Figure	Page
1 <b>Resistivity models.</b> The model represented in a) is a background model whose response is contrasted with that shown in b) which includes a resistive layer at depth. The depth to the top of the layer is 1000 m and its thickness is 50 m. The source is an electric dipole placed on the sea floor (left) and the electric dipole that acts as the receiver also rests on the seafloor (right). The frequency of the source is 0.25 Hz. The depth to the seafloor is referred to as $z_s$ .....	9
2 <b>Electric field for deep water models.</b> The continuous lines are the analytic responses for the two models shown in Figure 1, and the dots are the corresponding responses recovered using expression 13. The water depth is 2,000 m.....	10
3 <b>Electric field for shallow water models.</b> The continuous lines are the analytic responses for the two models shown in Figure 1, and the dots are the corresponding responses recovered using equation 13. The water depth is 20 m.....	10
4 <b>Electric field plus derivative for deep water models.</b> Graphical comparison of the background and heterogeneous model (Figure 1) responses vs offset. The proposed derivative measurement $ E  + T \partial E /\partial T$ using expression 10. The water depth is 2,000 m.....	12
5 <b>Electric field plus derivative for shallow water models.</b> Graphical comparison of the background and heterogeneous model (Figure 1) responses vs offset. The proposed derivative measurement $ E  + T \partial E /\partial T$ using expression 10. The water depth is 20 m.....	12
6 <b>Detectability D1.</b> <i>Detectability</i> of the resistive layer at depth using definition D1 for different water depths.....	15
7 <b>Detectability D2.</b> <i>Detectability</i> of the resistive layer at depth using definition D2 for different water depths.....	15
8 <b>Detectability D3.</b> <i>Detectability</i> of the resistive layer at depth using definition D3 for different water depths.....	16
9 <b>Detectability D4.</b> <i>Detectability</i> of the resistive layer at depth using definition D4 for different water depths.....	16
10 <b>Different detectabilities for 100m of water depth.</b> Profiles of <i>detectability</i> of the thin resistive layer for a water depth of 100 m.....	17

11	<b>Different detectabilities for 50m of water depth.</b> Profiles of <i>detectability</i> of the thin resistive layer for a water depth of 50 m.....	18
12	<b>Different detectabilities for 20m of water depth.</b> Profiles of <i>detectability</i> of the thin resistive layer for a water depth of 20 m.....	18
13	<b>Detectability of Mittet and Morten (2013).</b> Performance of definition $D_5$ for different water depths and varying noise floors according to water depth. This is Figure 10 in Mittet and Morten (2013).....	20
14	<b>Amplitude of Mittet and Morten (2013).</b> The continuous curves represent the background response corresponding to the model without the resistive layer, and the dotted curves are the scattered field by the resistive layer.....	21
15	<b>Description of the growth of the scattered fields by Mittet and Morten (2013).</b> The growth of the scattered fields by the resistive layer is interpreted by Mittet and Morten (2013) as an interaction between the air-water interface and the resistive layer. This is Figure 5 in their paper.....	21
16	<b>Detectability <math>D_5</math>.</b> Performance of definition $D_5$ for different water depths and fixed noise floor for all water depths.....	22
17	<b>Model of Figure 1b assuming a water depth of 2000m.</b> Upper figure density of contributions from the sea. Middle figure relative contributions from the sea and sub-seafloor. Lower figure density of contributions from the sub-seafloor.....	25
18	<b>Density of contributions from the sea for different water depths.</b> The density of contributions from the sea defines four zones. Zone I: direct current; Zone II: induction; Zone III: airwave; and Zone IV: plane wave. The arrows indicate how the airwave stops moving towards shorter offsets as the water depth decreases. The vertical scale represents distance upwards from the sea floor.....	26
19	<b>Maxima contributions from the sea surface and seafloor.</b> This curve summarizes the sections shown in Figure 18 for the sea surface and seafloor.....	27
20	<b>Maxima contributions from sea (integral of density).</b> This curve summarizes the sections shown in Figure 18. It shows the maximum of the total contribution from the sea as a function of the water depth.....	27

21	<b>Density of contributions from the sub-seafloor for different water depths.</b> The density of contributions from the sub-seafloor defines the same four zones as the contributions from the sea. Zone I associated with galvanic currents intensifies as the water depth decreases since the effect of the sea decreases. The induction zone II decreases in intensity and also loses offset span as the water depth decreases. Comparing with Figure 18 the airwave migrates from the sea to the formation as the water depth decreases, but now it possesses an intense negative component. The vertical scale represents depth from the sea floor.....	28
22	<b>Density of contributions from the sub-seafloor for the background model.</b> The density of contributions from the sub-seafloor for the background model defines the same four zones shown in Figures 18 and 21. One difference is that they occur over a shorter span of offsets and that there are no discontinuities at depth associated with the thin resistive layer. The frequency is $f=0.25$ Hz, the same as for Figures 18 and 21. The seafloor is the reference depth and increase when the sub-seafloor depth increase.....	29
23	<b>Maxima contributions from the resistive layer (integral of density).</b> The positive and negative contributions from the resistive layer respond in opposite ways to the decrease of the water depth. The curves cross at the water depth where the contribution from the sea is a maximum.....	30
24	<b>Maxima of contributions from the sea and from the resistive layer.</b> Comparison of maxima contributions from the sea and from the resistive layer reveals that the response of the latter can be larger than that of the former below a critical depth.....	31
25	<b>Electric field at offset of maximum contribution as a function of water depth.</b> Amplitude of the electric field corresponding to the maxima of contributions from the sea and from the resistive layer.....	32
26	<b>Maxima of contributions to the magnitude of the electric field.</b> Maxima contributions from the sea and from the resistive layer as functions of water depth.....	32
27	<b>Maxima of normalized sea contributions for different frequencies and different depths to resistive layer.</b> a) The curves of maximum contribution from the sea for different frequencies are approximately scaled versions of each other. After a local maximum all tend to vanish as the water depth decreases. b) The depth to the resistive layer has little effect on the location of the maximum contribution. The frequency used is 0.25 Hz.....	34

28	<b>Thin conductive layer.</b> Curves of electric field magnitude for the background model 1a, the three curves has the same conductance but with different thickness and resistivity in the water layer. The curves shows how in the limit, the sea becomes a thin conductive layer. This only happens in large offsets.....	35
29	<b>Density of contributions from the sub-seafloor for different water depths.</b> The density of contributions from the sub-seafloor is practically identical for a water depth of 30 m (top) and no sea (bottom).....	36
30	<b>Moving from marine CSEM to land CSEM.</b> Density of contributions from the sub-seafloor for three seemingly different models. Models A simulate sea CSEM for a very shallow sea 10 cm deep. Neither the source nor the receiver dipoles are grounded to the sea floor. Galvanic contact is provided by the sea water. Model B is the same as model A, but both dipoles are buried 10 cm below the sea floor. Model C is the same as model B but with the sea water removed. This model simulates land CSEM. It can be observed that the density of contributions for the three seemingly different settings is essentially identical. This illustrates that the transition from sea to land CSEM is smooth. Notice that the figures on the left hand side are not to scale.....	37
31	<b>Normalization of the electric field amplitude to deep water.</b> The electric field on the sea floor for different water depths is normalized using the values for the deepest water of the model without the resistive layer. a) Electric field corresponding to the model with the resistive layer. b) Electric field corresponding to the model without the resistive layer.....	40
32	<b>Ratio of image of Figure 30b to that of Figure 30a.</b> This figure is the typical <i>detectability</i> formula for different offsets and water depths.....	40
33	<b>Normalization of the electric field amplitude to shallow water.</b> The electric field on the sea floor for different water depths is normalized using the values for the shallowest water of the model without the resistive layer. a) Electric field corresponding to the model with the resistive layer. b) Electric field corresponding to the model without the resistive layer.....	41
34	<b>Difference of response normalized by electric field with and without resistive layer.</b> a) Difference of responses normalized by the electric field amplitude with the resistive layer. b) Difference of responses normalized by the electric field amplitude without the resistive layer. The images correspond to the magnitude of the differences.....	42
35	<b>Difference of response normalized by the difference in deep and shallow water.</b> a) Difference of responses normalized by that of the deepest water. B) Difference of responses normalized by that of the shallowest water.....	43

36	<b>Superficial density of charge on the sea surface.</b> The images represent charges on the surface of the sea for different water depths. a) For a model with the resistive layer. b) For a model without the resistive layer.....	44
37	<b>Superficial density of charge on the sea surface normalized by deep and shallow water.</b> The images represent charges on the surface of the sea for different water depths. a) Normalized with respect to shallow waters. B) Normalized with respect to deep waters.....	45
38	<b>Superficial density of charge on the sea surface normalized by deep and shallow water for a model with a resistive layer.</b> The images represent charges on the surface of the sea for different water depths. a) Normalized with respect to shallow waters. B) Normalized with respect to deep waters.....	46
39	<b>Staggered grid scheme for the finite volume of scattered electric field formulation.</b> a) It is a section of the mesh model; the nodes are defined as $i, j, k$ and the Cartesian position as $x_i, y_j$ and $z_k$ , the electric fields are in the midpoints of the edges $E_x(x_{i+1/2}, y_j, z_k), E_y(x_i, y_{j+1/2}, z_k), E_z(x_i, y_j, z_{k+1/2})$ and the conductivity model in the center of the mesh volume $\sigma(x_{i+1/2}, y_{j+1/2}, z_{k+1/2})$ . The finite volume stencil for the $E_x$ field calculation is marked in light navy line. b) Finite volume discretization for the $E_x$ field, the control volume $\Omega$ in color gray surround the field with bounding surface $\Gamma$ . Similar figures are create for the $y$ -component and $z$ -component.....	55
40	<b>Centripetal Catmull-Rom.</b> a) Comparative of the different kind of parameterization for Catmull-Rom Spline. b) Pyramid of Barry and Goldman (1998) for cubic Catmull-Rom Spline.....	57
41	<b>3D CSEM forward modeling.</b> Comparative of the electric fields calculated with the three dimensional forward model (cross) and the semi-analytical code DIPOLE1D developed by Key in 2009 (lines). a) $E_x$ . b) $E_y$ . c) $E_z$ . The worst similarity is in $E_y$ field because in inline direction this field is too small and the differences between the cross and the lines is due to the computational errors.....	59
42	<b>Sensitivity 3D CSEM.</b> Graphical comparison of the $E_x$ electric field sensitivity. The blue line is the sensitivity calculated by the DIPOLE1D code developed by Key in 2009. The red cross is the sensitivity calculated using the adjoint formulation for the tridimensional model.....	61
43	<b>Staggered-grid scheme for displacement-stress formulation.</b> Spatial grid cell for the staggered-grid finite difference scheme; the nodes are defined as $i, j, k$ and the cartesian position as $x_i, y_j$ and $z_k$ , the displacement are in the midpoints of the edges $u_x(x_i, y_{j+1/2}, z_{k+1/2}), u_y(x_{i+1/2}, y_j, z_{k+1/2}), u_z(x_{i+1/2}, y_{j+1/2}, z_k)$ and the model properties in the nodes $\rho(i, j, k), \mu(i, j, k)$ and $\lambda(i, j, k)$ .....	62

44	<b>Hybrid boundary condition scheme.</b> The gray color represents the hybrid boundary zone and the white color is the region where the original computational domain is calculated. The figure is not to scale, the computational domain is larger than hybrid boundary area. The subscript $l$ in vector position means the node in the absorbing direction, e.g. for the left border $u_x(x_l, y_{j+1/2}, z_{k+1/2})$ , $u_y(x_{l+1/2}, y_j, z_{k+1/2})$ and $u_z(x_{l+1/2}, y_{j+1/2}, z_k)$ .....	65
45	<b><math>u_x</math> seismograms.</b> Seismogram of the $u_x$ displacement. a) Model without hybrid boundary conditions. b) Model with hybrid boundary conditions. Is notorious the effect of the spurious reflections and the need of use non-reflecting boundaries.....	67
46	<b>Forward modeling with boundary conditions.</b> Different step times for the $u_x$ displacement. The source is a wavelet function in the x-direction. The model is a homogenous half space with $v_p=1,700$ m/s, $v_s=1,400$ m/s and $\rho=1,200$ g/cm <sup>3</sup> , in the top has a free surface and hybrid boundary conditions in the remaining borders. The wave propagation shows reflections only in the top of the model.....	68
47	<b>Backward modeling.</b> Comparison of the $u_x$ for the forward modeling (a,b,c,d,e) and the backward modeling (f,g,h,i,j) in the most representative step times. It is clear, how the wave field and its reflections are recovered.....	72
48	<b>P-sensitivity kernels.</b> a) P-sensitivity kernel $K_p$ to the x-z plane. b) P-sensitivity kernel $K_p$ to the y-z plane. c) P-sensitivity kernel $K_{vp}$ to the x-z plane. d) P-sensitivity kernel $K_{vp}$ to the y-z plane. e) P-sensitivity kernel $K_{vs}$ to the x-z plane. f) P-sensitivity kernel $K_{vs}$ to the y-z plane.....	73
49	<b>Topography model.</b> This is the topography included in the next examples, the values of the models over this topography have been chosen to simulate the sea. The objective function only takes the values below the seafloor because the sea is always constant.....	75
50	<b>CG Algorithm.</b> Preconditioned conjugate gradient method algorithm used to optimize the objective function. ....	77
51	<b>Regularization test.</b> The first column are the objective models to be reached, the second column are the initial models and the last column are the solutions after one iteration in the conjugate gradient algorithm. Notice that, the first column and the third columns have the same models. The values given in the models has no a physical meaning.....	81

- 52 **Smoothness test.** The first column are the objective models to be reached, the second column are the initial models and the last column are the models solutions obtained from the conjugate gradient algorithm using the Equation 53. The operator used in this example was a second derivative operator with  $\beta = 1.0E5$ . Comparing the first and the last column, the objective models are reached but with a smooth transition in the middle of the models, where the values change. The values given in the models has no a physical meaning..... 82
- 53 **Smoothness test 1.** Each line is the final model obtained from the conjugate gradient algorithm optimizing the Equation 53 with a first derivative operator and different parameters  $\beta$ 's. When the smooth term of equation 53 increase the final model become smoother, so much that the final model obtained with the largest  $\beta$  is a homogenous model (orange line)..... 83
- 54 **Smoothness test 2.** Each line is the final model obtained from the conjugate gradient algorithm optimizing the Equation 53 with a second derivative operator and different parameters  $\beta$ 's. The second derivative operator is more robust than the first derivative operator..... 84
- 55 **Initial models of Conjunction test.** a) Model 1, the model proposed is similar to the previous models the only difference is the smooth transition in the middle of the model. b) Model 2, the model was built with an arctangent function in the x- and z-direction but constant in y-direction. c) The value of the curves were extracted from the lines of Model 1 and Model 2 in the z-direction..... 85
- 56 **Conjunction test.** Different iteration to optimize the Equation 54. The parameter used are  $\alpha_1 = 0.01$  for Model 1,  $\alpha_2 = 1,000$  in Model 2,  $\beta = 1$  for both models and  $\gamma_{12} = 100$ . The initial are in Figure 57. The objective models are the same that the initial models. The first column is the evolution of Model 1 in each iteration until the reach the solution in 450 iterations..... 86
- 57 **Boundary condition.** Pillbox used for establishing the boundary condition and its physical nature at the air-sea interface. The plus signs represent electric charges deposited on top of the sea. The symbol  $\lambda$  stands for the surface density of charge and has the units of Coulombs/square meter..... 88

## Chapter 1. Introduction

---

### 1.1. Background

Frequency-domain, marine controlled-source electromagnetic (CSEM) methods were originally developed to determine the high resistivity of the lithosphere in the deep oceans (Cox, 1981; Young and Cox, 1981). Nowadays, they are routinely used to map resistive hydrocarbons in the sub-seafloor (e.g., Eidesmo et al., 2002; Constable, 2006; Key, 2009). This transfer of technology from the deep oceans to shallower seas introduced new challenges that are the object of research in recent literature. One of them has been associated with the electromagnetic interactions on the air-water interface which has been called the airwave effect. When the depth of the sea is less than the target's depth difficulties were anticipated about detecting the target (e.g., Eidesmo et al., 2002). The atmosphere, being highly resistive, competes and may overcome the effect of a resistive geological layer at depth. Insights into the interactions of the different agents have been widely explored (e.g., Løseth, 2011). One of the measures to quantify the effect is called *detectability* and is defined as the ratio of the magnitude of the responses of two models. One model includes the target, the resistive layer at depth, and the other is the reference model with homogeneous sub-seafloor resistivity. The response of the former divided by that of the latter defines *detectability* (e.g., Chen and Alumbaugh, 2011).

The concept of *detectability* was the first quantitative measure used to predict and show explicitly whether a resistive layer would be detectable or not. For deep waters, this ratio is larger than unity indicating an easy detection. However, for water shallower than a few hundred meters it rapidly decreases to unity, indicating the absence of the anomalous resistive layer. This motivated developments to improve the performance of marine CSEM. Mittet (2008) explores other definitions that take into account the phase of the responses and that trend better estimates for shallow waters. One recognizable tendency is to decompose the data into convenient elements for their further analysis. For instance, Amundsen et al. (2006) decompose the electromagnetic fields into up- and down-going components, and use the up-going part to improve *detectability*. This improves *detectability* because the up-going fields come directly from the geology at depth. On the other hand, Chen and Alumbaugh (2011) use an approximate decomposition that includes a lateral wave, which is identified as the airwave. From the analysis of this wave, they concluded that the frequency derivative of the data with respect to frequency is relatively immune to the water depth. The same results are reported by Maaø and Nguyen (2010) using a different approach. As a

closing remark regarding the definition of *detectability*, it can be said that although useful and motivating, the concept defined as a ratio captures only partially the contrast of the two responses, with and without objective.

The matter was settled by Mittet and Morten (2012), who used differences of responses normalized by the expected data errors: neither in theory nor in practice is the airwave an obstacle to detect resistive layers at depth in shallow waters. To explain how this is possible in spite of the airwave, Mittet and Morten (2013) show that the scattered fields from the anomalous resistive layer grow at as much as the airwave effect as the water depth decreases. The result is a fairly stable sensitivity for shallow waters. This is interpreted as a positive feedback from the airwave acting as a secondary source to excite the response of the anomalous resistive layer at depth. The interpretation of Mittet and Morten (2013) seems to lead to the conclusion that a thin sea is needed for a proper detection of a resistive layer at depth. This would imply that land CSEM are at a disadvantage with respect to its marine counterpart. Their interpretation relies on concepts that, like the airwave, were introduced recently by marine CSEM methods for hydrocarbon exploration. In a recent review Streich (2016) highlights this point, on how research on marine CSEM has grown independently from the earlier developments in land CSEM (e.g., Eadie and West, 1980; Nekut and Spies, 1989).

I consider contributions from the sea and below the seafloor using the concept of Fréchet derivatives. The approach has the potential of unveiling hidden effects like the air-wave because it summarizes and separate the physics for a particular setting. The concept has been applied to land, marine and airborne CSEM (e.g., Gómez-Treviño and Edwards, 1983; Edwards et al., 1984; Christensen, 2014). I begin by recalling an exact theory derived from the classical scattering equations by Gómez-Treviño (1987a), which states that the Fréchet derivatives also play the role of weighting functions for conductivity itself, not just for perturbations.

The thesis is organized as follows. Chapter 2 presents the integral formulation used in the analysis and how the required computations are carried out in practice. Chapter 3 explores existing definitions of *detectability* and proposes a set of three new definitions based on the splitting of responses. The extensive analysis of the effect of the sea on the detection of the resistive layer at depth is presented in Chapter 4, and the independent assessment of results is left to Chapter 5. Finally, Chapter 6 presents the conclusions.

## 1.2 Hypothesis

Presently, land and marine CSEM methods do not merge into each other because of recently introduced concepts like that of the airwave. This has created confusion regarding the role of the sea, whose effect seems to increase as the water column decreases. The hypothesis here is that both land and sea CSEM must merge into each other as the water disappears.

## 1.3 Objectives

### 1.3.1 General objective

The objective of the present work is to demonstrate that marine CSEM methods merge naturally with their land counterparts at their transition at zero water depth. Also remove or modify concepts involved in marine case that prevent a smooth transition to land.

### 1.3.2 Specific objectives

- To split the electric field measured in the seafloor into their composing contributions from the sea and from below the seafloor using the concept of Fréchet derivatives.
- To improve and assess the *detectability* definitions
- To understand the effects of the sea in the marine CSEM data.
- To provide a physical model for the airwave.

## Chapter 2. The splitting concept using Fréchet derivatives

---

### 2.1. Introduction

Splitting marine CSEM fields is a common practice to evaluate the data sensitivity to the subsurface resistivity distribution. For instance, Amundsen et al. (2006) decompose the electromagnetic fields into up- and down-going components, and use the up-going part to improve sensitivity. The improvement results from the up-going fields come directly from the geology at depth. On the other hand, Chen and Alumbaugh (2011) use an approximate decomposition to reduce the effect of the water. They conclude that the derivative of the data with respect to frequency is independent of the water depth. This result strengthens and provides an independent justification of the proposal of Maaø and Nguyen (2010) of the special properties of the derivative. In this thesis the approach developed by Gómez-Treviño in 1987a was used to split the fields, the approach states that the Fréchet derivatives or sensitivity functions also play the role of weighting functions for electrical conductivity, not just for their perturbations. This chapter gives a brief account of the theory and practical computations of weighting functions. It will also detail the role of the derivative of the data with respect to frequency enters naturally into the formulation.

### 2.2. The integral representation

I begin with Maxwell's equations in the quasi-static approximation, on the basis that in the sea and in the sub-seafloor displacements currents are several orders of magnitude smaller than conduction currents. In the air, the approximation is justified on the basis that the wavelengths are orders of magnitude larger than the distances between transmitters and receivers, so that the delays introduced by the finite velocity of EM waves is negligible (e.g., Grant and West, 1960). In this respect, marine and land CSEM are not much different from each other. The approximation will be tested below using a typical setting. For a given period  $T$ , Faraday's and Ampere's laws which govern the induction and the flow of electric current in conductive media can be written as

$$\nabla \times \mathbf{E} = -i \left( \frac{2\pi}{T} \right) \mathbf{B} \quad , \quad (1)$$

and

$$\nabla \times \mathbf{H} = \sigma \mathbf{E} + \mathbf{J}_0 \quad ; \quad (2)$$

where  $\mathbf{E}$  stands for the electric field,  $\mathbf{B}$  for the magnetic induction vector,  $\mathbf{H}$  for the magnetic field,  $i$  for the imaginary unit and  $\mathbf{J}_0$  for the current density of an external source. It is understood that the electrical conductivity  $\sigma$  varies with position. Angular frequency is written for convenience in terms of the period  $T$  in order to simplify the following scaling exercise: multiply  $T$  and  $\sigma$  by the same constant  $k$  and work out the resulting fields. The equations transform to

$$\nabla \times \mathbf{E} = -i \left( \frac{2\pi}{kT} \right) \mathbf{B}, \quad (3)$$

and

$$\nabla \times \mathbf{H} = k\sigma \mathbf{E} + \mathbf{J}_0. \quad (4)$$

By inspection, the constant  $k$  scales  $\mathbf{E}$  to  $k\mathbf{E}$ . Contrasting with the original formulas this implies that

$$k\mathbf{E}(k\sigma, kT) = \mathbf{E}(\sigma, T). \quad (5)$$

Let us now introduce another constant  $h$  as  $k = 1 + h$ . The last equation can be written as

$$\mathbf{E}(\sigma + h\sigma, T + hT) - \mathbf{E}(\sigma, T) = -h\mathbf{E}(\sigma + h\sigma, T + hT). \quad (6)$$

At this stage, assume that  $h \ll 1$ . The left hand side of this equation represents a small perturbation  $\delta\mathbf{E}(h\sigma, hT)$ . The contribution from the conductivity perturbation  $\delta\sigma = h\sigma$  can be expressed in terms of the Fréchet derivative  $\mathbf{F}_\sigma(\sigma, T, z)$  of  $\mathbf{E}$  with respect to  $\sigma$ , and that corresponding to the perturbation  $\Delta T = hT$  can be expressed in terms of the partial derivative of  $\mathbf{E}$  with respect to  $T$ . Leaving the right hand side as it is, the result can be written as

$$\int_a^b \mathbf{F}_\sigma(\sigma, T, z) h\sigma(z) dz + \frac{\partial \mathbf{E}}{\partial T} hT + \mathbf{O}(h^2) = -h\mathbf{E}(\sigma + h\sigma, T + hT). \quad (7)$$

Here I am assuming a one-dimensional (1D) conductivity distribution  $\sigma(z)$  defined over the domain  $[a, b]$ . Also, there is an implicit dependence of  $\mathbf{F}_\sigma$  and  $\mathbf{E}$  on offset in this and subsequent equations. Now divide both sides by  $h$  and take the limit as  $h$  goes to zero. The result is

$$\int_a^b \mathbf{F}_\sigma(\sigma, T, z) \sigma(z) dz + \frac{\partial \mathbf{E}}{\partial T} T = -\mathbf{E}(\sigma, T). \quad (8)$$

This equation can be interpreted in several ways. In the original derivation in Gómez-Treviño (1987a) it is considered as an exact nonlinear integral equation for EM inverse problems. The term *exact* refers to it not being a linearized equation. Considering  $\sigma(z)$  as the unknown and the electric field and its derivative as the data, expressions of the type of (8) are formal statements for 1D EM inverse problems. Early difficulties to solve them reported by Dosso and Oldenburg (1991) seemed an impasse for actual inversions. However, they can be iterated from an initial  $\sigma(z)$  and made to converge to adequate models as shown in Esparza and Gómez-Treviño (1996, 1997) for magnetotelluric (MT) and direct current (DC) resistivity soundings. The equation has been the starting point for estimating unique depth averages of  $\sigma(z)$  as an approximate, but robust solution for the 1D MT inverse problem (Gómez-Treviño, 1996; Gómez-Treviño et al., 2014), and also for imaging 2D and 3D land CSEM data (Pérez-Flores and Gómez-Treviño, 1997; Pérez-Flores et al., 2001, 2012).

### 2.3 Significance of the integral representation

Interestingly, expression 8 also provides a representation of the data in terms of their spatial sensitivity. This adds significance to the concept of sensitivity because now the data and its derivative can be viewed as contributions made up from all depths. The behavior of the integrand as a function of depth reveals the relative importance of the different regions, in the present case of the sea, the background formation and the resistive layer. At this point, it is important to recall that both  $\mathbf{E}$  and  $\mathbf{F}_\sigma(\sigma, T, z)$  are the solutions of a boundary value problem and, as such, there are not isolated contributions. No integral

expression of the fields can justify the use of its integrand for this purpose, unless the integrand is already physically meaningful. This is the case of equation 8, where the integrand is the sensitivity of the fields. Any other integrand would lead to contradictions when dealing with issues like the depth of investigation of a given datum. Thinking of either the fields as being the synthesis of elementary ground contributions, or perturbations of the fields being the synthesis of elementary ground perturbations, should lead to the same conclusions (Gómez-Treviño, 1987b; Gómez-Treviño and Esparza, 2014; Christensen, 2014; Gómez-Treviño and Flores, 2015).

## 2.4 Computation of the integral representation

With the origin placed on the seafloor,  $z$  pointing down and representing the depth of the sea as  $z_s$ , the integral is splitted into two parts:

$$\mathbf{E}(\sigma, T) + T \frac{\partial \mathbf{E}}{\partial T} = \int_{-z_s}^0 -\mathbf{F}_\sigma(\sigma, T, z) \sigma(z) dz + \int_0^\infty -\mathbf{F}_\sigma(\sigma, T, z) \sigma(z) dz. \quad (9)$$

To be specific, a single component of the electric field is considered, in this case  $E_x$  in an in-line array with the electric dipole source also aligned in the  $x$ -direction as depicted in Figure 1. With the understanding that  $E$  without a subscript represents  $E_x$ , a scalar equation for the electric field measured at the sea floor  $E(\sigma, T, z_s)$  can be written as

$$E(\sigma, T, z_s) + T \frac{\partial E(\sigma, T, z_s)}{\partial T} = \int_{-z_s}^0 -F_\sigma(\sigma, T, z) \sigma(z) dz + \int_0^\infty -F_\sigma(\sigma, T, z) \sigma(z) dz. \quad (10)$$

To compute the electric field and its Fréchet derivative, I use the algorithm and code of Key (2009). The code treats the air as another layer; which can have a non-zero conductivity and actual displacement currents are taken into account. However, as discussed earlier in relation to the quasi-static approximation, I do not consider contributions from the air. In the next section a proof of the approximation using actual calculations is present. The sea and the subsurface are divided into thin layers

of uniform conductivity  $\sigma_i$  and thickness  $\Delta z_i$ . In this case  $\sigma(z)$  is taken outside the integral, and writing the integral of the Fréchet derivative as a partial derivative we have

$$\sigma_i \int_{z_i - \Delta z_i/2}^{z_i + \Delta z_i/2} F_\sigma(\sigma, T, z) dz = \sigma_i \frac{\partial E(\sigma, T, z_s)}{\partial \sigma_i}. \quad (11)$$

Assuming now that  $\Delta z_i$  is small,  $F_\sigma$  now is approximate at the middle of the layer as

$$F_\sigma(\sigma, T, z_i + \Delta z_i/2) \cong \frac{1}{\Delta z_i} \frac{\partial E(\sigma, T, z_s)}{\partial \sigma_i}. \quad (12)$$

Since now is working with scalars, the expression 10 can be written as

$$E(\sigma, T, z_s) = \frac{1}{1+m} \int_{-z_s}^0 -F_\sigma(\sigma, T, z) \sigma(z) dz + \frac{1}{1+m} \int_0^\infty -F_\sigma(\sigma, T, z) \sigma(z) dz. \quad (13)$$

In this formula  $m = \partial \log E(\sigma, T, z_s) / \partial \log T$  is the slope of the electric field in a log-log scale. Notice that equation 5 holds for the electric field as a complex vector, so expressions 10 and 13 hold for both the real and imaginary components of the electric field. The real part on the left side of equation 13 is equal to the integral of the real part of  $[-F_\sigma(\sigma, T, z) \sigma(z)] / [1+m]$ . This ratio comes to be the density of contributions to the electric field.

## 2.5 Accuracy of the integral representation

To check on the accuracy of the density of contributions, I computed the electric field directly on one side and compared its real and imaginary parts with those obtained by integrating  $[-F_\sigma(\sigma, T, z) \sigma(z)] / [1+m]$  according to expression 13.

For both models the real and imaginary parts of the electric field are recovered through equation 13, they are achieved over ten orders of magnitude. The comparison is presented in Figure 2 for the two

models of Figure 1 with the same water depth of 2,000 m. The frequency of the source is 0.25 Hz. The sea is subdivided into 10 layers in this and all subsequent models. The underlying sediments are modeled using layers 50 m thick of equal electrical resistivity. The curves are plotted against the offset distance between transmitter and receiver.

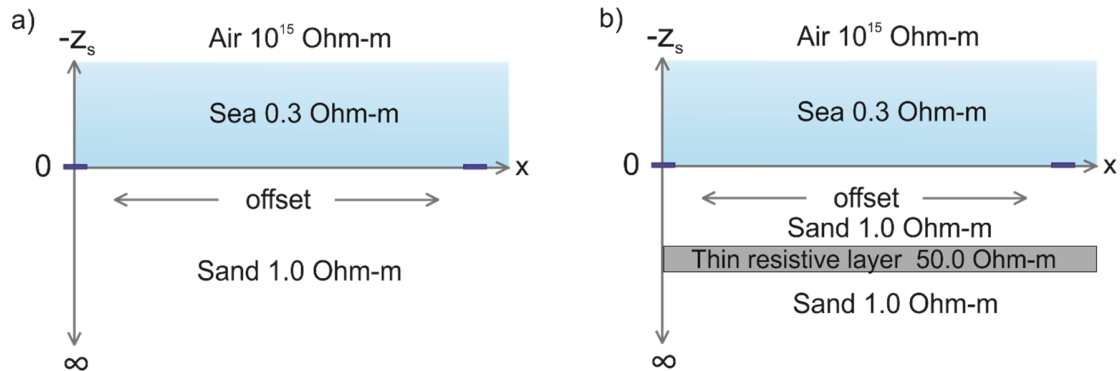


**Figure 1. Resistivity models.** The model represented in a) is a background model whose response is contrasted with that shown in b) which includes a resistive layer at depth. The depth to the top of the layer is 1000 m and its thickness is 50 m. The source is an electric dipole placed on the sea floor (left) and the electric dipole that acts as the receiver also rests on the seafloor (right). The frequency of the source is 0.25 Hz. The depth to the seafloor is referred to as  $z_s$ .

In addition to illustrate the accuracy of equation 13, the curves show that the responses of the two models are separated by more than one order of magnitude at intermediate offsets. This shows that a thin resistive layer below a 2,000 m of water is a feasible CSEM prospective target. As stated earlier, the same objective is more difficult to detect in shallow waters. Figure 3 presents the same comparison of the direct computation of the electric field with its recovery using the equality 13, but for a water depth of 20 m. The curves also show the difficulty of detecting the thin resistive layer in a shallow water scenario. The curves for the homogeneous model depart much less than an order of magnitude from those of the model that includes the resistive layer. An analyze of this issue is in the next section by means of the splitting concept explained above and then propose a strategy to improve thin layer detection.

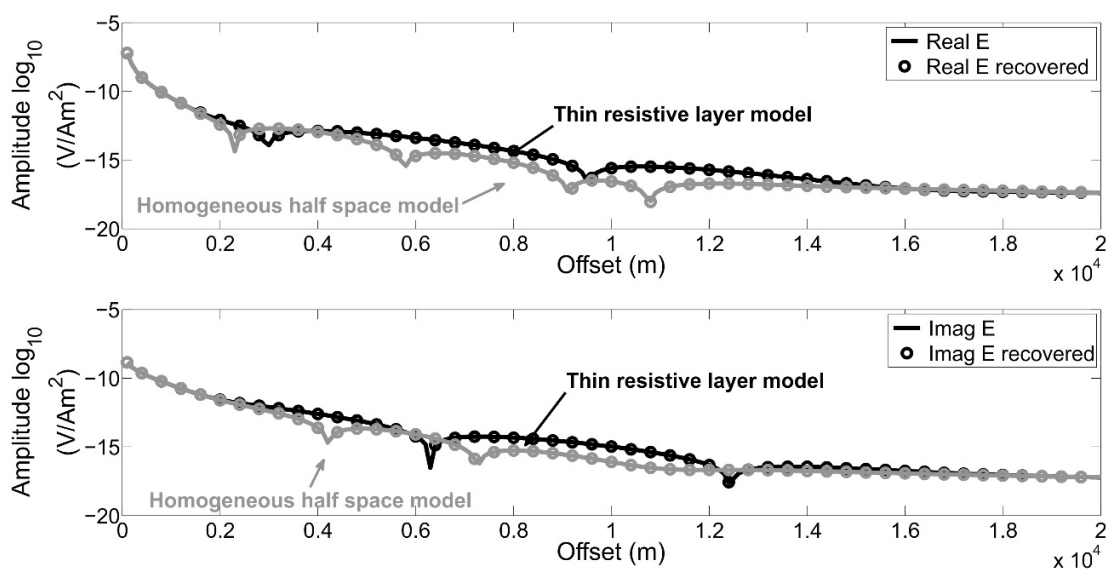


**Figure 2. Electric field for deep water models.** The continuous lines are the analytic responses for the two models shown in Figure 1, and the dots are the corresponding responses recovered using expression 13. The water depth is 2,000 m.

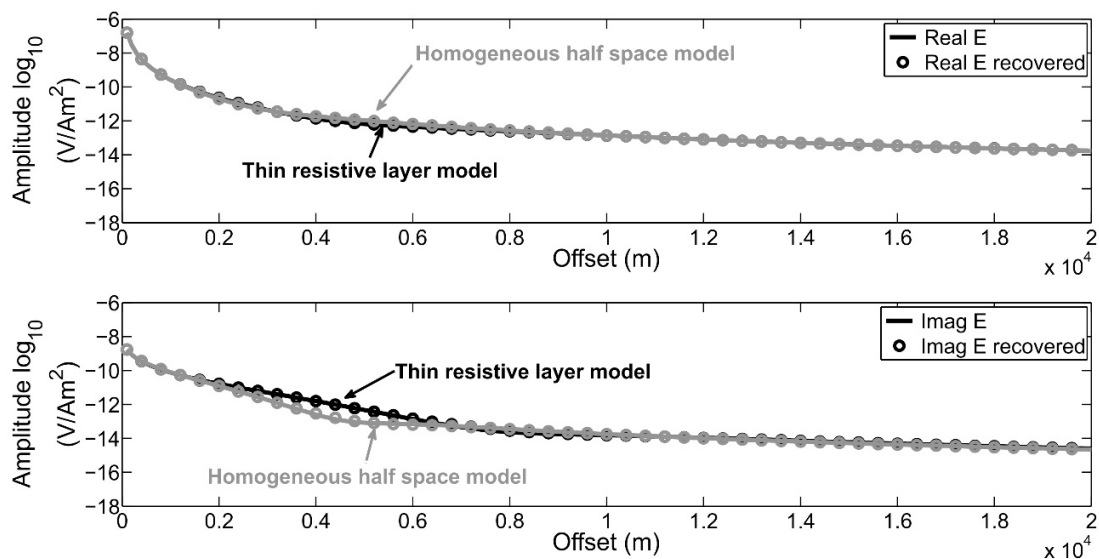


**Figure 3. Electric field for shallow water models.** The continuous lines are the analytic responses for the two models shown in Figure 1, and the dots are the corresponding responses recovered using equation 13. The water depth is 20 m.

## 2.6 The role of the derivative with respect to frequency

Equation 13 assumes that the data are measurements of the electric field. Returning to the original equation, equation 10, its left hand side can be interpreted as the data. That is, the electric field itself augmented with its derivative with respect to frequency. The comparison between the direct calculations and their synthesis through the integral of equation 10 are shown in Figures 4 and 5. The frequency of the source is again 0.25 Hz. The conductivity models are also the same represented in Figure 1, and the discretization of the model is the same as before. Figure 4 is for the deep water case of 2000 m and Figure 5 for the shallow water of 20 m. As mentioned above, some authors have suggested the use of the derivative as the data, taking measurements at two nearby frequencies, as a way to diminish the effect of the sea in shallow waters. This is confirmed by comparing Figures 3 and 5, particularly in relation to the imaginary part.

## 2.7 Conclusion

In this chapter the integral representation of the electric field has been introduced, that will be used in the following chapters. I have covered its formal derivation as well as its significance for understanding electromagnetic responses by means of splitting them as corresponding the sea and to the sub-seafloor. There was also discussion about how they are computed in practice and how accurate they are. The examples shown illustrate the problem that arises in marine CSEM when applied in shallow waters. Our approach confirms earlier claims that the derivative with respect to frequency alleviates in part the problem of shallow waters. In the next chapter, several definitions of *detectability* derived from our splitting approach are explored, in an effort to improve our understanding of how a shallow sea affects the detection of resistive layers at depth.

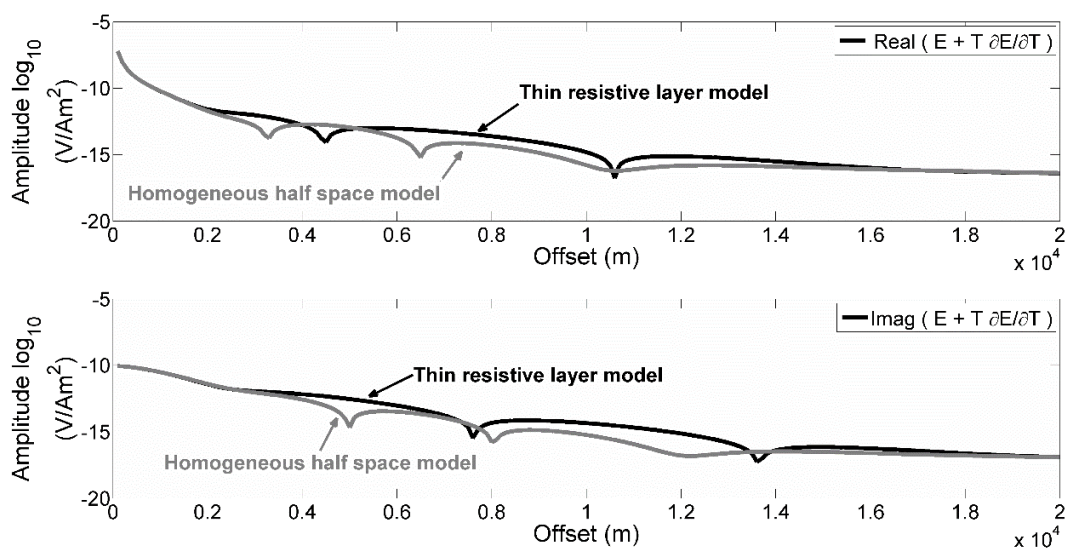


**Figure 4. Electric field plus derivative for deep water models.** Graphical comparison of the background and heterogeneous model (Figure 1) responses vs offset. The proposed derivative measurement  $|E| + T \partial|E|/\partial T$  using expression 10. The water depth is 2,000 m.

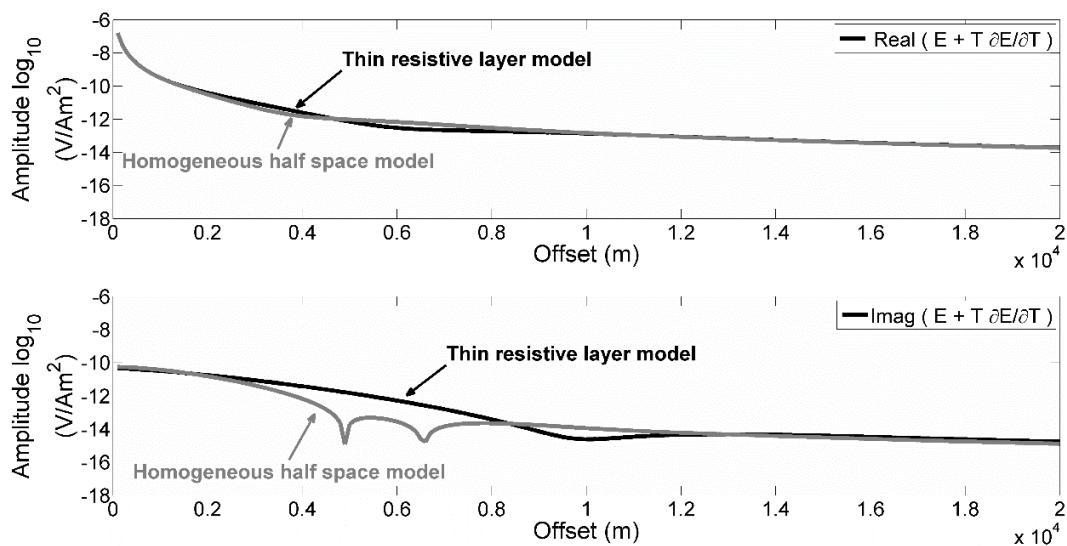


**Figure 5. Electric field plus derivative for shallow water models.** Graphical comparison of the background and heterogeneous model (Figure 1) responses vs offset. The proposed derivative measurement  $|E| + T \partial|E|/\partial T$  using expression 10. The water depth is 20 m.

## Chapter 3. Improving and assessing detectability definitions

---

### 3.1 Introduction

The concept of *detectability* has been used in marine CSEM methods to show the effectiveness of detecting a given target. Following Chen and Alumbaugh (2011) they define

$$Detectability = \frac{R_t}{R_0} , \quad (14)$$

where  $R_t$  is the response in the presence of the target and  $R_0$  the response without the target. In reference to Figure 1,  $R_t$  is the response corresponding to the model illustrated in Figure 1b) whereas  $R_0$  to that of Figure 1a). When the data is the amplitude of the electric field the standard definition is given as

$$D_1 = \frac{|E_t|}{|E_0|} . \quad (15)$$

This ratio is called  $D_1$ , for definition one. If the ratio is close to unity it has a poor *detectability* because the response that includes the resistive layer at depth is almost identical to that without the layer. The efforts mentioned in the last chapter of Amundsen et al. (2006), Chen and Alumbaugh (2011) and Maaø and Nguyen (2010) all go into improving this ratio. In this chapter a review of the work of Mittet and Morten (2012, 2013) was made and motivated to propose new definitions.

### 3.2 Using splitting for new definitions

Making use of the separation of sea and sub-seafloor contributions, a modified version of  $D_1$  can define as

$$D_2 = \frac{|E_t - [E_0]_s|}{|E_0|_{ss}} . \quad (16)$$

The subscripts  $s$  and  $ss$  stand for the sea and the sub-seafloor contributions, respectively. The idea is to isolate in the numerator the contribution from the subsurface when the target is present, but, since the model is unknown, I subtract, as an approximation, the sea contribution of the reference or base line model. This can be interpreted as eliminating all kind of source effects. The denominator is the sub-seafloor contribution of the reference model.

If now the data is considered as  $|E_t| + T \partial|E_t|/\partial T$ , it may be defined as

$$D_3 = \frac{|E_t| + T \partial|E_t|/\partial T}{|E_0| + T \partial|E_0|/\partial T} . \quad (17)$$

This definition is similar to  $D_1$  in the sense that it does not make use of the splitting of contributions. In other words, it is simply the response of the model with the thin resistive layer normalized by the response of the base line model.

The corresponding modified version of  $D_3$  when considering splitting can be written as

$$D_4 = \frac{\{|E_t| + T \partial|E_t|/\partial T\} - \{|E_0| + T \partial|E_0|/\partial T\}_s}{\{|E_0| + T \partial|E_0|/\partial T\}_{ss}} . \quad (18)$$

This definition is similar to  $D_2$  in the sense that it splits the contributions. Again, the idea is to isolate in the numerator the contribution from the subsurface when the target is present, but, since the model is unknown, I subtract as an approximation the sea contribution of the reference or base line model.

### 3.3 Performance of new definitions for different water depths

The performance of the above four definitions of *detectability* are illustrated in Figures 6 to 9. Each figure shows five water depths, ranging from 2000 to 20 m, the indicated definition. Figure 6 clearly evidence that a shallow sea is detrimental to the detection of the resistive layer at depth when using  $D_1$  definition. In contrast, a deep sea is an asset for *detectability*. The amplitude of the curves increase by

about an order of magnitude from shallow to deep waters. The overall picture for the other three definitions is very much the same.

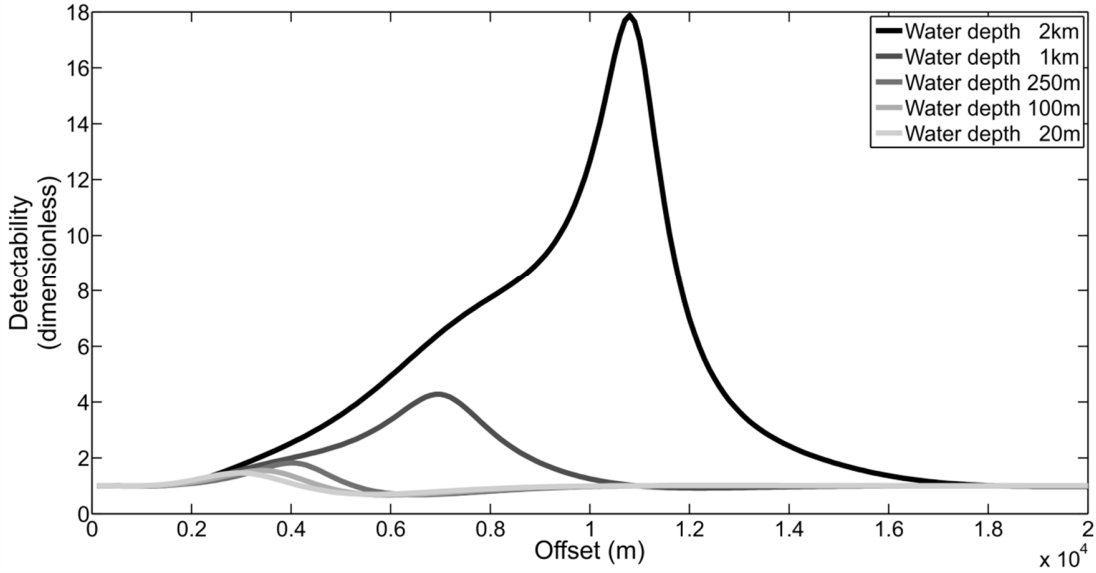


Figure 6. Detectability D1. Detectability of the resistive layer at depth using definition D1 for different water depths.

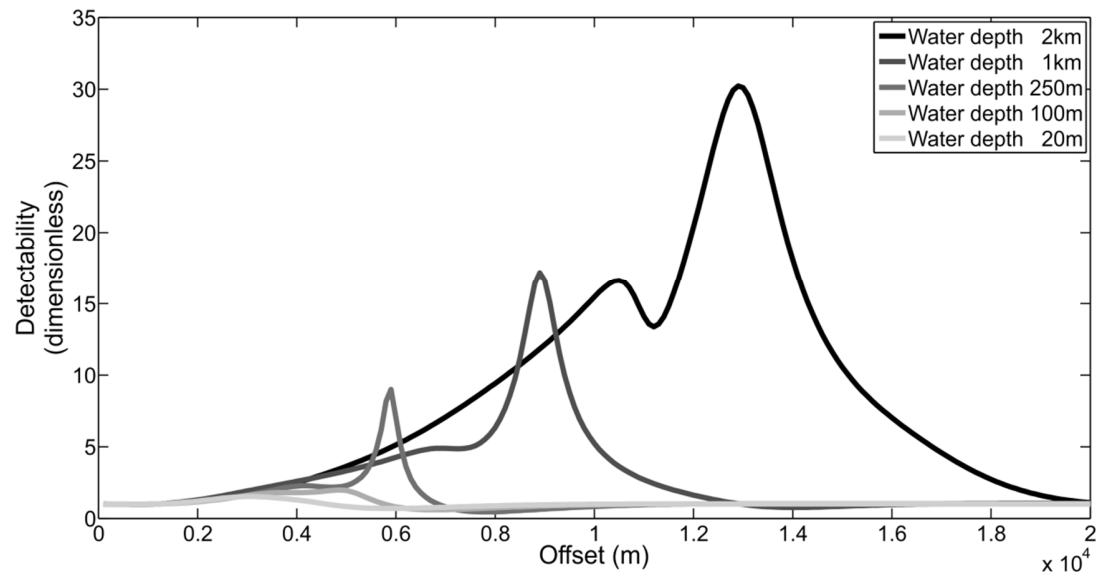
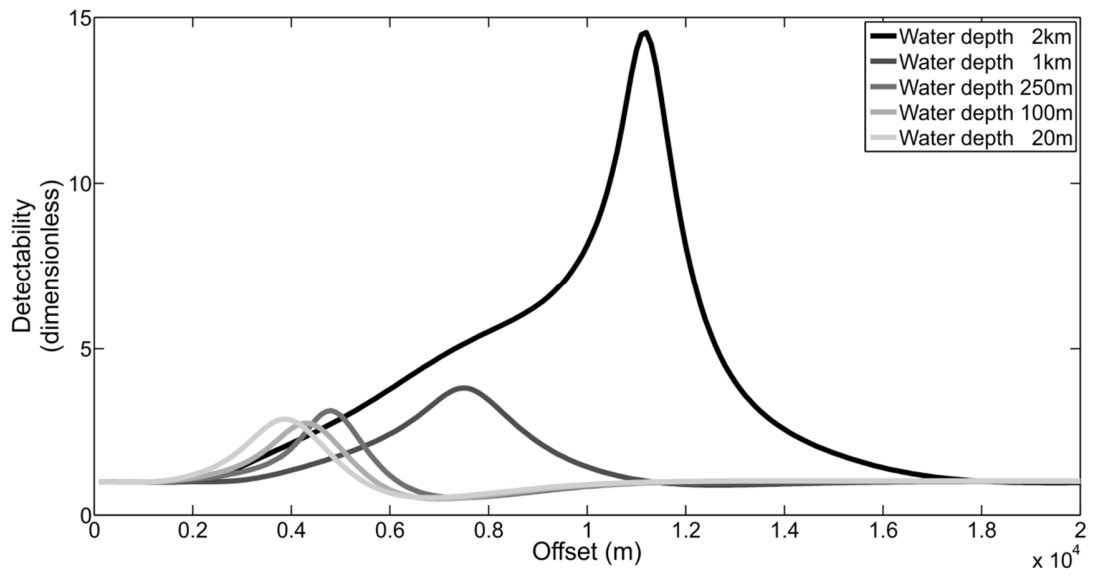
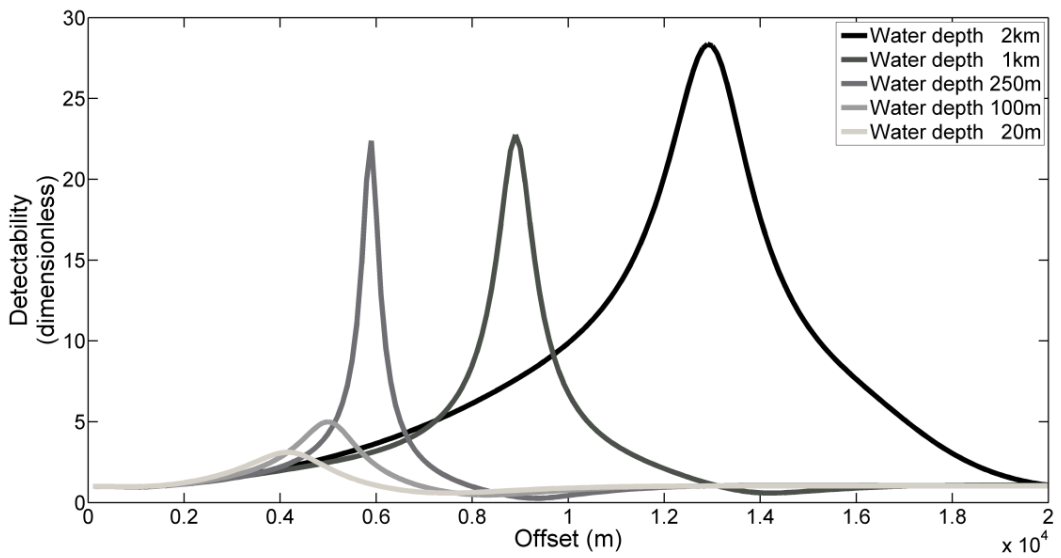


Figure 7. Detectability D2. Detectability of the resistive layer at depth using definition D2 for different water depths.



**Figure 8. Detectability D3.** Detectability of the resistive layer at depth using definition D3 for different water depths.



**Figure 9. Detectability D4.** Detectability of the resistive layer at depth using definition D4 for different water depths.

### 3.4 Performance of new definitions for shallow waters

A feature in the last four figures is the gradual increase in the depth of penetration as the water depth decreases. This shows because the maxima of the curves gradually migrate towards shorter offsets as the water depth decreases. This means that a shallow sea may also be an asset for detection but in a different way. Not so much because of the amplitude of the curves, but because the relative maxima appears at shorter offsets. This is one of the motivations for improving *detectability* for shallow waters. Figures 10 to 12 illustrate the performance of the four definitions described above for water depths of 100, 50 and 20 m. In all the cases, the proposed definitions based on splitting surpass the traditional  $D_1$ , based on the straight ratio of the response with the target to that without the target. In particular,  $D_3$  and  $D_4$ , which make use of the derivative with respect to period of the electric field. This is understandable since these responses contain more information to that of the electric field by itself. The limit case presented here corresponds to water depth of 20m (where the source is floating on the sea surface). The curves of *detectability* are shown in Figure 12. This case approaches land surveys where  $D_1 = D_2$  and  $D_3 = D_4$ . In this extreme scenario,  $D_3$  and  $D_4$  still outperform the definitions that use only the amplitude of the electric field.

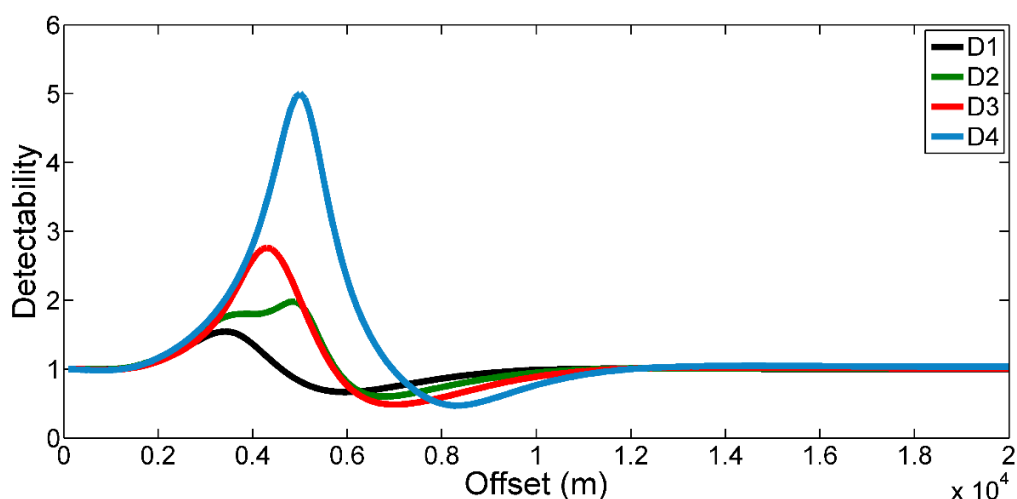


**Figure 10. Different detectabilities for 100m of water depth.** Profiles of *detectability* of the thin resistive layer for a water depth of 100 m.

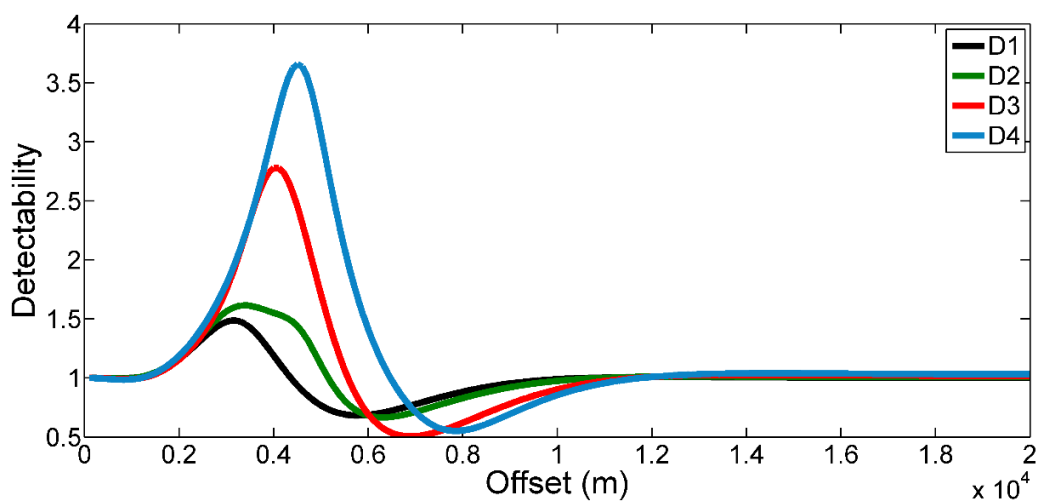


**Figure 11. Different detectabilities for 50m of water depth.** Profiles of *detectability* of the thin resistive layer for a water depth of 50 m.

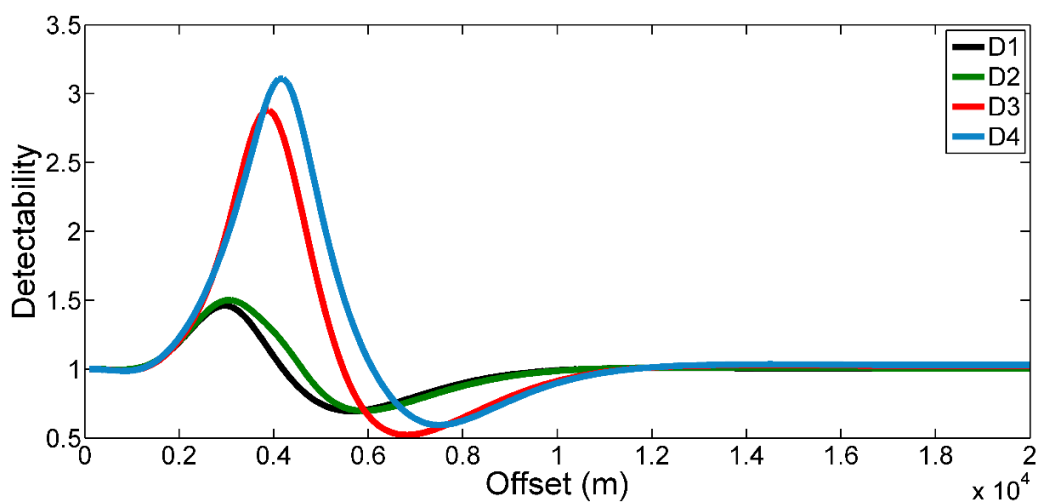


**Figure 12. Different detectabilities for 20m of water depth.** Profiles of *detectability* of the thin resistive layer for a water depth of 20 m.

### 3.5 The shallow sea as a secondary source

The performance of the above definitions is comparable or even better than others that have been proposed in the literature. However, regardless of performance, the very fact that there is margin for improvement suggests that the effect of the water column does not fully understood. After all, a ratio is only one of many possibilities to compare two responses. Mittet and Morten (2012, 2013) considered a definition based on differences of complex data and their uncertainties. I call this definition  $D_5$  and it is given by

$$D_5 = \left| \frac{\Delta E}{\delta E} \right| = \frac{|E_t - E_0|}{\sqrt{|\alpha E_t|^2 + \eta^2}} \quad , \quad (19)$$

where  $\alpha$  is the relative data uncertainty and  $\eta$  is noise floor, which in practice depends on the water depth, with shallow waters being the noisiest. Figure 13 (cf. Figure 10 in Mittet and Morten, 2015) illustrates the performance of definition  $D_5$  using  $\alpha = 3\%$  and variable noise floor according to the water depth. It can be observed that *detectability* is higher for deep waters, this does not add anything new to the previous *detectabilities*. What is new is that for shallow waters *detectability* remains relatively high and that it stops dropping as the water depth decreases. To explain this behavior Mittet and Morten (2013) compare the background field, that of the model without the resistive layer, with the field scattered by the resistive layer (reproduced here in Figure 14). Both sets of curves grow as the water depth decreases, so the detection is not hampered by the airwave. Their elaborated mathematical analysis is summarized in Figure 15 as an interaction between the air-water interface and the resistive layer. They conclude that the shallow sea acts as a secondary source that interacts with the resistive layer to enhance its influence as a scattering agent.

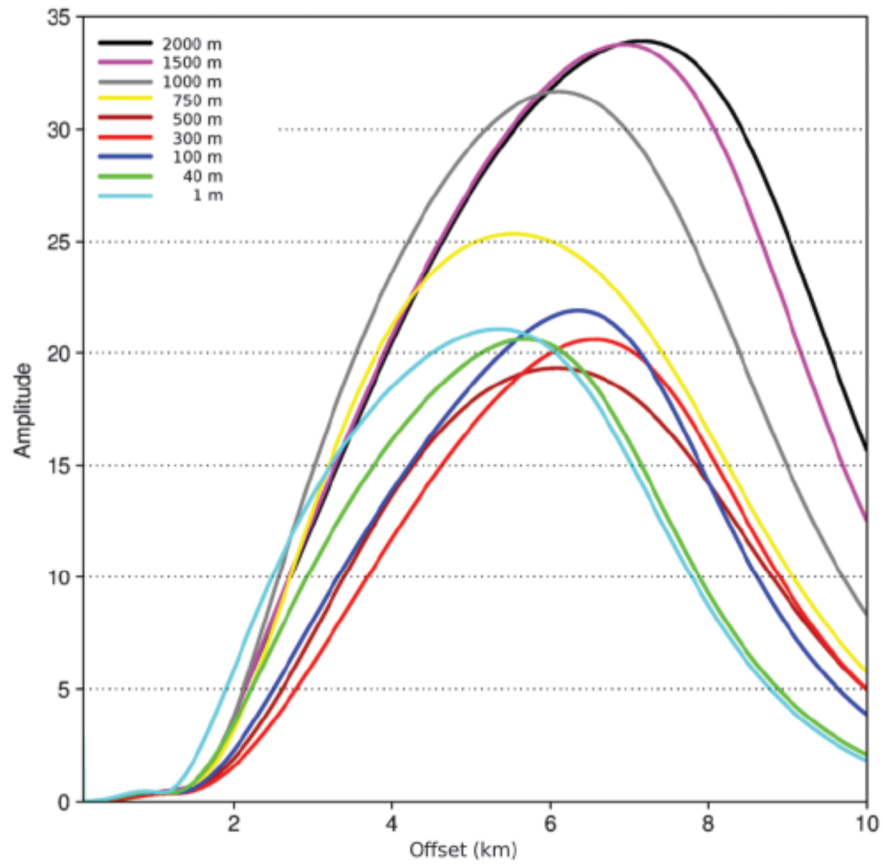


**Figure 13. Detectability of Mittet and Morten (2013).** Performance of definition  $D_5$  for different water depths and varying noise floors according to water depth. Mittet and Morten (2013).

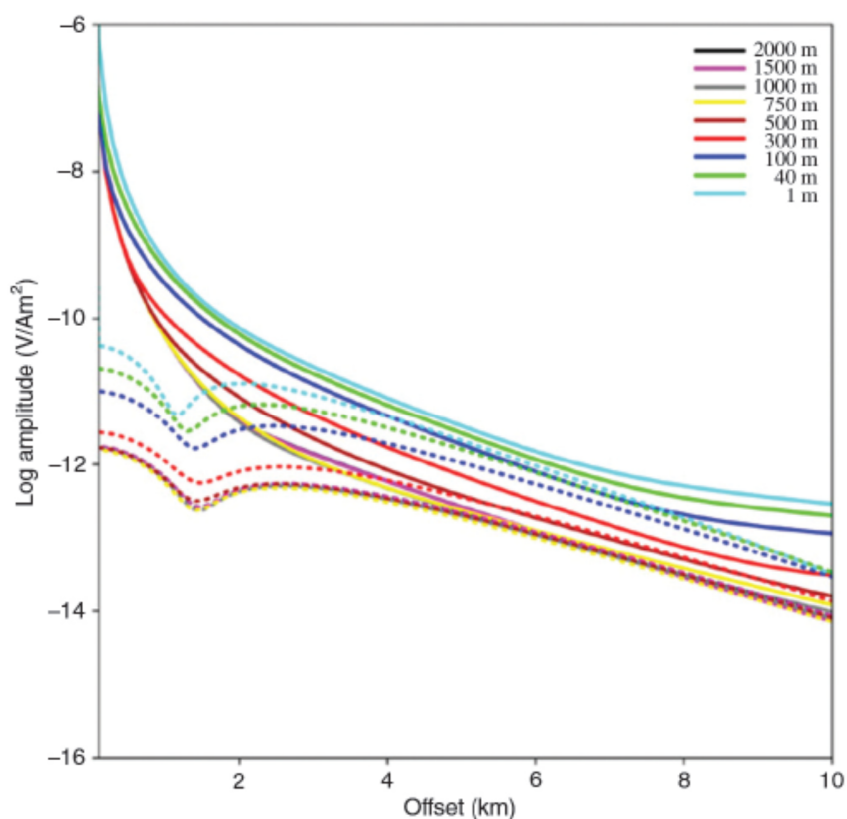


**Figure 14. Amplitude of Mittet and Morten (2013).** The continuous curves represent the background response corresponding to the model without the resistive layer, and the dotted curves are the scattered fields associated to the resistive layer.

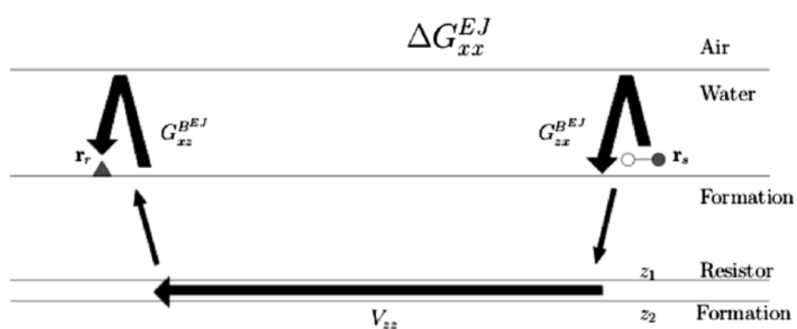


**Figure 15. Description of the growth of the scattered fields by Mittet and Morten (2013).** The growth of the scattered fields by the resistive layer is interpreted by Mittet and Morten (2013) as an interaction between the air-water interface and the resistive layer.

### 3.6 A contradiction: Shallow waters are best for detectability

Whereas Figure 13 still suggests that deep waters are better at detecting the resistive layer, it is worth considering a uniform noise floor for all water depths in equation 19. In Figure 16 the value of  $\alpha \approx 3\%$  was used as a constant with respect to offset, same as Mittet and Morten (2013), but a single value of  $1.5 \times 10^{-14} \text{ V/Am}^2$  for the noise floor, which corresponds to the noisiest case of shallow waters.

In Figure 16, it is seen that, unlike in the previous figures the highest value is for the shallowest water depth. It should also be noted that the curves are very narrow for deep waters and relatively wider, about twice judging by the half width, for shallow waters. This would predict about the same degree of *detectability* in both cases, with some loss of resolution for shallow seas. This is what actually happens as reported by Connell and Key (2013) using inverse techniques. One might be tempted to say that because of this prediction Figure 16 is a better representation of what actually happens when one goes from deep to shallow waters. However, this would be too audacious and difficult to accept on these grounds: the airwave transforming from a drawback to an asset on the basis of a few computations. To further supports this claim, the following chapter does an inspection of the contributions of all media involved.

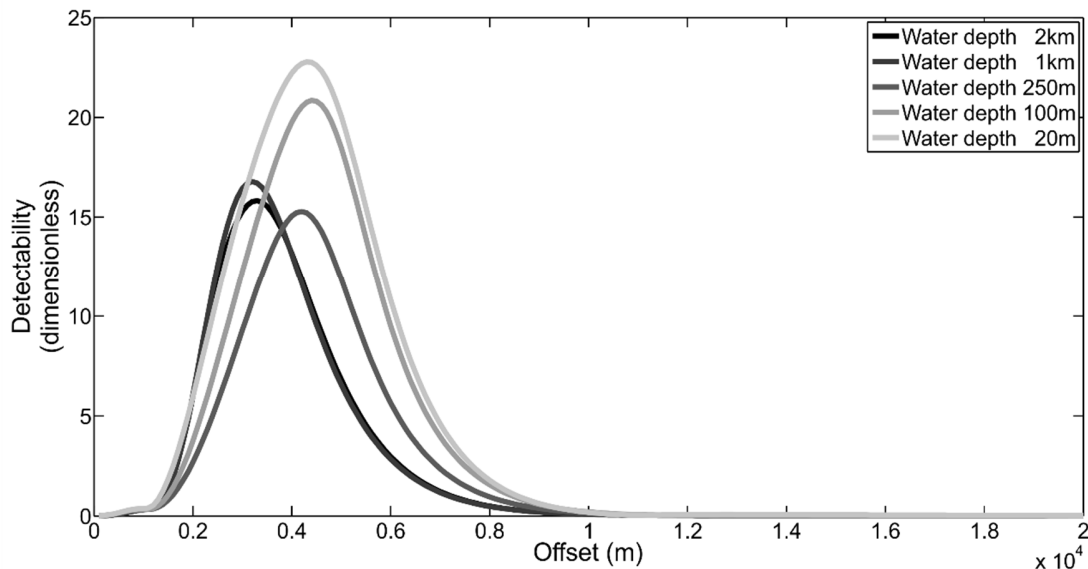


**Figure 16. Detectability D5.** Performance of definition  $D_5$  for different water depths and fixed noise floor for all water depths.

### 3.7 Conclusion

Different definitions of *detectability* seems to also enhance differently the role of the sea in marine CSEM methods. Those based on the ratio of the two responses lead to an inhibiting effect of shallow waters as clearly seen in Figure 6 for  $D_1$ . On the other hand, those based on the difference of the two responses lead to the contradicting conclusion that shallow waters are an asset for detection. This is particularly clear in Figure 16 that illustrates the performance of definition  $D_5$  in one of its varieties. It seems that it is a paradox, in the sense that the airwave seems to be at the same time a drawback and an asset to the detection of the resistive layer. How can it be both?

## Chapter 4. Understanding the effects of the sea

---

### 4.1 Introduction

In this chapter, a throughout study of the effects of the sea is presented using the splitting concept. From now on I will work with the amplitude of the electric field.. Since equation 5 also is valid for the amplitude of the electric field, expressions 10 and 13 also hold for the amplitude, provided the Fréchet and partial derivatives also correspond to the amplitude. In particular, equation 13 can be rewritten for normalized amplitude as

$$1 = \frac{|E|}{|E|} = \frac{1}{1 + m_A} \int_{-z_s}^0 - \frac{F_\sigma(\sigma, T, z)}{|E(\sigma, T, z_s)|} \sigma(z) dz + \frac{1}{1 + m_A} \int_0^\infty - \frac{F_\sigma(\sigma, T, z)}{|E(\sigma, T, z_s)|} \sigma(z) dz. \quad (20)$$

Here  $F_\sigma(\sigma, T, z) \cong \frac{1}{\Delta z_i} \frac{\partial |E(\sigma, T, z_s)|}{\partial \sigma_i}$  and  $m_A = \partial \log |E| / \partial \log T$ .

The integrands in equation 20, with the factor  $1/(1 + m_A)$  included, represent the density of contributions normalized by the amplitude of the electric field. These are relative contributions whose integrated effect is unity. Multiplying the integrands by  $|E|$ , the corresponding absolute contributions is obtained. The first integral corresponds to the sea and the second to the underlying formations. In this section, the model of Figure 1b is explored which includes the resistive layer at depth. Figure 17 is a representation of equation 20, the upper and lower figures are the density contribution from the sea and sub-seafloor, respectively. The curves in the middle summarize the total and relative contributions from the sea and sub-seafloor. The section of the density of contributions shows the sensitivity or corresponding weight for different depths for that model. In the seawater section the source highlighted is observed, meanwhile in the sub-seafloor section is the resistive layer. The curves show zones where the seawater is more important than the sub-seafloor and other zones where it is the opposite. A detailed analysis of the sea and sub-seafloor is made in the next sections changing the water depths.

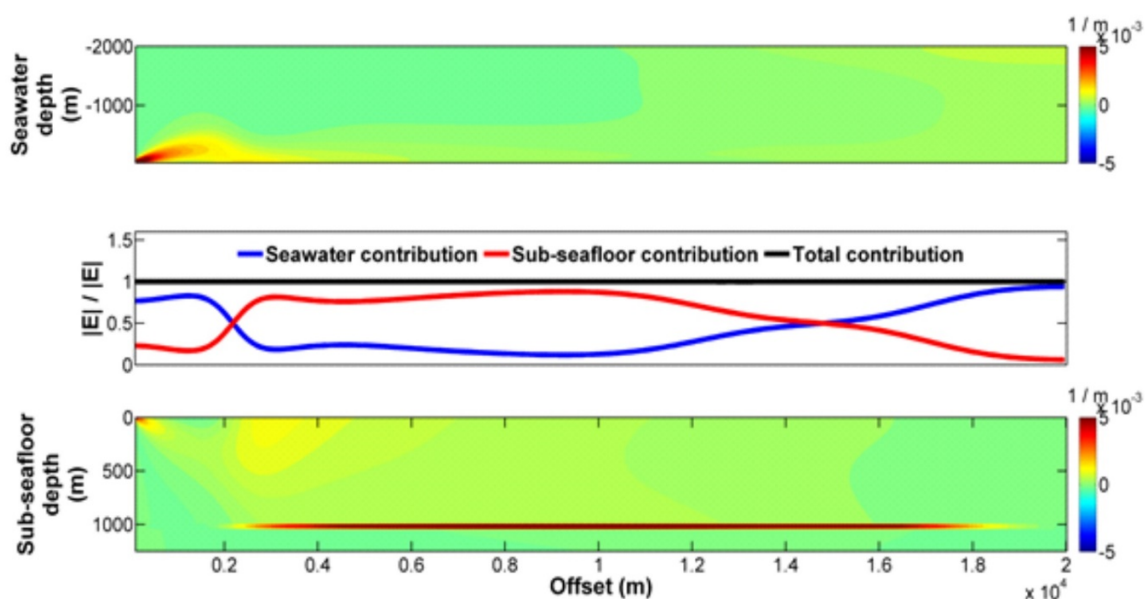
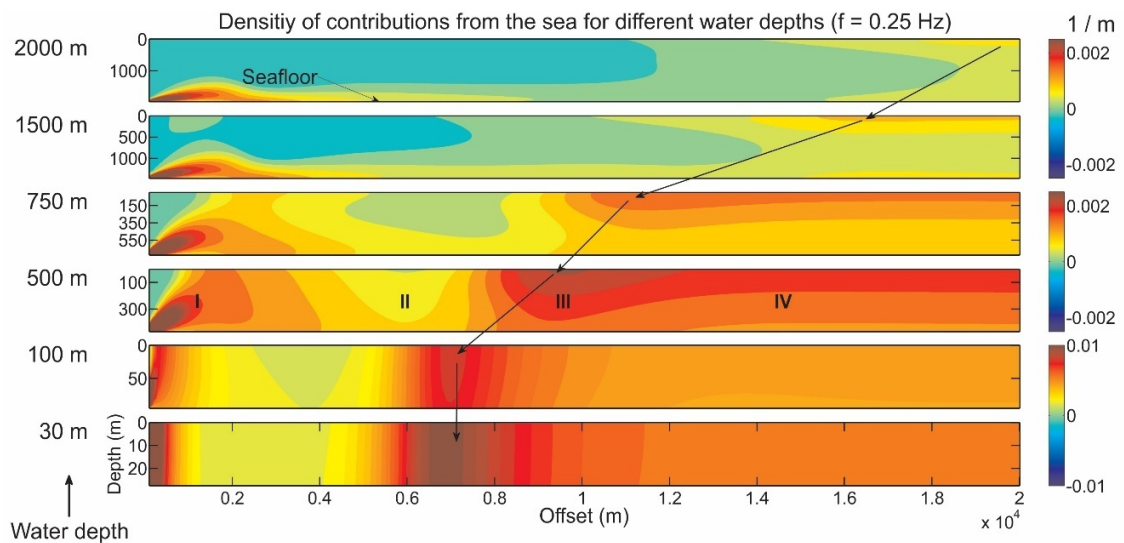


**Figure 17. Model of Figure 1b assuming a water depth of 2000m.** Upper figure: density of contributions from the sea. Middle figure: relative contributions from the sea and sub-seafloor. Lower figure: density of contributions from the sub-seafloor.

## 4.2 The sea

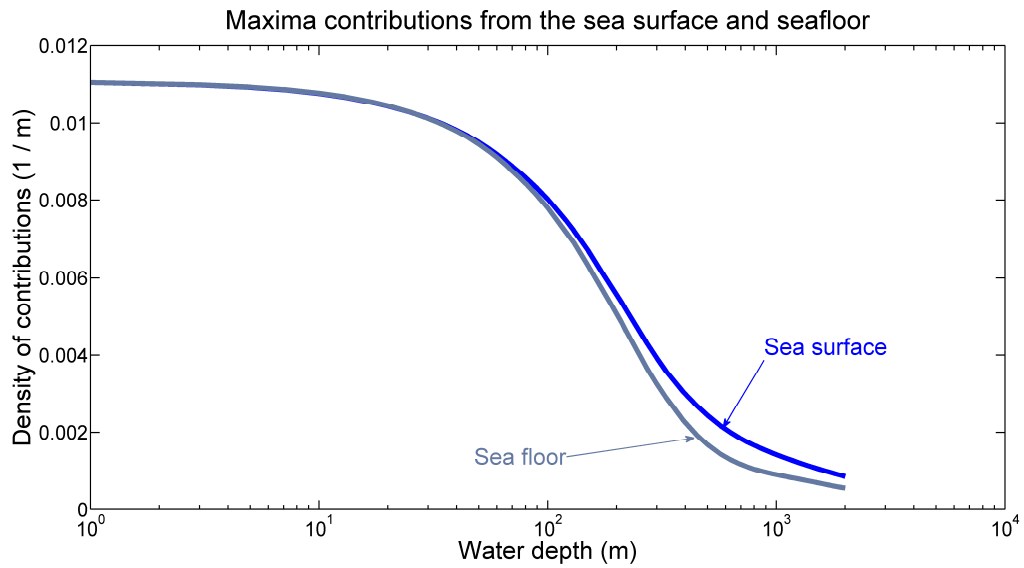
In Figure 18, images of the density of contributions from the sea is showed, which correspond to the integrand of the first integral in equation 20, including the factor behind the integral sign. Six images are presented for water depths from 2000 to 30 m, for each one of these images the vertical axis is the water depth and the horizontal axis is the offset distance. These depths cover both deep and shallow water scenarios. The model includes a thin resistive layer at depth as depicted in Figure 1b. Considered as functions of offset, the four classical zones of marine CSEM are clearly defined in the images. Zone I at short offsets is dominated by direct current effects. The sea being more conductive than the formations draws the currents upwards. The effects of induction overshadow the galvanic conduction in zone II. Then comes Zone III, which I associate with the airwave. Aside from the galvanic effect near the source, this zone is the most intense. Then comes the plane wave approximation as the fourth zone. Notice that zone III moves from long offsets for deep water to shorter offsets as the water depth decreases. However, for the shallowest depths this behavior seems to be driven by something else than the depth of the water because the migration towards the source stops at around 7000 m offset. Notice that the density of the contributions increases as the water depth decreases. However, this does not imply that the overall effect

of the sea also increases because the domain of the integral is also decreasing contributions from the air. Comparisons of the total contributions from the air, the sea and the sub-seafloor were made. As expected, the air contributions are many order of magnitude smaller than those from the sea and from the sub-seafloor. From now on, I will only consider the contribution from the sea and sub-seafloor.



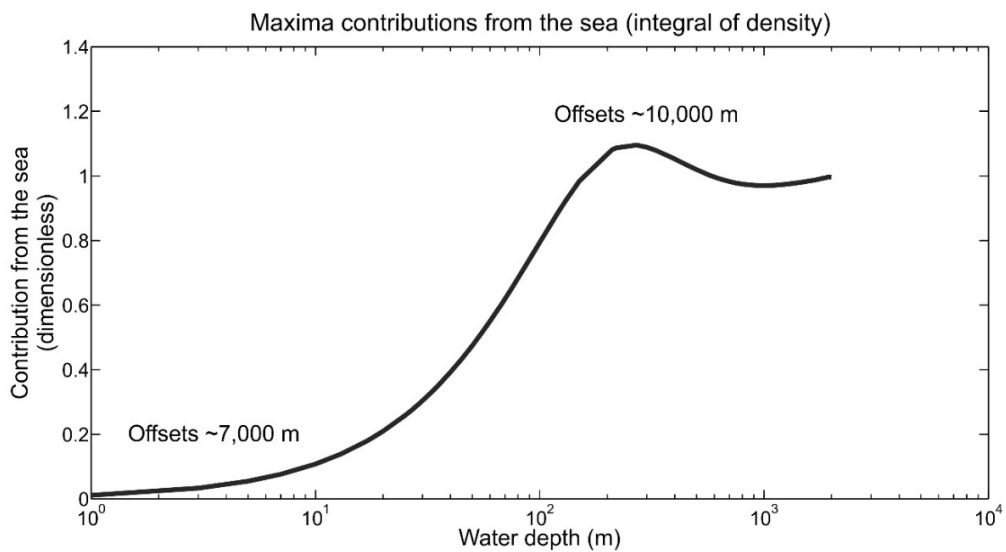
**Figure 18. Density of contributions from the sea for different water depths.** The density of contributions from the sea defines four zones. Zone I: direct current; Zone II: induction; Zone III: airwave; and Zone IV: plane wave. The arrows indicate how the airwave stops moving towards shorter offsets as the water depth decreases. The vertical scale represents water depth.

Figure 19 shows the density of contributions for two points within the sea for different water depths. One is at the sea surface and the other on the seafloor. The abscissa is the water depth and the ordinate is the maximum contribution along the offset axis in Figure 18. The curves summarize the increase in intensity of contributions seen in Figure 18 as the water depth decreases. The curves were obtained searching for the maximum along the offset axis, so the points on the curves potentially refer to different source-receiver separations. However, as seen in Figure 18 the maxima on the sea surface and the sea floor occur at about the same offsets, leaving aside zone I. The curves merge as the water depth decreases, as they should, since for zero depth they refer to the same point. The relevant thing here is that the curves remain finite and tend to a uniform value, implying a vanishing effect of the water column.



**Figure 19. Maxima contributions from the sea surface and seafloor.** This curve summarizes the sections shown in Figure 18 for the sea surface and seafloor.

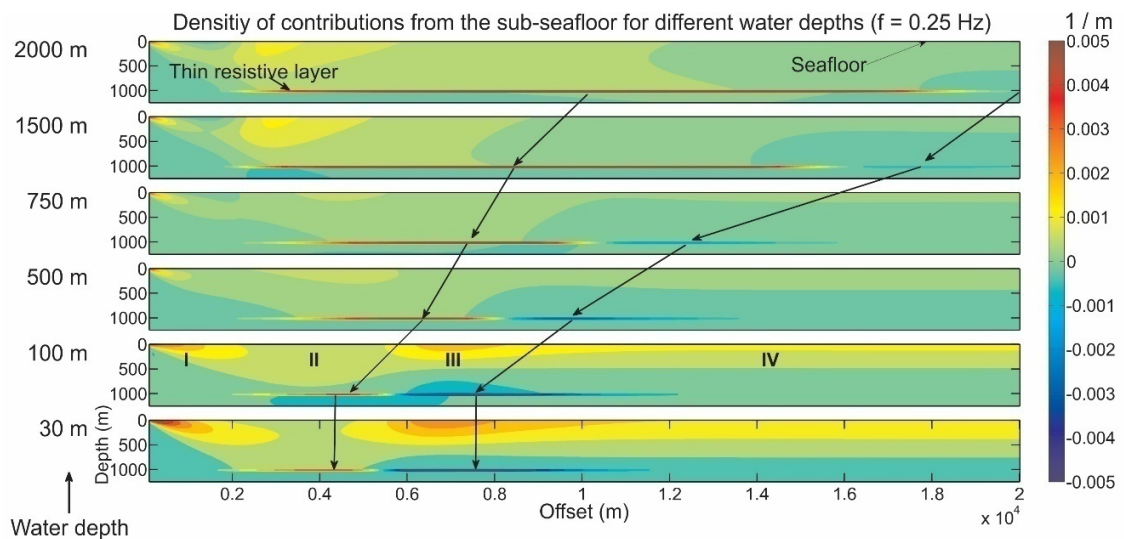
The total contribution of the sea is shown in Figure 20 for the same wide range of depths. The curve represents the integral of the density of contributions for each depth. It can be observed that the maximum contribution of the air wave happens for moderate water depths of around 300 m. From then on the effect decreases to zero as the water depth decreases, as it should, since the sea is disappearing.



**Figure 20. Maxima contributions from sea (integral of density).** This curve summarizes the sections shown in Figure 18. It shows the maximum of the total contribution from the sea as a function of the water depth.

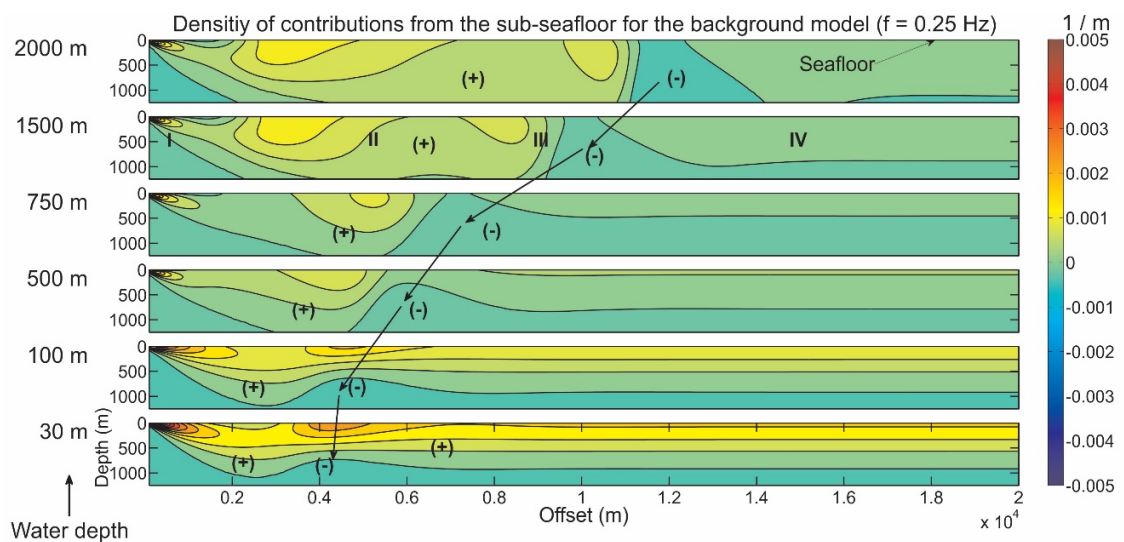
### 4.3 The sub-seafloor

Figure 21 presents the corresponding images of the density of contributions for the sub-seafloor. In this case, they represent the integrand of the second integral in equation 20. For these images the vertical axis represents depth below the seafloor. Zone I intensifies for shallow waters as the sea pulls less and less current upwards. As the water depth decreases zone II loses intensity and also loses offset domain where it is most intense. Zone III behaves similarly as in the sea; it stops migrating towards the source at around 7000 m offset. It was mentioned regarding the behavior of the airwave in the sea that something else apart from the sea must be driving its behavior. It is clear that this is the airwave itself but now in its materialization in the sub-seafloor. Together with the positive contributions on top of the formation, there is a new coupling with the resistive layer that becomes more intense as the water depth decreases. This coupling is negative and tends to cancel the overlying positive values. Perhaps this is the reason behind the belief that the airwave hinders severely the detection of the resistive layer. In fact, what it does is to deteriorate the resolution at depth (e.g., Connell and Key, 2013). There are two significant contributions from the layer, one positive at around 4000 m offset and one negative at around 7000 m. The positive one diminishes as the water depth decreases and the negative increases in intensity.



**Figure 21. Density of contributions from the sub-seafloor for different water depths.** The density of contributions from the sub-seafloor defines the same four zones as the contributions from the sea. Zone I associated with galvanic currents intensified as the water depth decreased since the effect of the sea decreases. The induction zone II decreases in intensity and also loses offset span as the water depth decreases. Comparing with Figure 18 the airwave migrates from the sea to the formation as the water depth decreases, but now it possesses an intense negative component. The vertical scale represents depth below the seafloor.

The appearance of negative contributions at depth for shallow waters can be traced back to the normal conditions in the background model. Figure 22 shows the corresponding contributions from the sub-seafloor for the background model. Comparing Figures 21 and 22, it can be observed that the positive and negative contributions at depth ( $\sim 1000$  m) in the background model are amplified by the presence of the resistive layer. Notice that the same four zones are already present but now they are shifted towards shorter offsets. The negative contributions, present for all water depths, stop migrating towards shorter offsets as the water depth decreases. Notice also that regardless of the presence of the thin resistive layer there is again a gradual accumulation of positive contributions above the negative concentrations.

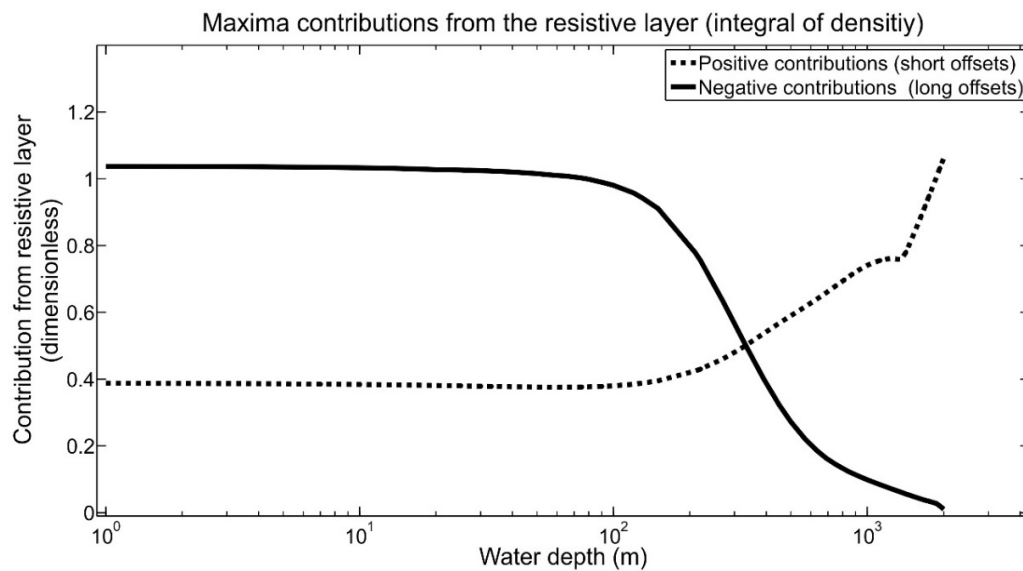


**Figure 22. Density of contributions from the sub-seafloor for the background model.** The density of contributions from the sub-seafloor for the background model defines the same four zones shown in Figures 18 and 21. One difference is that they occur over a shorter span of offsets and that there are no discontinuities at depth associated with the thin resistive layer. The frequency is  $f=0.25$  Hz, the same as for Figures 18 and 21. The seafloor is the reference depth and the vertical scale represents depth below the seafloor.

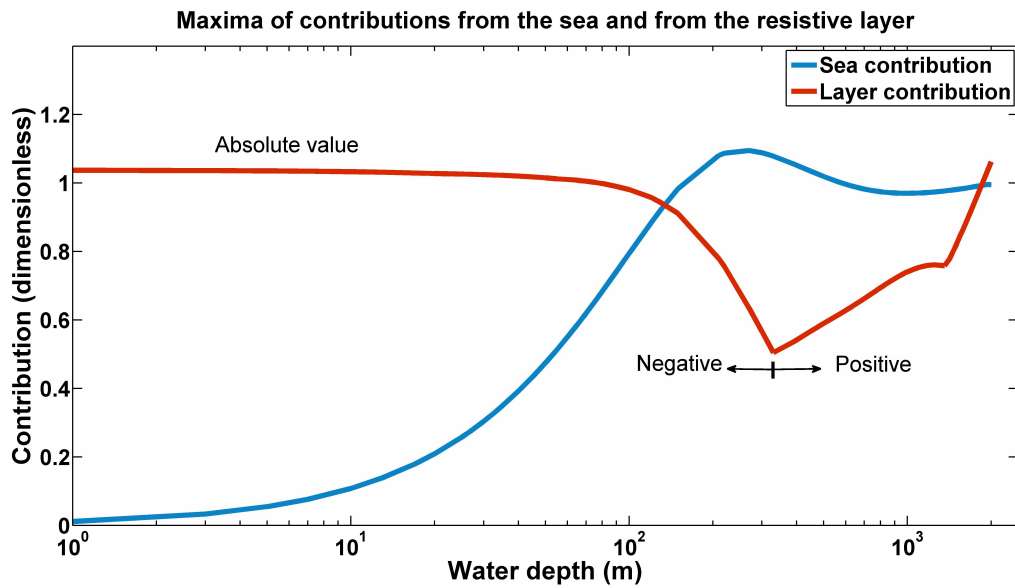
#### 4.4 The sea and the resistive layer

Figure 23 shows the contributions from the resistive layer for a wide range of water depths. It can be observed that the positive and negative contributions respond in opposite ways to the decrease in water depth. For depths of less than 100 m the negative contribution of the layer is of the same size as the

positive contribution for deep water. The curves cross at a water depth of around 300m, which is also the depth for the maximum contribution from the sea shown in Figure 19. This hints to the airwave as the origin of the decrease of the positive contribution and also of the increase of the absolute value of the negative. The comparison of the maximum of the two curves with that for the sea is shown in Figure 24. The curves now intersect at about 100 m water depth where the response of the layer overcomes that of the sea.



**Figure 23. Maxima contributions from the resistive layer (integral of density).** The positive and negative contributions from the resistive layer respond opposite to the decrease of the water depth. The curves cross at the water depth where the contribution from the sea is a maximum.



**Figure 24. Maxima of contributions from the sea and from the resistive layer.** Comparison of maxima contributions from the sea and from the resistive layer reveals that the response of the latter can be larger than that of the former for water depths below a critical value.

The above results are based on relative contributions to the electric field. To obtain the contributions to the electric field itself the electric fields are computed at the offsets of maxima contributions. As explained in relation to the use of equation 20, the relative contributions convert to contributions multiplying them by the amplitude of the electric field. Figure 25 shows the behavior of the electric field as a function of water depth. For the case of the sea, the amplitude of the field decreases with the water depth because the maxima in the sea migrate toward larger offsets. For shallow waters the curve stabilizes because the maxima in the sea stop migrating towards smaller offsets at about 7 km as shown in Figure 18. The curve for the resistive layer is more complicated due to the change in sign of the contributions. The jump around 300 m reflects the sudden migration in offsets of the maxima contributions. However, both curves converge at shallow waters because the maxima in the sea coincide in offsets with the maxima of the absolute values of the contributions from the resistive layer.

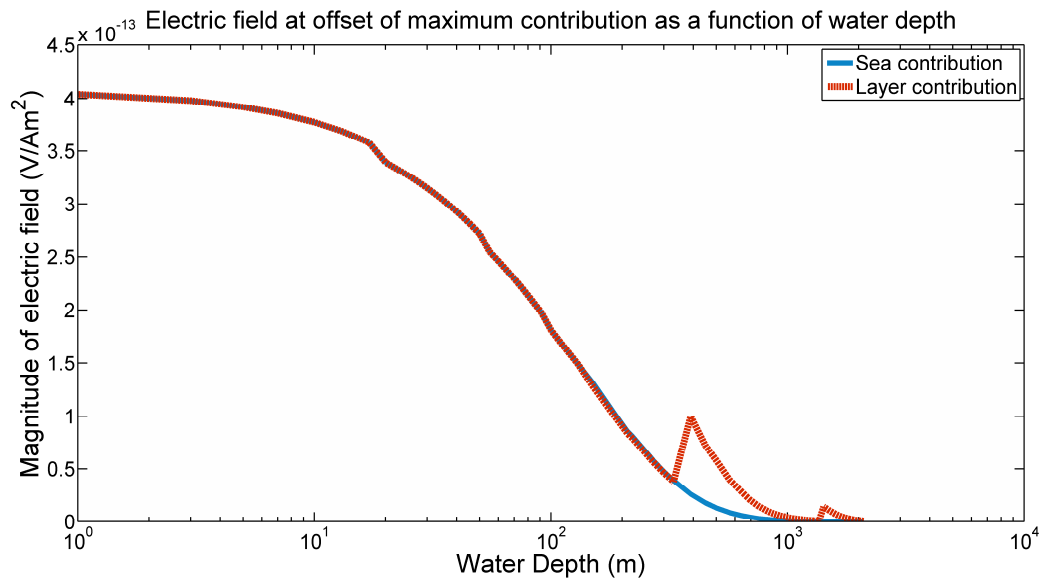


**Figure 25. Electric field at offset of maximum contribution as a function of water depth.** Amplitude of the electric field corresponding to the maxima of contributions from the sea and from the resistive layer.

Multiplying the curves of Figure 24 by the corresponding curves in Figure 25 we obtain the contributions of the sea and of the resistive layer are obtained in the units of the electric field. These are shown in Figure 26. Both curves stabilize as the water depths tend to zero, the one for the sea to zero and the one for the layer to a constant.

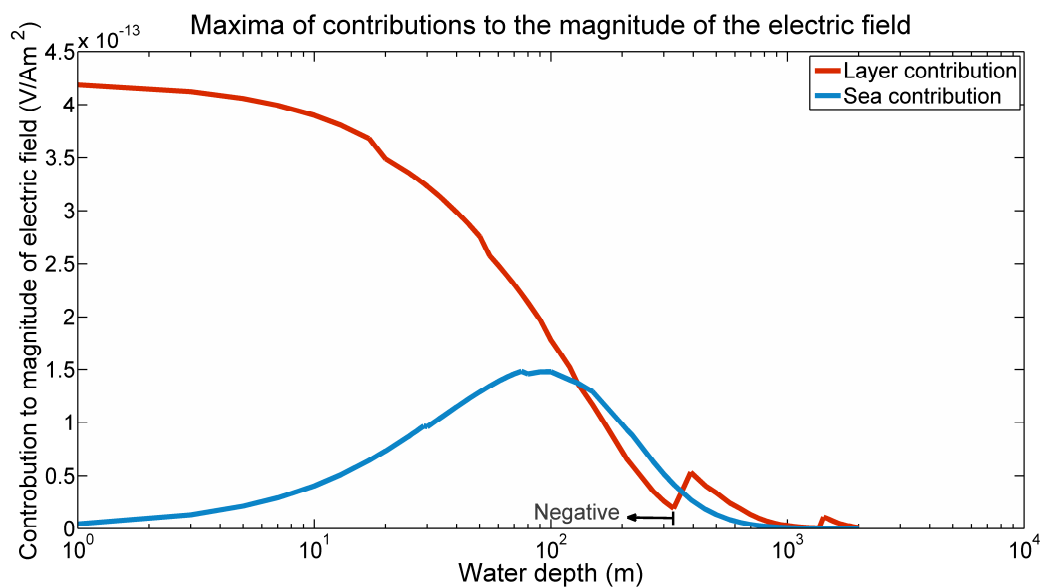


**Figure 26. Maxima of contributions to the magnitude of the electric field.** Maxima contributions from the sea and from the resistive layer as functions of water depth.

The water depth where the maximum of contributions from the sea occurs depends on frequency. In Figure 26 the maximum occurs at about 100 m. This corresponds to a frequency of 0.25 Hz when the top of the resistive layer is placed at 1000 m depth. Figure 27 shows how this depth changes for different frequencies and depths of the top of the resistive layer. In the first case, Figure 27a shows that the maximum migrates towards shallower depths as the frequency increases. The curves are normalized with respect to their own maximum to better illustrate the effect. I used frequencies from 0.1 to 4.0 Hz which correspond to skin depths in the sea from 800 to 140 m, respectively. In all cases the maxima occur at about the same fraction of the corresponding skin depths, indicating that the curves are scaled versions of each other, as they should. The scaling is not perfect because the model includes the resistive layer. However, as illustrated in Figure 27b the water depth of the maxima contribution is little affected by the depth of the layer. It thus have that for different frequencies and depths to the resistive layer the contributions from the sea have a local maximum but eventually tend to vanish as the water depth decreases.

Water depths larger than a skin depth in Figure 27 would define deep water scenarios. This is because the fields barely reach the air-water interface avoiding the effect of the air wave. The curves rise at about one skin depth when the air-water interface begins to make its presence felt. Eventually, the rise stops because the contributions must vanish as the water depth decreases to zero. This is because, to large offsets, the sea becomes a thin conductive layer when its thickness is smaller than a skin depth. One of the properties of a thin conductive layer is that its effects depend only on conductance, the product of conductivity and thickness e.g. Grant and West (1965). Since the conductivity of the sea remains the same its conductance necessarily vanishes with its thickness and also its effects on the total response (Figure 28). This further explains that the sensitivity to the detection of the resistive layer at depth stops falling as the water depth decreases as is in Figure 20.

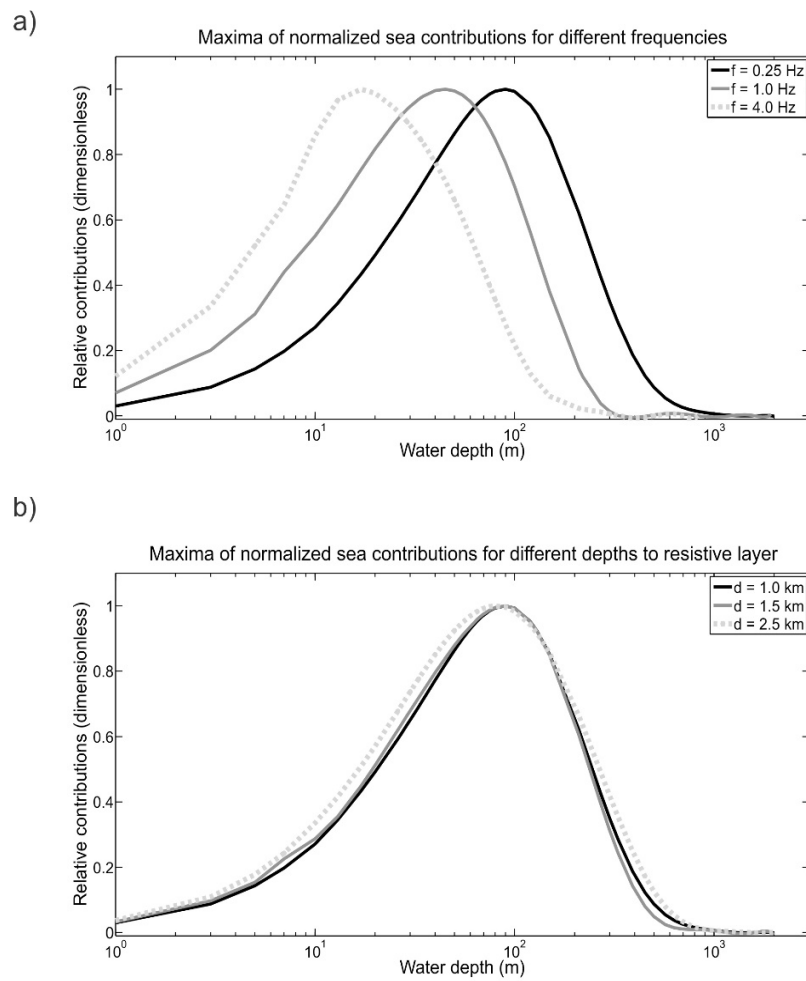


**Figure 27. Maxima of normalized sea contributions for different frequencies and different depths of the resistive layer.** a) The curves of maximum contribution from the sea for different frequencies are approximately scaled versions of each other. After a local maximum, all tend to vanish as the water depth decreases. b) The depth to the resistive layer has little effect on the location of the maximum contribution. The frequency used is 0.25 Hz.

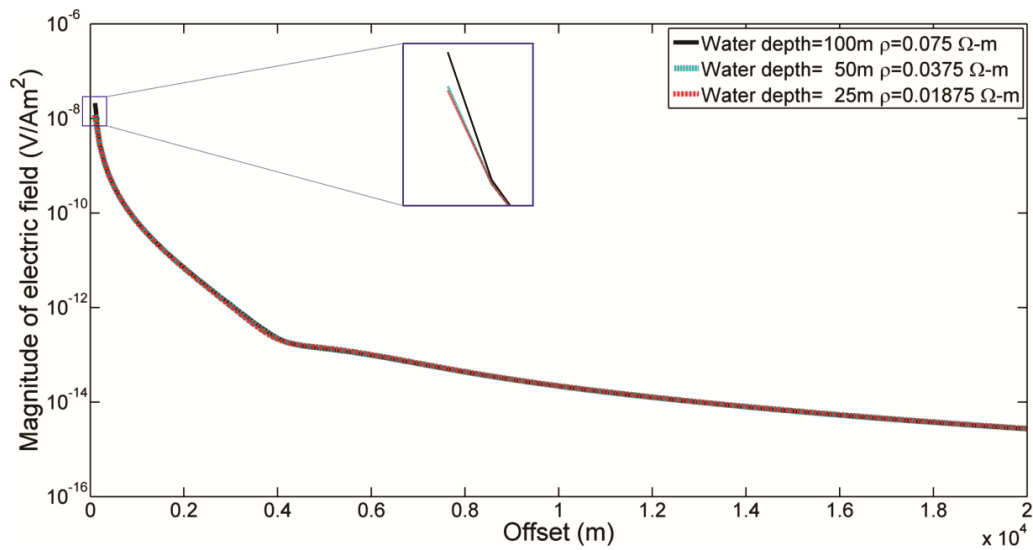


**Figure 28. Thin conductive layer.** Curves of electric field magnitude for the background model 1a, the three curves has the same conductance but with different thickness and resistivity in the water layer. The curves shows how in the limit, the sea becomes a thin conductive layer. This only happens in large offsets.

#### 4.5 The transition sea to land

The overall picture given above about the detection of a resistive layer in shallow waters can be summarized as follows. Looking back at the top image of Figure 21 there is no doubt that a deep water scenario is best suited for the detection of the resistive layer. The image shows a neat positive and uniform contribution from the layer for a very wide span of offsets. In fact, the resistive layer dominates the scenery. As the water depth decreases towards the bottom of the figure, this single signature decomposes into several regions of positive and negative contributions. Three contributions are positive and one is negative. Of particular interest is the negative contribution because it comes from the resistive layer and it grows as the water depth decreases. The overlying positive contribution at the top of the sub-seafloor that also grows as the water depth decreases is also of interest. While this is happening, the contribution from the sea decreases. Consequently, the sea is a vanishing agent in the phenomenology of the airwave and the detection of resistive layers in shallow waters. That is, the phenomena of shallow waters must be driven by a land view of the airwave. To test this hypothesis, I computed the contributions from the sub-seafloor for a zero water depth. The results are shown in Figure 29. It can be observed that the images for the 30 m water depth and no water at all are practically identical.

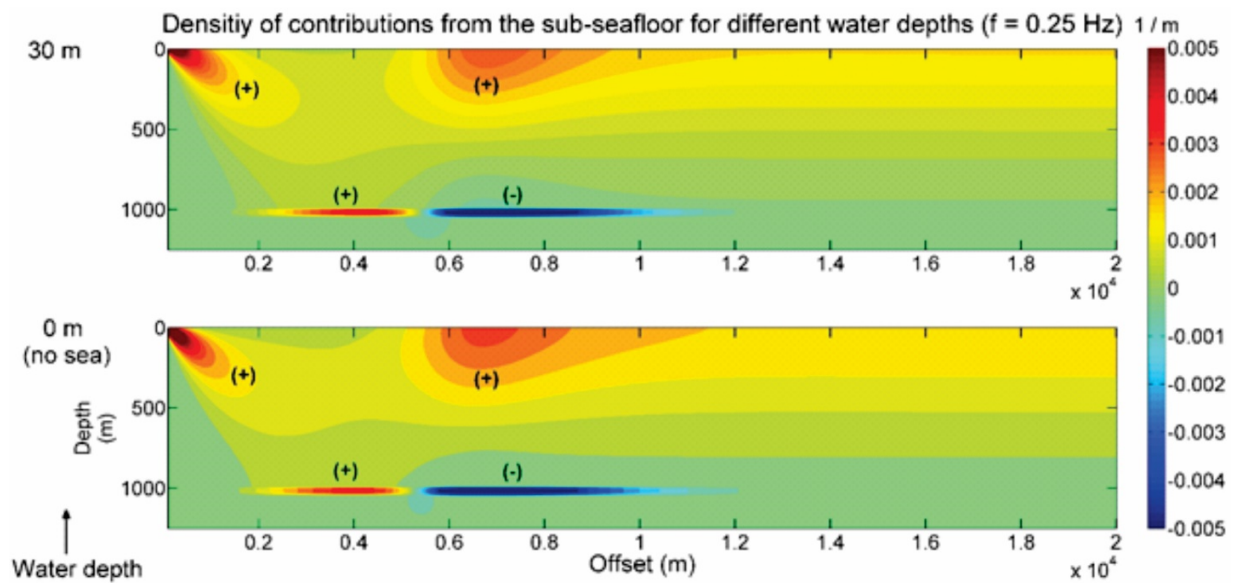


**Figure 29. Density of contributions from the sub-seafloor for different water depths.** The density of contributions from the sub-seafloor is practically identical for a water depth of 30 m (top) and no sea (bottom).

The effect of a vanishing sea discussed in relation to Figure 29 suggests a smooth transition from marine to land CSEM. This requires further discussion because there may be an abrupt change in the physical settings depending on how the transition is handled. One way to proceed is to change the resistivity of the sea by that of the air and perform the corresponding computations. Following this path, if the water vanishes, the galvanic coupling of the source with the conducting media disappears, because it was the water that provided the coupling. The abrupt change can be exaggerated for clarity by placing the source somewhere above the sea floor. If the water is vanished, the dipole source is in the air, an awkward setting for land CSEM. The other way is to strictly adhere to how both sea and land CSEM are performed in practice. That is, to simulate the two actual settings. Our simulation is illustrated in Figure 30. Model A has the dipole source and the dipole receiver placed on the sea floor under a very shallow sea 10 cm deep. The dipoles are not grounded to the sea floor, the water provides the galvanic coupling. This simulates the sea CSEM. Model B is intermediate between land and sea CSEM, with both a shallow sea and buried electrodes 10 cm below the sea floor. Model C is the same as model B but without the sea layer. This last model simulates the typical land CSEM. It can be observed that the three contribution sections are essentially identical, which confirms the earlier statement that the transition from sea to land CSEM is smooth.

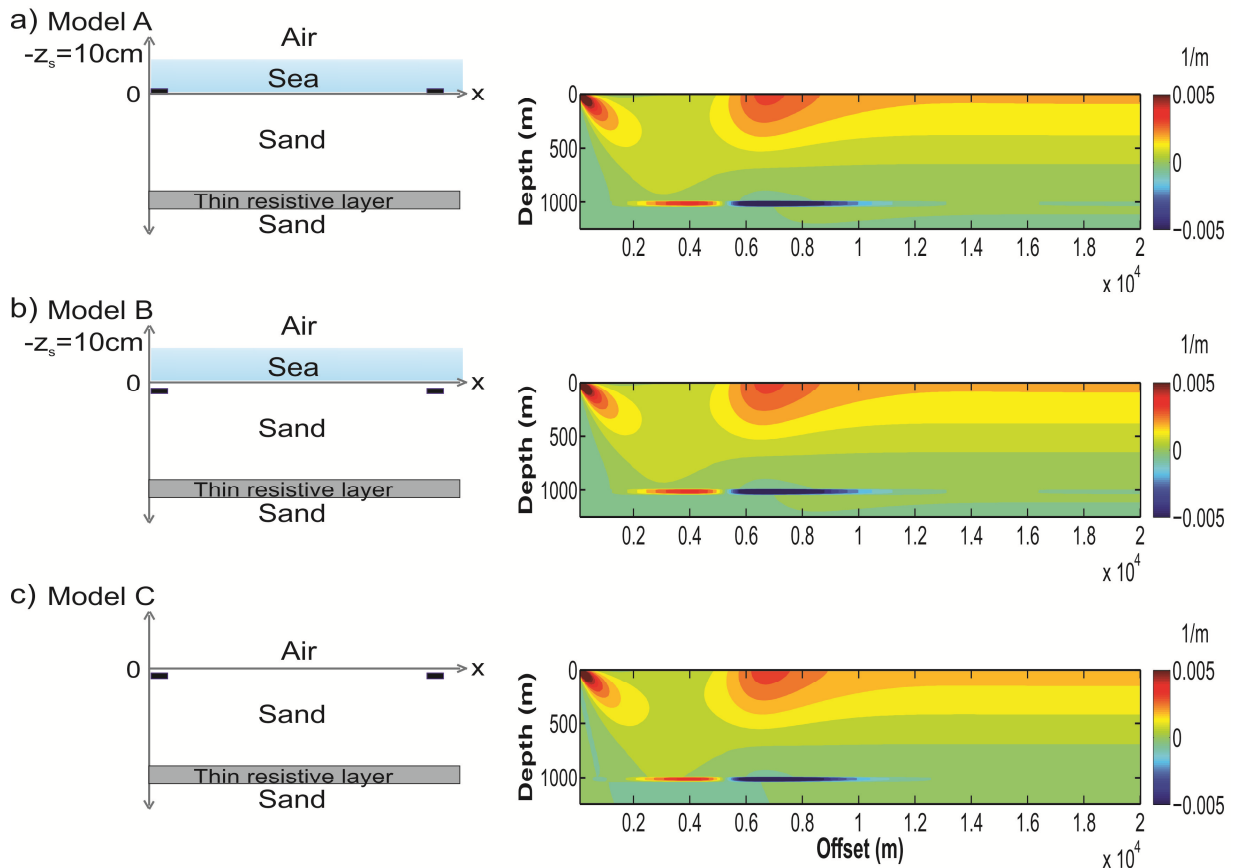


**Figure 30. Moving from marine CSEM to land CSEM.** Density of contributions from the sub-seafloor for three seemingly different models. Model A simulates sea CSEM for a very shallow sea 10 cm deep. Neither the source nor the receiver dipoles are grounded to the sea floor. Galvanic contact is provided by the sea water. Model B is the same as model A but both dipoles are buried 10 cm below the sea floor. Model C is the same as model B but with the sea water removed. This model simulates land CSEM. It can be observed that the density of contributions for the three seemingly different settings is essentially identical. This illustrates that the transition from sea to land CSEM is smooth. Notice that the figures on the left hand side are not to scale.

## 4.6 Conclusions

Our results support the claims of Mittet and Morten (2012, 2013) that shallow waters are no impediment for the detection of resistive layers at depth. However, the idea that the shallow sea acts as a secondary source is not supported because when the sea disappears the method remains detecting the resistive layer. This can be observed in Figure 29. This analysis is different from typical analyses made in marine CSEM where the field is separated into different signals (direct wave, horizontal wave, etc.). But, I also identified four zones depending on the offset from the source. First the DC approximation appears for the shortest offsets; the larger contributions come from the sea for large water depths because the

ocean, being thick and very conductive, draws most of the current upwards. However, for shallow water depths the sub-seafloor dominates. Then comes the induction zone dominated by the sub-seafloor. This zone extends towards larger offsets when a resistive layer at depth is included. The third zone is dominated by the sea and it is associated with the airwave. The fourth zone is in the plane wave approximation. In this last zone is where the resistive layer is not detected.

Nordskog and Amundsen (2007), and Mittet (2008) write that the air wave creates reverberations in very shallow water cases since multiple reflections in the water layer remain without attenuation. Our explanation for this argument is that when the skin depth is larger than the shallow water depth, the sea layer acts as a thin conductive layer, there are no reverberations in the sea. The last important thing is the smooth transition from the marine to land CSEM. In fact, all four zones are also present in land CSEM; this includes the third zone that is linked to the air-water interface.

## Chapter 5. Controversy and the physical nature of the airwave

---

### 5.1 Introduction

There seems to be some apparent contradictions in the last two chapters. Chapter III begins by assuming the long held idea that shallow waters severely hampers the detection of a resistive layer at depth. This motivated the improvement of the classical detectability by removing the effect of the sea and by other means. The chapter ends with definition of  $D_5$  which performs much better than the others but requires the recognition of an apparently new physical phenomenon at the surface of the sea that increases in intensity as the ocean thins out. Chapter 4, on the other hand, concludes that the effect of the sea must vanish as the sea disappears. The present chapter explains that these seemingly contradicting views are all a matter of perspective of what is considered normal, and of implicit assumptions hidden in the arguments. The chapter ends by offering a physical picture of what must be the airwave.

### 5.2 Deep waters as the reference

The electric field when both the source and receiver are at the bottom of the sea depends on the water depth, regardless of the presence of the resistive layer. This is illustrated in Figure 31. In fact, the field increases in both cases as the water depth decreases. In general terms, this is because the current density is confined to a decreasing volume. To emphasize this point, the magnitude of the field is normalized by that of the model without the resistive layer when the water depth is deepest, in this case 5 km. This is why the upper part of Figure 31b shows zeros for all offsets –the values are the logarithm base 10 of the relative amplitudes. This means that deep waters have been reached since the electric field at the bottom of the sea does not change at those in that ranges of water depths. For shallower depths the fields increase for all water depths, particularly for large offsets. Figure 31a shows the electric field for the model with the resistive layer normalized exactly as Figure 31b. That is, by the field of the deepest water of the model without the layer. It can be observed that the images are almost identical except at the deepest waters. Figure 32 shows the difference of the two images; that with the resistive layer divided by that without it. Notice that the previous normalization cancels out. It can be observed that the ratio, which is nothing else than the classical definition of  $D_1$  for *detectability*, is largest for deep waters and levels off as the water level decreases. This drop in the values of  $D_1$  was thought to be due to the airwave;

something that appears and increases in intensity as the water depth decreases. This effect must come from the air so the term is from airway.

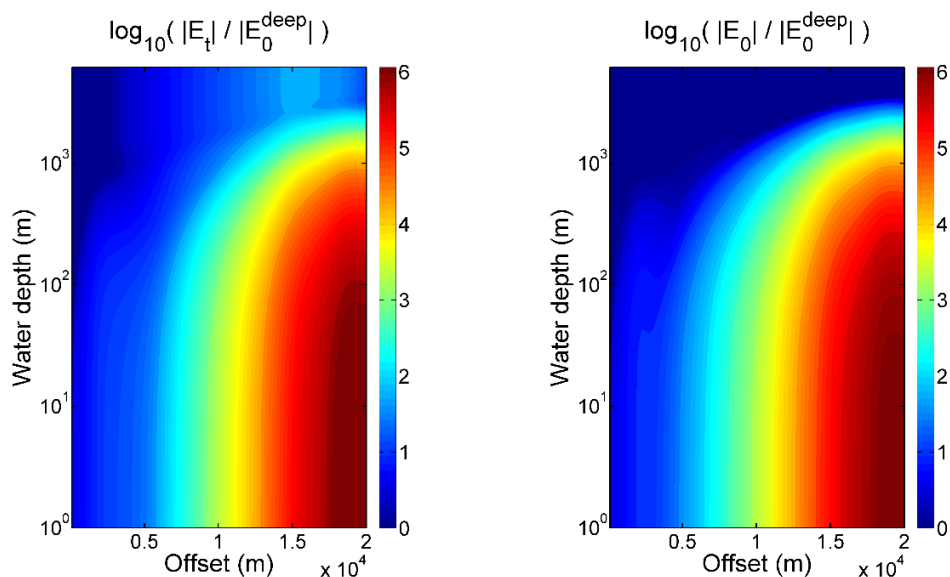


**Figure 31. Normalization of the electric field amplitude to deep water.** The electric field on the sea floor for different water depths is normalized using the values for the deepest water of the model without the resistive layer. a) Electric field corresponding to the model with the resistive layer. b) Electric field corresponding to the model without the resistive layer.

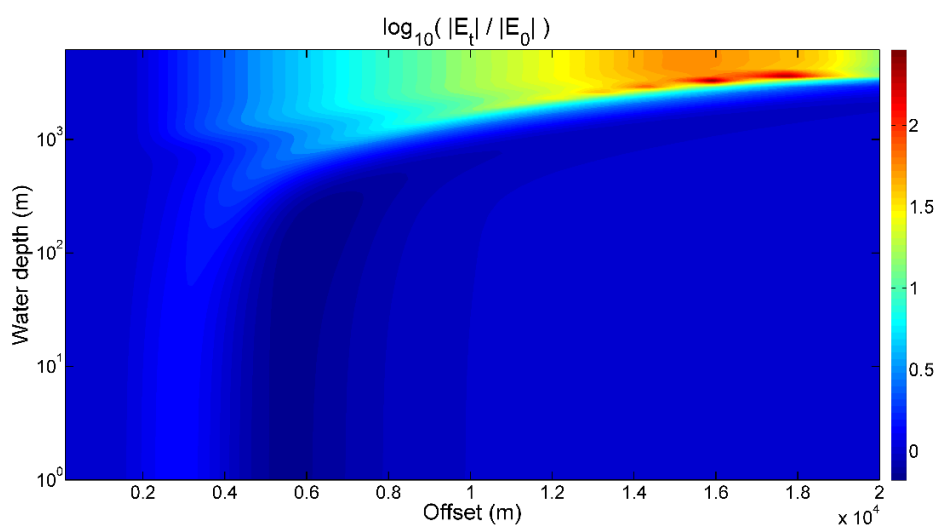


**Figure 32. Difference of image of Figure 30b to that of Figure 31a.** This figure is the typical *detectability* formula for different offsets and water depths.

### 5.3 Shallow waters as the reference

The contrasting normalization of Figure 31 is to use shallow water response as reference. The result of this normalization is shown in Figure 33. It can be observed how the presence of the resistive layer is clearly manifested in Figure 33a for shallow waters, without any need of normalization with respect to the background response of Figure 33b. Notice that the anomalous response at shallow waters happens at around 5 km offset, at the same region as the ratio in Figure 32. Notice also that the difference of the image in Figure 33a normalized by that of Figure 33b must be the same as Figure 32. That is, deep waters dominate the scene.

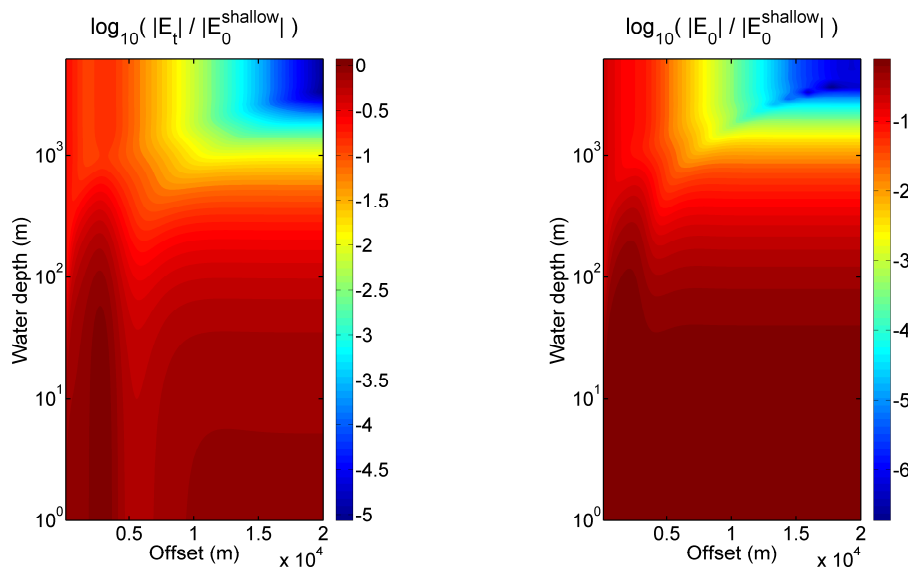


**Figure 33. Normalization of the electric field amplitude to shallow water.** The electric field on the sea floor for different water depths is normalized using the values for the shallowest water of the model without the resistive layer. a) Electric field corresponding to the model with the resistive layer. b) Electric field corresponding to the model without the resistive layer.

## 5.4 Deep versus shallow waters

The use of differences between responses, although a straightforward and a very natural approach, was not explored until recently by Mittet and Morten (2012, 2013). Their results were reviewed in chapter 3. They inspected the differences normalized by a combination of relative errors and variable error floors using definition  $D_5$ . Because of this combination of different normalizing elements it is difficult to understand the difference between deep and shallow waters. Figure 34 shows the differences between responses normalized in a) by the field of the model with the resistive layer and b) by the background field. Notice that there seems to be two regimes, one for deep and the other for shallow waters. The division is marked by the skin depth in the ocean, which is 550 m. Notice that *detectability* remains almost without change below this depth, and that the values are comparable to those for deep waters. The only change is that the higher values are located at a narrow vertical band for short offsets. This last remark about the vertical band means that the depth of penetration remains the same regardless of the water depth.

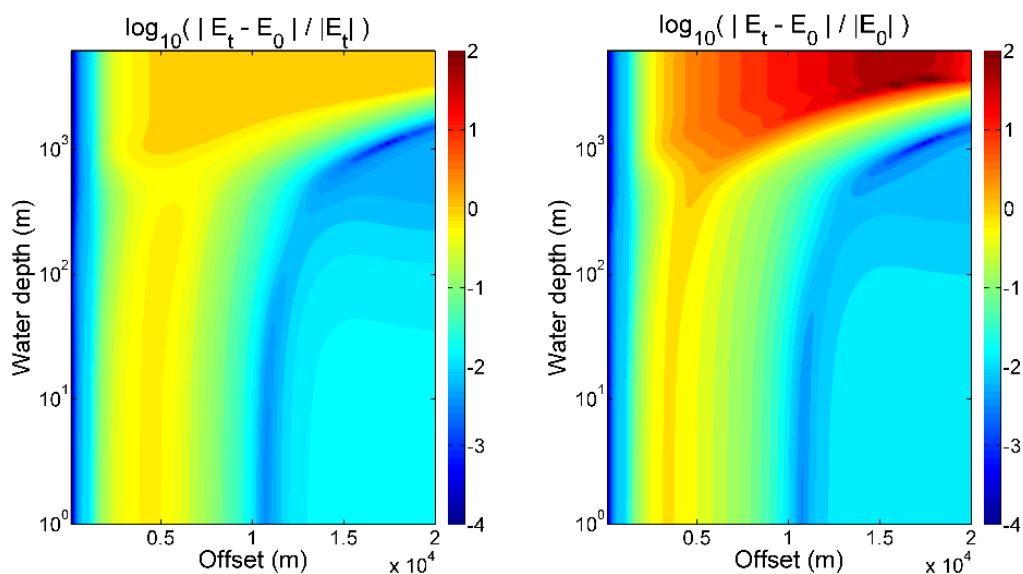


**Figure 34. Difference of response normalized by difference with and without resistive layer.** a) Difference of responses normalized by that without the resistive layer. b) Difference of responses normalized by that with the resistive layer. The images correspond to the magnitude of the differences.

Another possibility for comparing responses is to consider the straight differences, and to simply normalize by those of deep and shallow waters for scaling reasons. These are shown in Figure 35 for the two types of normalization. Notice that, in this case, one cannot but accept the possibility that shallow waters are even better for detecting the resistive layer at depth.

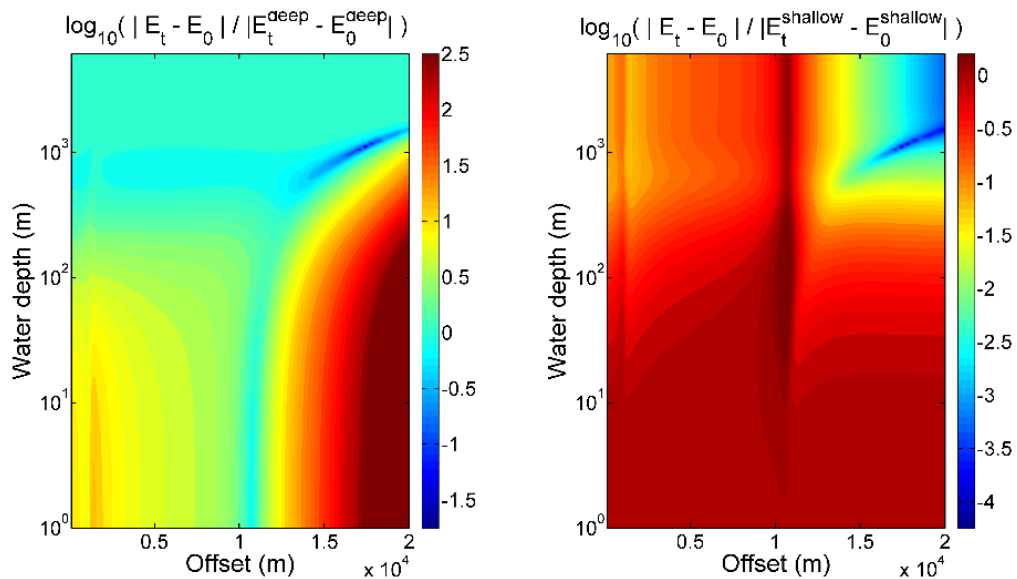


**Figure 35. Difference of response normalized by difference with and without resistive layer in deep water. a)** Difference of responses normalized by that of the deepest water. **b)** Difference of responses normalized by that of the shallowest water.

## 5.5 Electric charges on the surface of the sea: the actual airwave.

Let us consider what actually happens in physical terms when going from deep to shallow waters and vice versa. When the sea is much thicker than the skin depth in the ocean, there cannot be anything happening on the surface of the sea. As one moves towards shallower waters of the order of the skin depth in the ocean, there must appear electric charges on the surface of the sea. This is because they are the ones responsible for preventing the electric current that flows within the ocean to cross the air-water interface. They make the horizontal electric field to be parallel to the surface of the water. That is, the vertical electric field below the surface must be nil. In the air, just above the water the vertical field cannot

be zero (see Appendix B). The appearance of this vertical field is the only electrical change on the water surface that can be associated with changes in the water depth.

Up to now, the airwave is more a hypothesis than a physical real phenomenon, brought about to explain the behavior of the electric field at the bottom of the sea. The rest of the chapter shows that the charges on the surface of the sea fit very well the properties assigned to the airwave. The vertical electric field expressed as surface density of charge is shown in Figure 36. The charges decrease with offset and increase when the water depth diminishes, as they should. The shallower the sea the less space available for the circulation of the current, and therefore the more charge needed to make this possible. The charges fall with offset simply because they are farther from the source. One of the images is for the model without the resistive layer and the other includes the layer. Notice that they are practically identical, which implies that the layer influences the whole distribution of currents a lot less than the sea. In particular, that the layer influences very little the vertical electric field on top of the ocean. This is one of the reasons why the vertical electric field is not measured on top of the sea: it has no information about the resistive layer. At the bottom of the sea it is another matter.

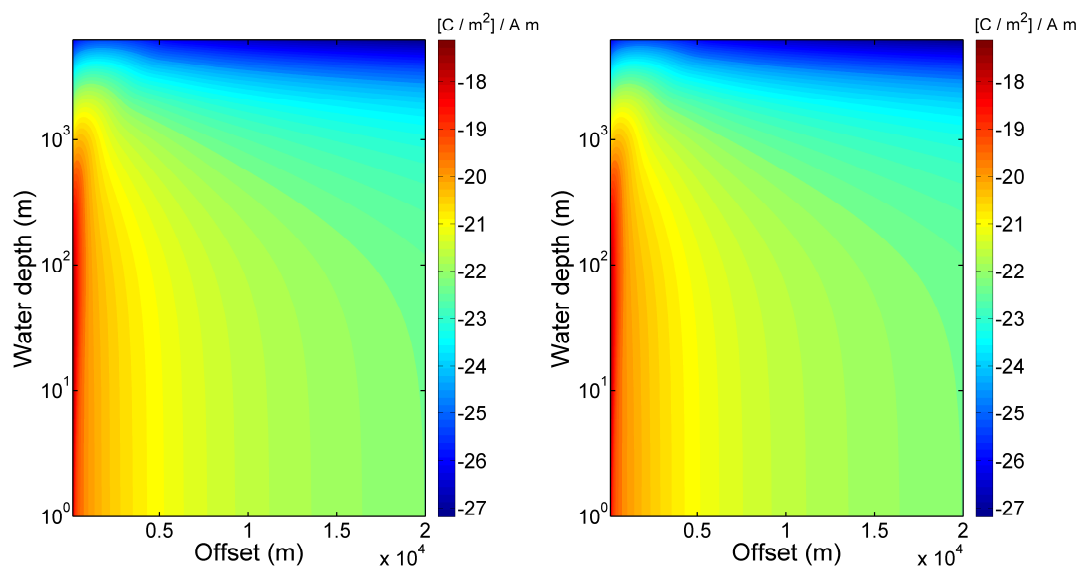


**Figure 36.** The images represent charges on the surface of the sea for different water depths. a) Normalized with respect to shallow waters. B) Normalized with respect to deep waters.

The next four figures are elaborations of the images in Figure 36 to show more clearly how the charges behave for different water depths. The same type of normalizations as before is used to neutralize

the strong decay of the charges with offset. I normalize with respect to the charges for both the shallowest and deepest waters. In the present case the results are remarkable. Figures 37 and 38 present the normalized charges for the case without the resistive layer and that including the layer, respectively. Figure 36 shows the charges normalized with respect to the deepest waters. It can be observed that the charge density increases several orders of magnitude as the water depths decrease, as it should. The remarkable feature is that, after relatively short offsets, the relative charges present a uniform behavior as the offset increases for all water depths, at their own level. The other remarkable thing is that the charges remain almost the same for shallow waters up to a depth of about the skin depth in the sea of 500 m. This implies that adding substantial water to a land survey the charges on top of the sea are about the same as those with no sea. Both images normalized with respect to the deep and shallow waters offer the same picture, and also do the images in Figure 38 for the model with the resistive layer. Again, notice that with or without the layer the charges are very much the same.

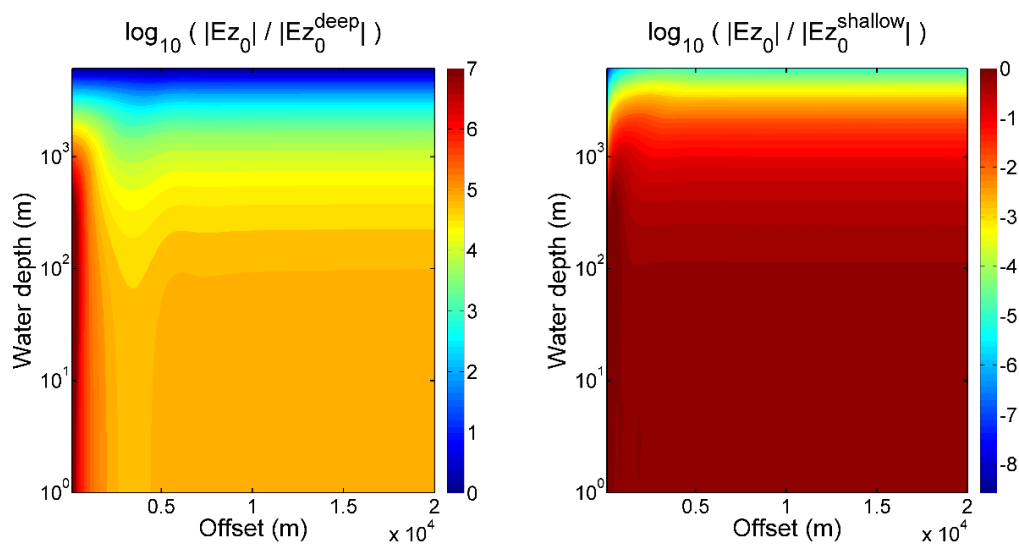


**Figure 37. Surface charge density on top of the sea for different water depths in the background model. a) Normalized with respect to deep waters. b) Normalized with respect to shallow waters.**

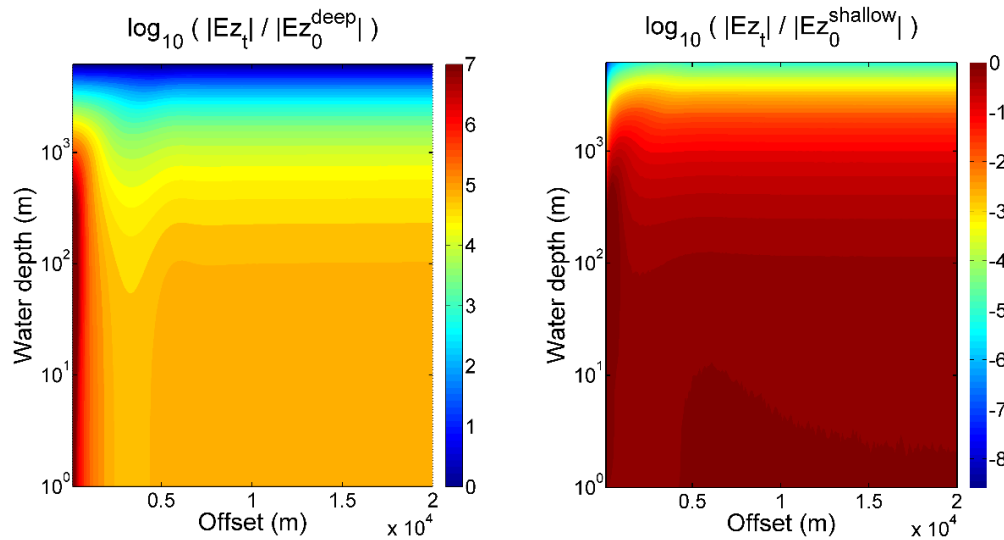


**Figure 38. Surface charge density on top of the sea for different water depths in the resistive layer model. a)** Normalized with respect to deep waters. **b)** Normalized with respect to shallow waters.

## 5.6 Conclusion

Several ways of comparing the response of the model with and without the resistive layer have been reviewed, in order to understand the physical nature of what has been called the air-wave. It is clear that below one skin depth all the definitions of the *detectability*, remain almost the same regardless of the water depth. As discussed in chapter 4, the effect of the sea must decrease as the water depth vanishes, and at the same time the effect of the layer increases. This result contrasts with the explanation of Mittet and Morten (2013), that both responses increase as the water vanishes. The reason that both responses increase is that the current density in both cases is increasingly confined in a smaller space. The blue band of zeroes in Figure 34 around 10 km offset corresponds to equal responses. Beyond this point, the layer is undetectable for shallow depths. However, for shorter offsets of around 5 km the layer is detectable all the way from no water at all to deep waters.

## Chapter 6. Conclusions

---

### 6.1 Conclusions

The present analysis was motivated by a growing conceptual gap between land and marine CSEM methods. It rests on a theory by which a marine CSEM data can be decomposed into two or more contributions. In the analysis, I identified four zones depending on the offset from the source. First appears the direct current approximation for the shortest offsets; the larger contributions come from the sea for large water depths because the ocean, being thick and very conductive, draws most of the current upwards. However, for shallow water depths the sub-seafloor dominates. Then comes the induction zone dominated by the sub-seafloor. This zone extends towards larger offsets when a resistive layer at depth is included. The third zone is dominated by the sea and it is associated with the airwave, which has been considered to have an inhibiting effect on the detection of the resistive layer at depth. The fourth zone is in the plane wave approximation. All four zones are also present in land CSEM; this includes the third zone that is linked to the air-water interface. Our analysis shows that there is a smooth transition from deep waters to no water at all. For shallow waters the origin of the airwave effects gradually migrates from the sea to the sub-seafloor, or opposite, from the sub-seafloor to the top of the sea. Neither the sea nor the sub-seafloor is a secondary agent in allowing the detection of resistive layers at depth in shallow waters. The current view that the shallow sea acts as a source that energizes the resistive layer cannot hold for all water depths, since in the limit there is no sea. There is a transitory behavior. The present explanation reinforces and extends the recent view that a resistive layer at depth is effectively detectable at shallow waters. The same result is obtained by identifying the airwave with the surface density of charge over the sea surface.

The density of charge over the sea surface is the only physical phenomenon that could possibly be associated with what has been termed the airwave. It has the same properties of making the horizontal electric field grow for shallow waters, with or without the resistive layer. In general, this increase in the electric field occurs because the current density is forced to circulate in a smaller space in shallower waters. The physical phenomenon that makes the current density at the surface of the sea to be horizontal is the presence of this surface charge density. Results show that these charges actually increase for shallow waters, as they should. This shows that the same phenomenon –the airwave- that used to be invoked to explain the failure of marine CSEM in shallow waters, is now responsible for the resurgence of shallow waters as an asset for the recovery of a resistive layer at depth.

An analysis like the present one was needed because according to the conflicting airwave argument land CSEM would be impossible, or nearly impossible; and this is not true. The other contradictory argument claims that a shallow sea acts as a secondary source that couples with the resistive layer, is also pessimistic. This is because it leaves the land CSEM without secondary sources. On the other hand, for decades, land CSEM have been proved to be successful in detecting conductive and resistive layers. Instead of going from sea to land, which is confusing, I went here from land to sea. The result is that shallow seas have almost no effect with respect to land CSEM. The pessimistic and unrealistic extrapolations from marine to land CSEM disappear.

It is expected that the present analysis contributes to the unification of marine and land CSEM concepts in what is and must be one and the same subject.

## 6.2 Future work

While this thesis has solved some paradigms and demonstrated a deeply analysis in the CSEM method, the results from this work focus on the  $E_x$  amplitude and leaves many approaches than could be done whether taking into account the results or comments of this thesis as start point. Some of them are:

- Extending this work to the phase of in-line and to other components of the electric field, as well as to the three components of the magnetic field.
- To make a comparative analysis of the charge density on the surface of the sea with that on the sea floor and on both interfaces of the resistive layer.
- To explore the potential of the frequency-derivative formulation as a more sensitive approach than the straight use of the electric field in the inversion of the data.

## References

---

- Amundsen, L., Løseth, L., Mittet, R., Ellingsrud, S., Ursin, B. 2006. Decomposition of electromagnetic fields into upgoing and downgoing components. *Geophysics*, 71(5), G211–G223. doi:10.1190/1.2245468.
- Barry, P., Goldmann, R. 1988. A recursive evaluation algorithm for a class of Catmull-Rom splines. *ACM Siggraph Computer Graphics*, 22, 199–204. doi:10.1145/378456.378511.
- Bording, R.P., Lines, L.R. 1997, Seismic modeling and imaging with the complete wave equation. Society of Exploration Geophysicists Course Notes No. 8, Oklahoma. doi:10.1190/1.9781560801870.
- Calderón-Moctezuma, A., Gómez-Treviño E., Gallardo L. A. 2017. Splitting marine controlled-source electromagnetic responses into sea and seafloor contributions: Grounding the air wave. *Geophysics*. 82(6), 1-9. doi:10.1190/GEO2016-0277.1.
- Chave, A.D., Cox, C.S. 1982. Controlled electromagnetic sources for measuring electrical conductivity beneath the oceans, 1. Forward problem and model study. *Journal of Geophysical Research*, 87, 5327–5338. doi:10.1029/JB087iB07p05327 .
- Chen, J., Alumbaugh, D.L. 2011. Three methods for mitigating airwaves in shallow water marine controlled-source electromagnetic data. *Geophysics*, 76(2), F89-F99. doi:10.1190/1.3536641.
- Christensen, N.B. 2014. Sensitivity functions of transient electromagnetic methods. *Geophysics*, 79(4), E167-E182. doi:10.1190/geo2013-0364.1.
- Connell, D., Key, K. 2013. A numerical comparison of time and frequency-domain marine electromagnetic methods for hydrocarbon exploration in shallow water. *Geophysical Prospecting*, 61, 187-199. doi:10.1111/j.1365-2478.2012.01037.
- Constable, S., Weiss, C.J. 2006. Mapping thin resistors and hydrocarbons with marine EM methods. Insights from 1D modeling. *Geophysics*, 71(2), G43–G51. doi:10.1190/1.2187748.
- Cox, C.S., 1981. On the electrical conductivity of the oceanic lithosphere. *Physics of the Earth and Planetary Interiors*, 25, 196–201. doi:10.1016/0031-9201(81)90061-3.
- Dosso, S.E., Oldenburg, D.W. 1991. The similitude equation in magnetotelluric inversion: *Geophysical journal international*, 106, 507-509. doi:10.1111/j.1365-246X.1991.tb03910.
- Eadie, T. 1980. Detection of hydrocarbon accumulations by surface electrical methods - a feasibility study: M.S. thesis, University of Toronto. 93 pp.
- Edwards, R.N., Nobes, D.C., Gómez-Treviño, E. 1984. Offshore electrical exploration of sedimentary basins. The effects of anisotropy in horizontally isotropic, layered media. *Geophysics*, 49(5), 566-576. doi:10.1190/1.1441691.
- Eidesmo, T., Ellingsrud, S., MacGregor, L.M., Constable, S., Sinha, M.C., Johansen, S., Kong, F.N., Westerdahl, H. 2002. Sea Bed Logging (SBL), a new method for remote and direct identification of hydrocarbon filled layers in deepwater areas. *First Break*, 20, 144–152.

- Esparza, F.J., Gómez-Treviño, E. 1996. Inversion of magnetotelluric soundings using a new integral form of the induction equation. *Geophysical Journal International*, 127, 452-460. doi:10.1111/j.1365-246X.1996.tb04733.
- Esparza, F.J., Gómez-Trevino, E. 1997. 1-D inversion of resistivity and induced polarization data for the least number of layers. *Geophysics*, 62(6), 1724-1729. doi:10.1190/1.1444272.
- Freund, R.W., Nachtigal, N.M. 1994. An implementation of the QMR method based on coupled two-term recurrences. *SIAM Journal on Scientific Computing*, 15(2), 313-337. doi:10.1137/0915022.
- Gallardo, L.A., Meju, M.A. 2004, Joint two-dimensional DC resistivity and seismic travel time inversion with cross-gradient constraints, *Journal of Geophysical Research*, 109, B03311, doi:10.1029/2003JB002716.
- Gill, P.E., Murray, W., Wright, M.H. 1981. *Practical Optimization*, Academic Press, NewYork.
- Gómez-Treviño, E. 1987a. Nonlinear integral equations for electromagnetic inverse problems. *Geophysics*, 52(9), 1297-1302. doi: 10.1190/1.1442390.
- Gómez-Treviño, E. 1987b. A simple sensitivity analysis of time-domain and frequency-domain electromagnetic measurements. *Geophysics*, 52(10), 418-423. doi: 10.1190/1.1442254.
- Gomez-Treviño, E. 1996. Approximate depth averages of electrical conductivity from surface magnetotelluric data: *Geophysical Journal International*, 127, 762-772. doi: 10.1111/j.1365-246X.1996.tb04055.x.
- Gómez-Treviño, E., Edwards, R.N. 1983. Electromagnetic soundings in the sedimentary basin of southern Ontario-A case history. *Geophysics*, 48(3), 311-330. doi: 10.1190/1.1441470.
- Gómez-Treviño, E., Esparza, F.J. 2014. What is the depth of investigation of a resistivity measurement?. *Geophysics*, 79(2), W1-W10. doi: 10.1190/geo2013-0261.1.
- Gómez-Treviño, E., Esparza, F. J., Muñiz, Y., Calderón, A. 2014. The magnetotelluric transverse electric mode as a natural filter for static effects: Application to the COPROD2 and COPROD2S2 data sets. *Geophysics*, 79(2), E91-E99. doi: 10.1190/geo2012-0522.1.
- Gómez-Treviño, E., Flores, C. 2015. Alternative theory for signal contribution sections and depth of investigation characteristics in electrical prospecting. *Geophysical Prospecting*, 63, 740-749. doi:10.1111/1365-2478.12214.
- Grant, F.S., West, G. F. 1965. *Interpretation theory in Applied Geophysics*. McGraw-Hill, New York.
- Graves, R. 1996. Simulating seismic wave propagation in 3D elastic media using staggered-grid finite differences. *Bulletin of the Seismological Society of America*, 86, 1091-1106.
- Higdon, R.L. 1991. Absorbing boundary conditions for elastic waves. *Geophysics*, 56, 231-241. Doi:10.1190/1.1443035.
- Ixaru, L.Gr., Berghe, G.V 2004. *Exponential Fitting*. Kluwer Academic Publishers.

- Jaysaval, P., Shantsev, D., Kethulle de Ryhove, S. 2014. Efficient 3-D controlled-source electromagnetic modelling using an exponential finite-difference method. *Geophysical Journal International*, 203(3), 1541-1574. doi: 10.1093/gji/ggv377.
- Key, K. 2009. 1D inversion of multicomponent, multifrequency marine CSEM data: Methodology and synthetic studies for resolving thin resistive layers. *Geophysics*, 74(2), F9-F20. doi: 10.1190/1.3058434.
- Kristek, J., Moczo P., Archuleta, R.J. 2002. Efficient methods to simulate planar free surface in the 3D 4th-order staggered-grid finite-difference schemes. *Studia Geophysica et Geodaetica*, 46(2), 355–381.
- Liu, Q., Tromp, J. 2006. Finite-Frequency Kernels Based on Adjoint Methods. *Bulletin of the Seismological Society of America*, 96(6), 2383-2397. doi:10.1785/0120060041.
- Liu, Y., Sen, M.K. 2010. A hybrid scheme for absorbing edge reflections in numerical modeling of wave propagation. *Geophysics*, 75 (2), A1–A6. doi: 10.1190/1.3295447.
- Løseth L. 2011. Insight into the marine controlled-source electromagnetic signal propagation. *Geophysical Prospecting*, 59, 145-160. doi: 10.1111/j .1365-2478.2010.00898.
- Maaø, F., Nguyen, A. 2010. Enhanced subsurface response for marine CSEM surveying. *Geophysics*, 75, A7–A10. doi:10.1190/1.3377054.
- McGillivray, P.R., Oldenburg, D.W., Ellis, R.G., Habashy, T.M. 1994. Calculation of sensitivities for the frequency-domain electromagnetic problem. *Geophysical Journal International*, 116 (1), 1-4 doi:10.1111/j.1365-246X.1994.tb02121.x.
- Mittet, R. 2008. Normalized amplitude ratios for frequency-domain CSEM in very shallow water. *First Break*, 26, 47-54.
- Mittet, R., Morten J.P. 2012. Detection and imaging sensitivity of the marine CSEM method. *Geophysics*, 77(6), E411-E425. doi: 10.1190/ geo2012-0016.1.
- Mittet, R., Morten, J.P. 2013. The marine controlled-source electromagnetic method in shallow water. *Geophysics*, 78, E67-E77. doi: 10 .1190/geo2012-0112.1.
- Moczo, P., Kristek, J., Halada, L. 2000. 3D fourth-order staggered-grid finite-difference schemes: stability and grid dispersion, *Bulletin of the Seismological Society of America*, 90(3), 587–603. doi: 10.1785/0119990119.
- Moczo, P., Kristek, J., Vavrycuk, V., Archuleta, R.J., Halada, L. 2002. 3D heterogeneous staggered-grid finite-difference modeling of seismic motion with volume harmonic and arithmetic averaging of elastic moduli and densities. *Bulletin of the Seismological Society of America*, 92(8), 3042–3066. doi:10.1785/0120010167.
- Nocedal, J., Wright, S. 2006. *Numerical optimization*. (2da ed.) Springer, New York.
- Nekut, A.G., Spies, B.R. 1989. Petroleum exploration using controlled-source electromagnetic methods. *Proceedings of the IEEE*, 77, 338-362. doi: 10.1109/5.18630.
- Nordskog, J.I., Amundsen L. 2007. Asymptotic airwave modeling for marine controlled-source electromagnetic surveying, 72(6), F249-F255.

- Pérez-Flores, M.A., Gómez-Treviño, E. 1997. Dipole-dipole resistivity imaging of the Ahuachapán-Clpilapa Geothermal Field, El Salvador. *Geothermics*, 26, 657-680. doi: 10.1016/S0375-6505(97)00015-1.
- Pérez-Flores, M.A., Méndez-Delgado, S., Gómez-Treviño, E. 2001. Imaging low-frequency and dc electromagnetic fields using a simple linear approximation. *Geophysics*, 66(4), 1067-1081. doi:10.1190/1.1487054.
- Pérez-Flores, M.A., Antonio-Carpio, R.G., Gómez-Treviño, E., Ferguson, I., Méndez-Delgado, S. 2012. Imaging of 3D electromagnetic data at low-induction numbers. *Geophysics*, 77(6), WB47-WB57. doi: 10.1016/S0375-6505(97)00015-1.
- Shewchuk, J.R. 2004. An introduction to the conjugate gradient method without the agonizing pain. Consulted in: <http://www-2.cs.cmu.edu/~jrs/jrspapers.html>.
- Sen, M.K., Stoffa, P.L. 2013. *Global Optimization Methods in Geophysical Inversion*. Cambridge University Press, New York. doi:10.1017/CBO9780511997570.
- Streich, R. 2016. Controlled-Source Electromagnetic Approaches for Hydrocarbon Exploration and Monitoring on Land. *Surveys in Geophysics*, 37, 47-80. doi: 10.1190/1.1487054.
- Ward, S.H., Hohmann, G.W. 1987. Electromagnetic theory for geophysical applications in: Nabighian, M. N. (Ed), *Electromagnetic methods in applied geophysics*. Society of Exploration Geophysics, Oklahoma. pp.131–312.
- Weiss, C.J. 2007. The fallacy of the “shallow-water problem” in marine CSEM exploration. *Geophysics*, 72(6), A93–A97, doi: 10.1190/1.2786868.
- Weiss, C.J., Constable, S. 2006. Mapping thin resistors and hydrocarbons with marine EM methods: Part 2 — Modeling and analysis in 3D. *Geophysics*, 71(6), G321–G332. Doi:10.1190/1.2356908.
- Young, P.D., Cox, C.S. 1981. Electromagnetic active source sounding near the East Pacific Rise. *Geophysical Research Letters*, 8, 1043-1046. doi: 10.1029/GL008i010p01043.
- Yuksel, C., Schaefer, S., Keyser, J. 2011. Parameterization and Applications of Catmull-Rom Curves. *Computer Aided Design*, 43(7), 747-755. doi: 10.1016/j.cad.2010.08.008.

## Appendix A1 Justification of appendix A

---

Most of the time spent in the doctoral research was to develop the theme “Join inversion of controlled source electromagnetic and seismic data applied to hydrocarbon exploration”. During the development of this thesis, many interesting topics related to marine CSEM method were emerging, and due to different circumstances the approach of the thesis changed to the actual subject “Merging land and marine controlled-source electromagnetic methods and a physical model for the elusive airwave”. Therefore, this appendix is a disclosure space for the investigation made in the original title.

Although the original theme was not completely covered the relevant results are described in the appendix as follows: First a code to calculate the electromagnetic fields and their sensitivities for CSEM method is explained, then the displacement-stress formulation of elastic wave equation is solved for the seismic case and their sensitivity kernels are computed. Finally, the objective function is built and a code is developed to solve it in an efficient way.

In the 3D CSEM part, an existing code was modified to increase the precision of the electromagnetic field that it calculates. The results obtained in the numerical simulation were tested with a semi-analytical code, in the same way the sensitivity was proven.

The second part is provides the basic formulation to model the wave displacement field also addressing the boundary conditions and the stability parameter succinctly. The calculation of the sensitivity kernels is not described in detail, but the strategy to compute them is reported.

The last section describes the different elements of the objective function as well as the optimization method used to solve it. This method must solve large-scale problems with low memory requirements. A fast review of the optimization routine and the solutions achieved are examined in the last part of the appendix.

Finally, the idea of this part is not going into detail on each method, but to show the progress made in the topics.

## Appendix A2 3D CSEM forward modeling

---

### A2.1 Approach to the problem

I use the 3D staggered-grid modeling algorithm FDM3D of Weiss and Constable (2006) for the CSEM forward modeling with some modifications. This code solves the Helmholtz equation for electric scattered fields using the finite volume method. The equation solved is written as:

$$\int_{\Gamma} \mathbf{n} \times (\nabla \times \mathbf{E}^s(\mathbf{x})) d\Gamma - i\omega\mu_0 \int_{\Omega} \sigma(\mathbf{x}) \mathbf{E}^s(\mathbf{x}) d\Omega = -i\omega\mu_0 \int_{\Omega} (\sigma(\mathbf{x}) - \sigma_0(\mathbf{x})) \mathbf{E}^p(\mathbf{x}) d\Omega, \quad (21)$$

where superscripts  $p$  and  $s$  denote the primary and secondary fields, respectively,  $\mathbf{x}$  is the position vector,  $\omega$  is the angular frequency,  $\mu_0$  is the vacuum magnetic permeability ( $4\pi \times 10^{-7}$  H/m),  $\sigma$  is the electric conductivity of the medium and  $\sigma_0$  is the conductivity for the primary field. In the finite volume method, the model is divided into continuous control volumes  $\Omega$  that surround each node point where the field was placed on the mesh (e.g. Figure 39). The volume integral represents the electric field into the volume, while the surface integral is interpreted as fluxes of field at the surface  $\Gamma$  of each finite volume, where  $\mathbf{n}$  is the outward-pointing unit normal.

The program uses the Dirichlet boundary conditions for the scattered electric field. The solution of the linear system formed in the equation 21 is given by the quasi-minimal residual method with the coupled two-term recurrence (Freund and Nachtigal, 1994) and the Jacobi preconditioner.

Despite of the efficiency of the code, it presents deficiencies when the field is computed in long offsets hence I did some modifications explained in the next sections.

### A2.2 Primary electric field calculation

Initially the primary electric field could be calculated using a uniform space as background model and a punctual source (Ward and Hohmann, 1988). Now it has the option to use a layered background model, for this option I used the quasi-analytic formula from Chave and Cox (1982) based on Hankel transforms and the filter developed by Kerry Key in 2009 for the approximation of the Bessel functions. It can now add the length of the source in the two cases of background model.

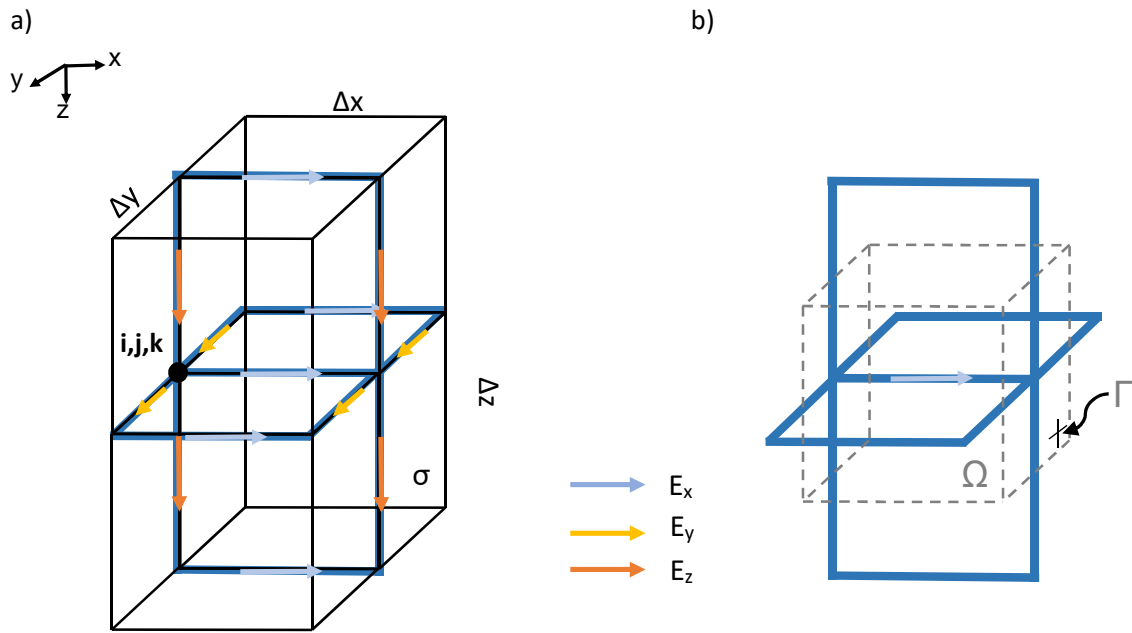


**Figure 39. Staggered grid scheme for the finite volume of scattered electric field formulation.** a) It is a section of the mesh model; the nodes are defined as  $i,j,k$  and the Cartesian position as  $x_i, y_j$  and  $z_k$ , the electric fields are in the midpoints of the edges  $E_x(x_{i+1/2}, y_j, z_k)$ ,  $E_y(x_i, y_{j+1/2}, z_k)$ ,  $E_z(x_i, y_j, z_{k+1/2})$  and the conductivity model in the center of the mesh volume  $\sigma(x_{i+1/2}, y_{j+1/2}, z_{k+1/2})$ . The finite volume stencil for the  $E_x$  field calculation is marked in light navy line. b) Finite volume discretization for the  $E_x$  field, the control volume  $\Omega$  in color gray surround the field with bounding surface  $\Gamma$ . Similar figures was created to calculate the  $y$ -component and  $z$ -component of the scattered electric field.

### A2.3 Averaging formula

As the fields need to be calculated where the conductivity is discontinuous. The original code solves this using arithmetic averages. But I decided to use the harmonic average because it is a better approximation when the magnitude of the conductivity varies by a few orders. For instance, the expression for the average of the staggered conductivity in the  $E_x(i+1/2,j,k)$  field is

$$\sigma^H_{i+\frac{1}{2},j,k} = \frac{\sum_{l=-1}^1 \sum_{m=-1}^1 \Delta y_{j+l} \Delta z_{k+m}}{\sum_{l=-1}^1 \sum_{m=-1}^1 \sigma_{i+\frac{1}{2},j+l+\frac{1}{2},k+m+\frac{1}{2}}} \quad (22)$$

In the same way, the averaging is defined for the  $y$ - and  $z$ -component.

## A2.4 Catmull-Rom spline interpolation

When the linear system is solved, I have to interpolate the fields computed from the staggered grid location to the arbitrary position of the receivers. The original interpolation used is a trilinear interpolation, now it uses the cubic Catmull-Rom splines.

The Catmull-Rom are cubic splines interpolation methods. This is a smooth curve from a set of control points  $P_i$  associated to the parametric value  $s_i$ . This mean that in the parametric value  $s_i$  and  $s_{i+1}$  the curve evaluates to  $P_i$  and  $P_{i+1}$  respectively. Between this consecutive control points,  $P_i$  and  $P_{i+1}$ , the Catmull-Rom curve is composed of 3<sup>rd</sup> degree polynomial segments. These polynomial pieces are only affected by a local set of control points.

I used the Barry and Goldman (1998) formulation which exploited the characteristic of Catmull-Rom spline combining the Lagrange interpolation and the B-spline basis functions. This formula is summarized in a pyramid algorithm (Figure 40b). The pyramid begins with the control points at the base, for the next level (e.g.  $L01$ ). This notation should be interpreted as multiplying each point at the base of the triangle by the coefficient on the arrow and summing the result. From this diagram, it is easy to see that  $C1$  Catmull-Rom curves are cubic polynomials as there are 3 levels in this pyramid and each adds a single, linear factor. The Barry and Goldman's formula is non-uniform and allows to choose the kind of parameterization (arbitrary  $s_i$  values). The behavior of the Catmull-Rom curves depends on the parameterization as shown in Figure 40a. Yuksel et al. (2011) defined the parameter values as

$$s_{l+1} = |P_{l+1} - P_l|^{\zeta} + s_l, \quad (23)$$

where  $0 \leq \zeta \leq 1$  for the knot parametrization,  $l = 0,1,2,3$  with  $s_0 = 0$ , for centripetal Catmull-Rom spline the value of  $\zeta$  is 0.5. When it is 0, the resulting curve is the standard Catmull-Rom spline (uniform Catmull-Rom spline); when  $\zeta = 1$ , the product is a chordal Catmull-Rom spline. Once the interpolation is made in one dimension this is extended to three dimensions.

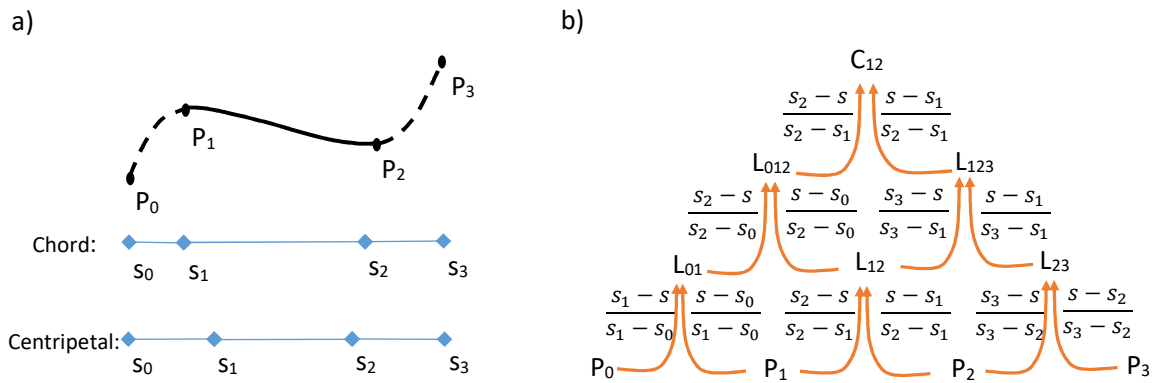


**Figure 40. Centripetal Catmull-Rom.** a) Comparative of the different kind of parameterization for Catmull-Rom Spline. b) Pyramid of Barry and Goldman (1998) for cubic Catmull-Rom Spline.

## A2.5 The finite difference approximation

In the first integral of the left side of equation 21 is necessary calculate the rotational of the electric field. The original code use the standard finite difference approximation, based on truncated Taylor's series expansions to calculate the first derivatives. We adapt an exponential finite difference scheme. This approximation was described by Ixaru and Berghe (2004) and exploited in the CSEM method by Jaysaval et al. (2015) because of the EM fields have oscillatory and exponentially decaying behaviors.

$$f'(x) = \lim_{h \rightarrow 0} \frac{c_1 f\left(x + \frac{h}{2}\right) + c_2 f\left(x - \frac{h}{2}\right)}{h} \quad (24)$$

In the standard finite difference the weight coefficients in the equation 24 are  $c_1 = -c_2 = 1$ . This is a good approximation only if the field behaviors between the nodal points is a low-degree polynomial. In the exponential finite difference, the weight coefficients  $c_1$  and  $c_2$  can be chosen in accordance with the characteristics of the electromagnetic waves in components that represent in a better way the behavior of the field.

$$c_1 = -c_2 = \frac{1}{vh} \left[ \exp\left(-v + \frac{h}{2}\right) + \exp\left(v + \frac{h}{2}\right) \right] \quad (25)$$

$$v = \pm(1-i) \sqrt{\omega \mu_0 \frac{\sigma}{2}}$$

As it can be seen in the previous equation, the electromagnetic behavior is included in the exponent coefficient  $\nu$  which is chosen as the wave number of the planar EM fields to include the frequency and the conductivity model in the derivative calculus. From the point of view of the linear system, the difference between the standard and exponential finite difference methods is that in the first one only the diagonal of the matrix is complex, while in the exponential finite difference the diagonal and the off-diagonal values are complex.

## **A2.6 Results of 3D CSEM forward modeling**

The modified code is tested with a background model (Figure 1a) and compared with the semi-analytical code of Key (2009) in Figure 41. The mesh is a uniform 160 X 160 X 160 node with a length of 4,000 m in all directions. The x- and y-direction start in -3,000m and finish in 3,000 m while the z-direction start in -1,000 m and finish in 3,000 m. The water depth is 1km. The source is punctual, collocated 50 m from the seafloor and in the middle of the model, with a frequency of 1 Hz. The receivers lay over the seafloor collocated in inline direction.

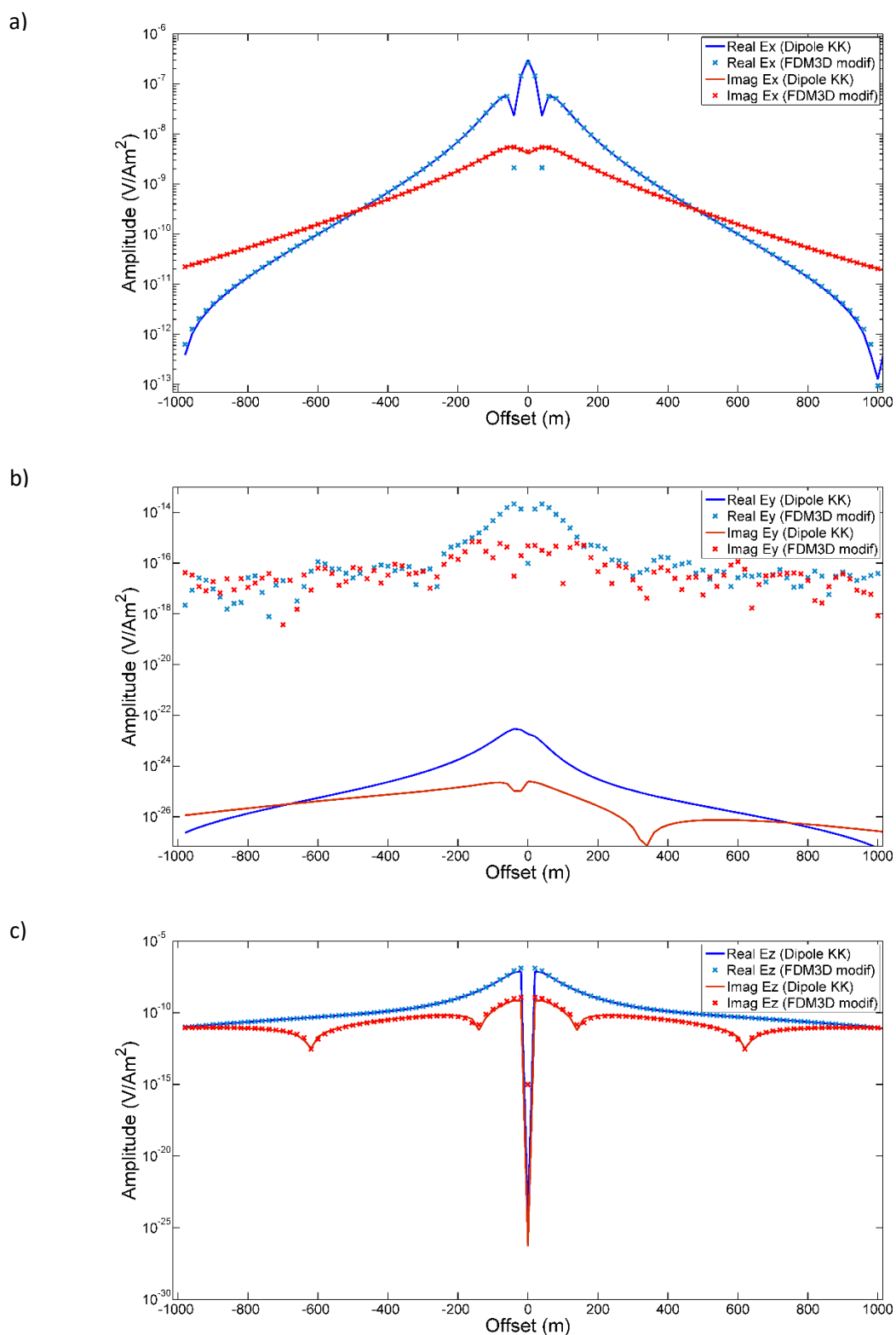


**Figure 41. 3D CSEM forward modeling.** Comparison of the electric fields calculated with the three dimensional forward model (crosses) and the semi-analytical code DIPOLE1D developed by Key in 2009 (solid lines). a) Ex. b) Ey. c) Ez. The worst similarity is in Ey field because in inline direction this field is too small and the differences between the crosses and the solid lines is due to the computational errors.

## Appendix A3 Sensitivity in the CSEM data

---

To compute the sensitivity at the CSEM data, I use the adjoint-equation approach because it is efficient in these cases when the number of data is less than the number of unknown parameters. I followed the development of McGillivray et al. (1994) by its simplicity, though does not formally invoke reciprocity. Their calculus begin by solving a primal electromagnetic problem subject to boundary conditions, until a problem with sensitivity equations and boundary conditions is set. To solve it, they appeal to reciprocity of the electromagnetic data using an auxiliary Maxwell equations with the particularity that the auxiliary problem is solved using an electric (or magnetic) dipole inside the numerical domain. Using vector identities, divergence theorem and proving that both the auxiliary and the sensitivity fields are eliminated when the boundary extends to the infinity, the sensitivity equation for the electric field can written as:

$$\int_D \frac{\partial \mathbf{E}}{\partial \sigma_k} dv = \int_D \tilde{\mathbf{E}} \cdot \mathbf{E} \Psi_k(\mathbf{x}) dv. \quad (26)$$

In this case, the basis functions  $\Psi_k(\mathbf{x})$  are continuous over the discretized conductivity  $\sigma_k$ . The previous equation shows that the sensitivity for the electric field is obtained specifying the source for the supplementary fields and by integrating the dot product of the primal ( $\mathbf{E}$ ) and auxiliary ( $\tilde{\mathbf{E}}$ ) electric field over the non-zero region of  $\Psi_k(\mathbf{x})$ . For example, to compute the sensitivity of  $E_x$  electric field. In the left hand of the Equation 26, the primal problem is solved in all the computational domain, meanwhile the auxiliary problem use a unit horizontal electric dipole in x-direction placed at the observation position to solve the auxiliary fields in all the domain. Finally, with the two electric fields obtained over the conductivity domain, the dot product of this two fields is integrated.

Figure 42 displays the real part of the sensitivity for the electric field in x-direction ( $E_x$ ). The test uses the same background model than the experiments in the forward modeling. The curve of the computed Fréchet derivative is the sensitivity of the whole model below the seafloor. Unfortunately, when the calculations of the code are compared with a semi-analytical method (Key, 2009) the results are not consistent. The reason of this, is that the precision of the adjoint approach lies on the precision of the primal and auxiliary fields. As it can be seen in Figure 41, the forward modelling has not enough precision and the errors are added when the sensitivity of each volume is summed to obtain the sensitivity of the sub-seafloor.

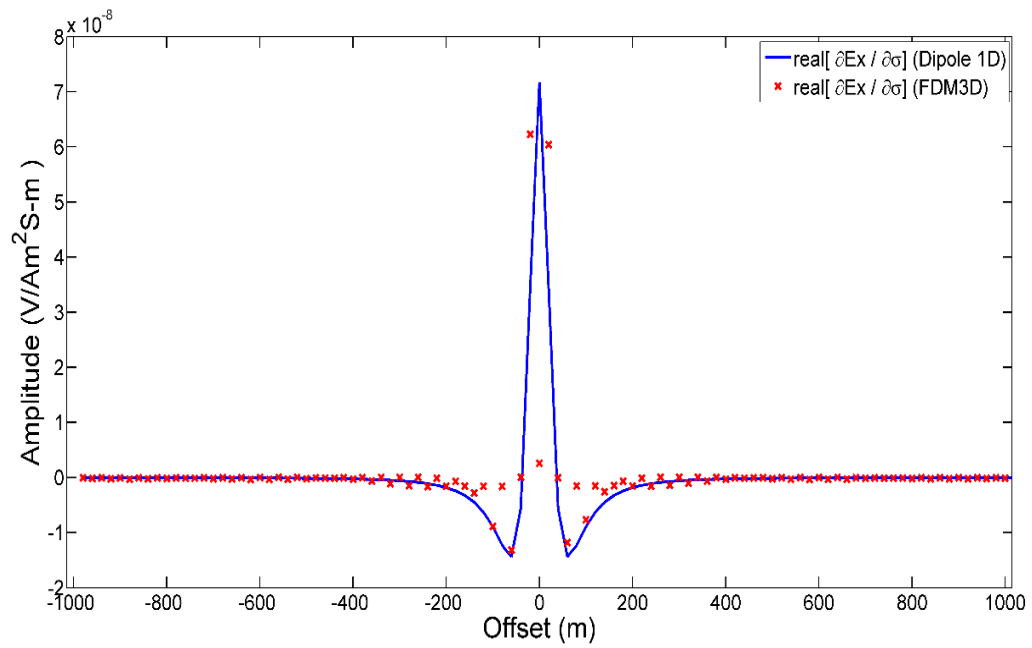


**Figure 42. Sensitivity 3D CSEM.** Graphical comparison of the Ex electric field sensitivity. The blue line is the sensitivity calculated by the DIPOLE1D code developed by Key in 2009. The red cross is the sensitivity calculated using the adjoint formulation for the tridimensional model.

## Appendix A4 3D Seismic forward modeling

### A4.1 Approach to the problem

To model the seismic response, I start from the equation of motion

$$\rho(\mathbf{x}) \partial_{tt} u_p(\mathbf{x}, t) = \partial_p \tau_{pq}(\mathbf{x}, t) + f_p(\mathbf{x}, t); \quad (27)$$

and the Hooke's law for an elastic, inhomogeneous and isotropic media.

$$\tau_{pq}(\mathbf{x}, t) = \delta_{pq} \lambda(\mathbf{x}) \partial_r u_r(\mathbf{x}, t) + \mu(\mathbf{x}) [\partial_p u_q(\mathbf{x}, t) + \partial_q u_p(\mathbf{x}, t)], \quad (28)$$

where  $p, q, r \in \{x, y, z\}$ ,  $\mathbf{x}$  is the position vector in spatial coordinates,  $t$  is the time variable,  $\delta$  is the Kronecker delta,  $\rho$  is the density,  $\lambda$  and  $\mu$  are the Lamé elastic coefficients. The displacement vector is defined as  $\mathbf{U}(u_x, u_y, u_z)$ , the stress tensor as  $\tau_{p,q}$ ; and the body force per unit volume as  $\mathbf{f}(f_x, f_y, f_z)$ . The scheme to solve these equations is shown in Figure 43, using a wavelet formulation as the source term.

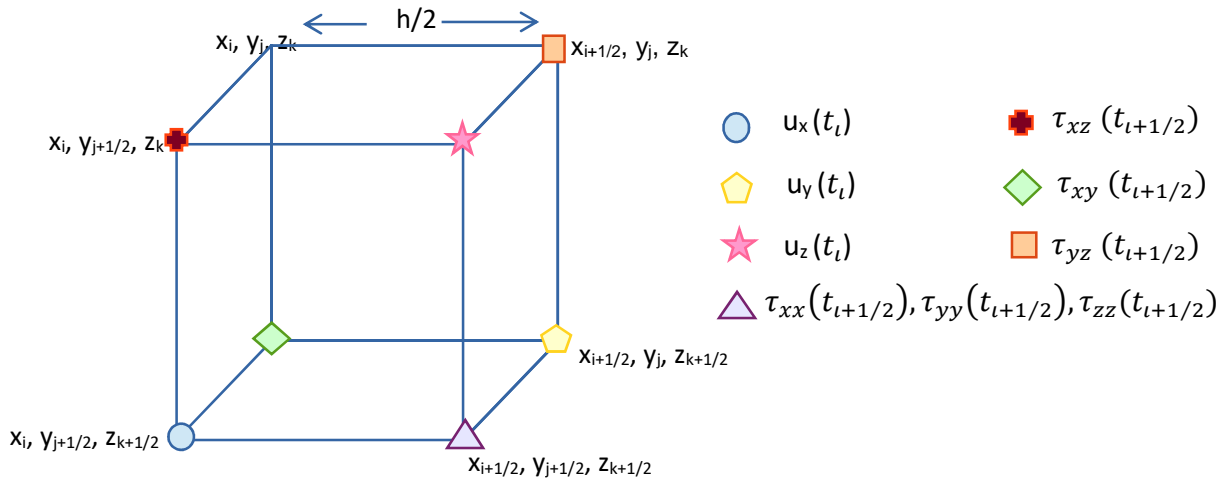


**Figure 43. Staggered-grid scheme for displacement-stress formulation.** Spatial grid cell for the staggered-grid finite difference scheme; the nodes are defined as  $i, j, k$  and the cartesian position as  $x_i, y_j$  and  $z_k$ , the displacement are in the midpoints of the edges  $u_x(x_i, y_{j+1/2}, z_{k+1/2})$ ,  $u_y(x_{i+1/2}, y_j, z_{k+1/2})$ ,  $u_z(x_{i+1/2}, y_{j+1/2}, z_k)$  and the model properties in the nodes  $\rho(i, j, k)$ ,  $\mu(i, j, k)$  and  $\lambda(i, j, k)$ . The displacement are defined in complete time steps meanwhile the stress are in half time steps.

Unlike other formulations, the displacement-stress formulation needs storing a previous time for the displacement but not in the stress variables; this was exploited in the code to reduce the storage requirements.

## A4.2 The finite difference approximation

To calculate the directional derivative, I use the 4<sup>th</sup>-order approximation developed in the staggered-grid finite difference scheme by Moczo et al. (2000). For example, the first derivative of a function  $\Phi(x_0)$  is approximated by

$$\frac{d\Phi}{dx}(x_0) = \frac{1}{h} \left\{ a \left[ \Phi \left( x_0 + \frac{3}{2}h \right) - \Phi \left( x_0 - \frac{3}{2}h \right) \right] + b \left[ \Phi \left( x_0 + \frac{1}{2}h \right) - \Phi \left( x_0 - \frac{1}{2}h \right) \right] \right\}, \quad (29)$$

with  $a=-1/24$  and  $b = 9/8$ .

## A4.3 Stability parameter

As it can be seen, the displacement equation (Equation 27) is explicit in time, so the new step in time is calculated with the previous step in time. Therefore the size of the time step  $\Delta t$  cannot be propagated across the mesh faster than the mesh velocity (Bording and Lines, 1997). To maintain the stability of this scheme Moczo et al. (2000) calculates the maximum time step size defined as

$$\Delta t \leq \frac{6}{7\sqrt{3}} \frac{h}{v_p}, \quad (30)$$

Where  $h$  is the maximum directional step,  $v_p$  is p-wave velocity obtained with the relation of the Lamé parameters and density. Finally the stability parameter  $p$  is defined as:  $\frac{7\sqrt{3}}{6} \frac{\Delta t}{h} v_p$ , which means that  $p \leq 1$ .

#### A4.4 Averaging formula

As it is noted in Figure 43, the displacements and stresses have to be computed where the media properties are discontinuous. To average the media properties in the position of the fields, I use the volume harmonic and arithmetic averaging for the elastic moduli and densities as Graves et al. (1996) and Moczo (2002). For example, Equation 31 is the density average for the  $u_x$  displacement and Equation 32 is the shear modulus average  $\tau_{xx}$ :

$$\rho_{i,j+\frac{1}{2},k+\frac{1}{2}}^A = \frac{1}{h^3} \int_{x_{i-1/2}}^{x_{i+1/2}} \int_{y_j}^{y_{j+1}} \int_{z_k}^{z_{k+1}} \rho \, dx \, dy \, dz, \quad (31)$$

$$\mu_{i+1/2,j+\frac{1}{2},k+\frac{1}{2}}^H = \frac{1}{h^3} \int_{x_i}^{x_{i+1}} \int_{y_j}^{y_{j+1}} \int_{z_k}^{z_{k+1}} \frac{1}{\mu} \, dx \, dy \, dz. \quad (32)$$

#### A4.5 Boundary conditions

This section describes what happens when the propagated wave arrives to the boundaries of the computational model. The boundary on the top of the computational model is a free surface, it is modeled using a planar free surface with the normal strain equal to zero. For this, I use the adjusted finite difference approximations (AFDA) of Kristek et al. (2002). In this method the values are calculated using adjusted finite differences approximations to the boundary conditions components in  $h$  and  $h/2$  to maintain the precision of the algorithm.

In the remaining borders of the computational model, sides and bottom have to be treated as a transmissive boundaries like a large and continuous model, because the area to be modeled might be quite large compared with the area of the computational model.

To model the effect of this non-reflecting boundary, I use the hybrid scheme for absorbing boundary conditions of Liu and Sen (2010). This method is a mixture between the absorbing boundary (non-reflecting boundary) conditions and the damping zone method. The main idea of this scheme is to

make a computational domain where the outgoing waves are damped until they are eliminated in the boundary with a short and effective damping area.

The total computed domain is divided into an inner area, a damping area (or transition zone), and a boundary (Figure 44). The inner area, is where the elastic equation is modeled; in the damped area the elastic equation and the absorbing boundary condition are needed and, in the boundary, only the absorbing boundary condition is computed. The last two zones are computed using the following equation:

$$\mathbf{U}(\mathbf{x}_l, t) = (1 - w_l)\mathbf{U}^{EWE}(\mathbf{x}_l, t) + w_l\mathbf{U}^{ABC}(\mathbf{x}_l, t). \quad (33)$$

Equation 33 shows how the wave field  $\mathbf{U}(\mathbf{x}_l, t)$  passes through the hybrid boundary area. The variables  $\mathbf{U}^{EWE}$  and  $\mathbf{U}^{ABC}$  are the displacement fields of the elastic wave equation (Equation 27) and the chosen absorbing boundary condition, respectively.  $w_l$  is a weighting vector, its values decrease from 1 to 0 and its length depends on the length of the hybrid boundary zone. The outgoing displacement  $\mathbf{U}^{EWE}$  is damped by the absorbing boundary condition  $\mathbf{U}^{ABC}$  using the weighting vector until it eliminates any outgoing wave field in the edge by the absorbing boundary condition.

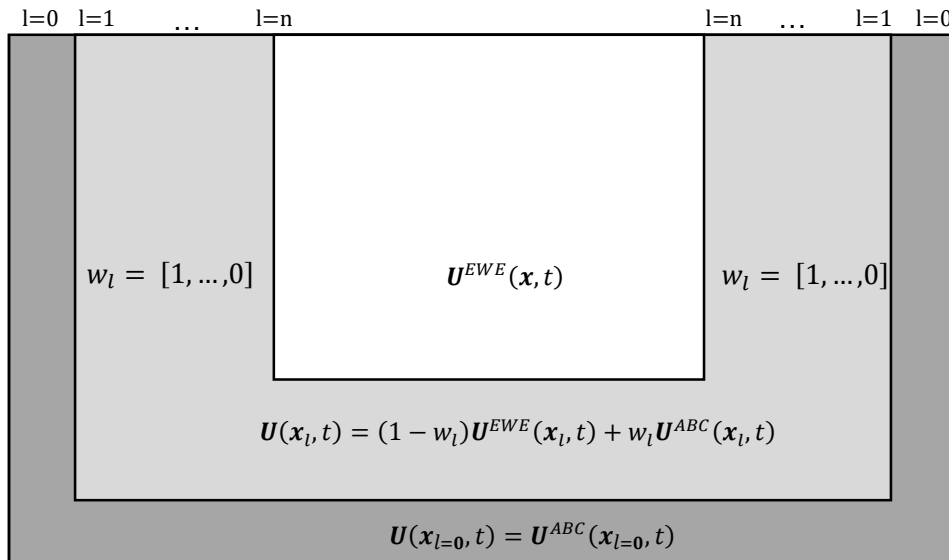


**Figure 44. Hybrid boundary condition scheme.** The gray colors represent the hybrid boundary zone and the white region is the original computational domain. The figure is not to scale, since the computational domain is larger than the hybrid boundary area. The subscript  $l$  in vector position means the node in the absorbing direction, e.g. for the left border  $u_x(x_i, y_{j+1/2}, z_{k+1/2})$ ,  $u_y(x_{i+1/2}, y_j, z_{k+1/2})$  and  $u_z(x_{i+1/2}, y_{j+1/2}, z_k)$ .

The absorbing boundary condition selected to apply on the hybrid boundary is the second order one-way wave equations (OWWEs) developed by Higdon in 1991 for the elastic case. This technique offers one of the best accuracies and stabilities. To apply the Higdon boundary condition a second order boundary operator is applied to each component of displacement.

For example, in the left boundary, the operator that was applied is:

$$\left( B_1 \frac{\partial}{\partial t} - v_p \frac{\partial}{\partial x} \right) \left( B_2 \frac{\partial}{\partial t} - v_p \frac{\partial}{\partial x} \right) u_p = 0 \quad (34)$$

where the subscript  $p$  means the direction of the displacement,  $B_1=1$ ,  $B_2 = v_p/v_s$ ,  $v_p$  and  $v_s$  are  $P$ - and  $S$ -wave velocities respectively. The minus sign means the direction of the propagation of the boundary operator. The discrete form of the previous equation can be written as

$$u_p(0, y_j, z_k, t_{i+1}) = \sum_{n=1}^2 \gamma_{0,n} u_p(x_i, y_j, z_k, t_i) + \sum_{m=0}^1 \sum_{n=0}^2 \gamma_{m+1,n} u_p(x_i, y_j, z_k, t_{i-1}), \quad (35)$$

the subscript  $i,j,k$  denotes the node position for the  $x$ -,  $y$ - and  $z$ -direction respectively, while the subscript  $i$  is the step time. For more details of how calculate the weights  $\gamma$  see Higdon 1991.

Finally, to maintain the stability of the boundary conditions, I tried to avoid the convergence of boundary zones but in the zone where the coincidence was inevitable, half of each boundary is used; in similar way when three boundaries coexist, a third part of each boundary is considered.

## A4.6 Catmull-Rom spline interpolation

To calculate the displacement in any position where the receivers were collocated I use the Catmull-Rom interpolation equally spaced, this method is similar to cubic spline method.

## A4.7 Results of seismic forward modeling

To test the forward seismic model, I use a 3D homogeneous model with a uniform mesh of 100 nodes and a length of 1000m in all directions. The homogenous half space is modeled with a compressional-wave speed of 2,700 m/s, shear-wave speed of 1,400 m/s and density of 1,200 kg/m<sup>3</sup>. For the hypothetical source, I use a point force in x-direction with a Ricker wavelet source time function with a peak frequency of 15 Hz located at the middle of the model. The results of this model is exposed in seismograms in Figure 45 and different time slices for the displacement in Figure 46. The observed reflections in Figure 46 are from the top boundary due to the free surface border because in the other edges the propagated wave is absorbed.

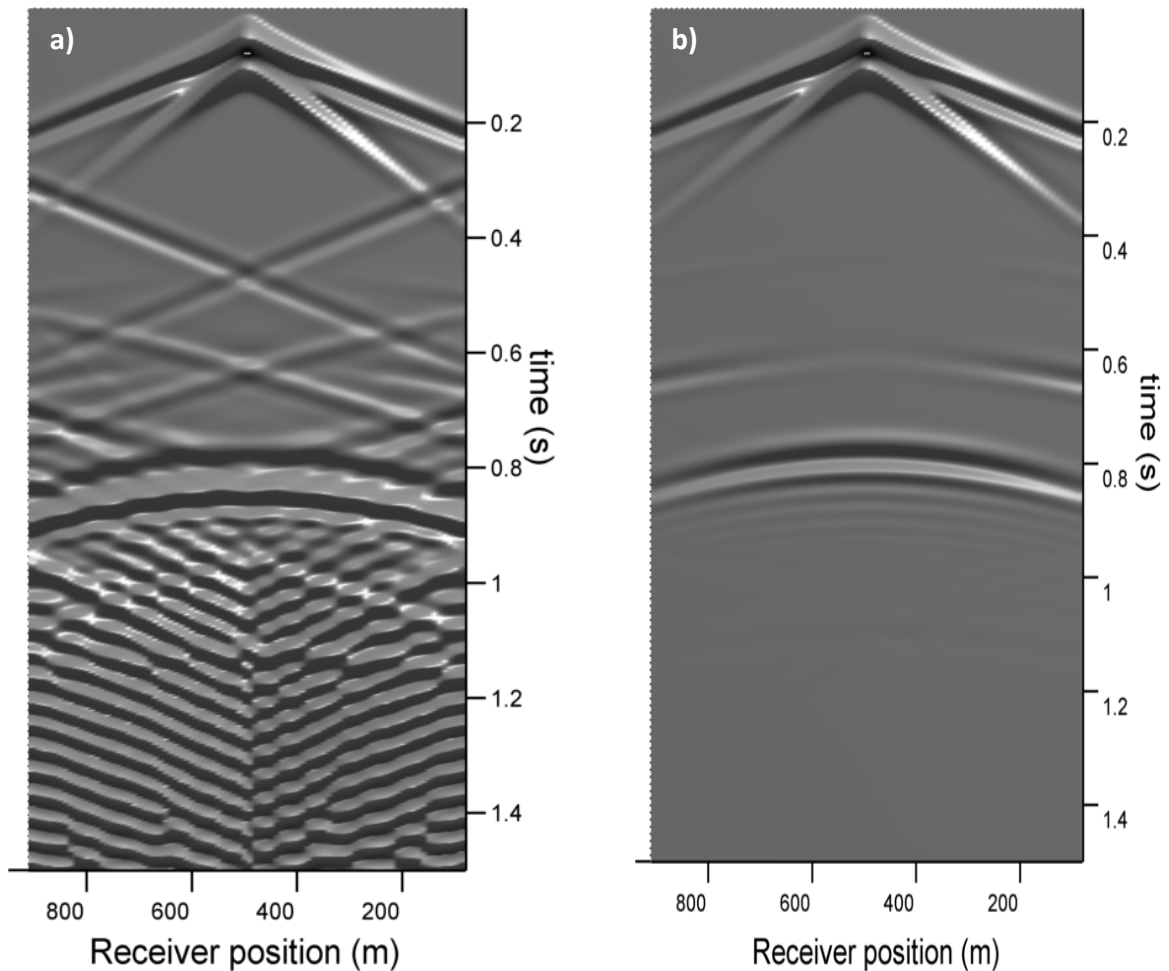


**Figure 45. U<sub>x</sub> seismograms.** Seismogram of the  $u_x$  displacement. a) Model without hybrid boundary conditions. b) Model with hybrid boundary conditions. It is notorious the effect of the spurious reflections and the need of using non-reflecting boundaries.

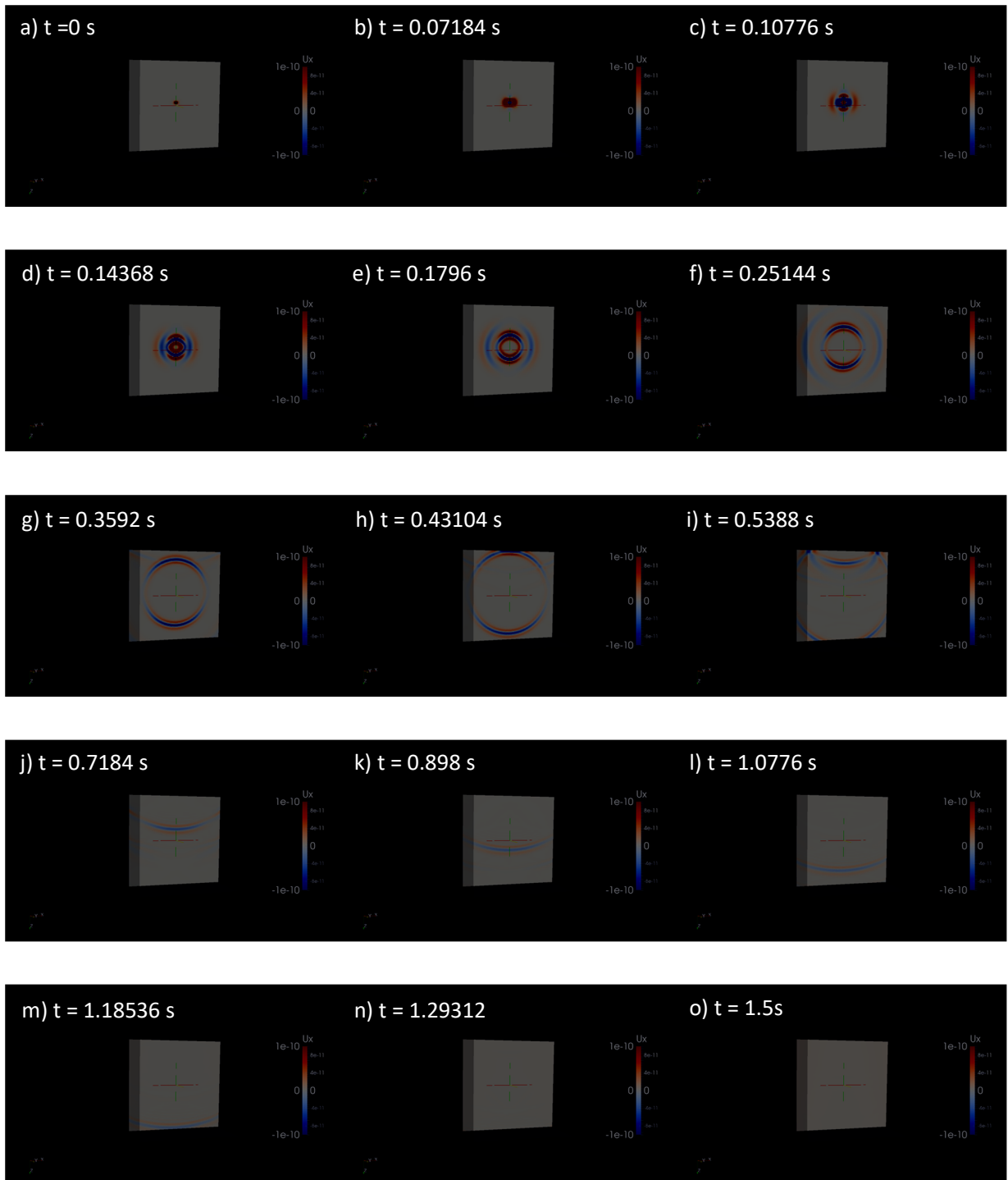


**Figure 46. Forward modeling with boundary conditions.** Different time slices for the  $u_x$  displacement. The source is a wavelet function in the  $x$ -direction. The model is a homogenous half space with  $v_p=1700\text{m/s}$ ,  $v_s=1400\text{m/s}$  and  $\rho=1200 \text{ kg/m}^3$ , the top has a free surface and the remaining borders hybrid boundary conditions. The wave propagation shows reflections only in the top of the model.

## Appendix A5 Seismic sensitivity kernels

---

As previously stated, the methodology used to obtain the sensitivity is the adjoint method. In the time domain, the adjoint approach was originated in the field of control theory for dynamical systems. It is an efficient tool for the computation of an objective functional with respect to the model parameters due to its dependency on just two numerical simulations to each source, one for the model and one for the adjoint calculation.

Starting from the objective function  $\varphi(m)$ , its Fréchet derivative may be written in generic form as  $\delta\varphi = \int K_m(x) \delta \ln m(x) d^3x$ , where  $m$  denotes the physical parameters of the earth model,  $\delta \ln m = \delta m/m$  the relative model perturbation and  $K_m$  the associated 3D sensitivity or Fréchet Kernel.

The kernels showed in Liu and Tromp (2006) are based on the the adjoint method using the Lagrange multipliers and were derived from the elastic and isotropic wave equation. They define explicitly two sets of kernels one for the density, shear moduli and bulk moduli; and other for density, compressional-wave velocity and shear-wave velocity. To complete the set of kernels, I add the kernels for density, shear moduli and first Lamé parameter.

The isotropic kernels for density ( $\rho$ ), shear moduli ( $\mu$ ) and bulk moduli ( $\kappa$ ) are defined as

$$K_\rho(x) = - \int_0^T \tilde{\mathbf{U}}(\mathbf{x}, T-t) \cdot \partial_t^2 \mathbf{U}(\mathbf{x}, t) dt, \quad (36)$$

$$K_\mu(x) = - \int_0^T 2\mu(x) \tilde{\mathbf{D}}(\mathbf{x}, T-t) : \mathbf{D}(\mathbf{x}, t) dt, \quad (37)$$

$$K_\kappa(x) = - \int_0^T \kappa(x) [\nabla \cdot \tilde{\mathbf{U}}(\mathbf{x}, T-t)] [\nabla \cdot \mathbf{U}(\mathbf{x}, t)] dt, \quad (38)$$

Where

$$\begin{aligned} \mathbf{D} &= \frac{1}{2} [\nabla \mathbf{U} + (\nabla \mathbf{U})^t] - \frac{1}{3} (\nabla \cdot \mathbf{U}) \mathbf{I}, \\ \tilde{\mathbf{D}} &= \frac{1}{2} [\nabla \tilde{\mathbf{U}} + (\nabla \tilde{\mathbf{U}})^t] - \frac{1}{3} (\nabla \cdot \tilde{\mathbf{U}}) \mathbf{I}. \end{aligned} \quad (39)$$

The set of kernels for density ( $\rho$ ), compressional-wave speed ( $v_p$ ) and shear-wave speed ( $v_s$ ) are

$$K'_\rho = K_\rho + K_\kappa + K_\mu , \quad (40)$$

$$K_{v_s} = 2 \left( K_\mu - \frac{4}{3} \frac{\mu}{\kappa} K_\kappa \right), \quad (41)$$

$$K_{v_p} = 2 \left( \frac{\kappa + \frac{4}{3} \mu}{\kappa} \right) K_\kappa. \quad (42)$$

Finally, for density ( $\rho$ ), shear moduli ( $\mu$ ) and first Lamé parameter ( $\lambda$ ) the kernels are

$$K_\rho(x) = - \int_0^T \tilde{\mathbf{U}}(\mathbf{x}, T-t) \cdot \partial_t^2 \mathbf{U}(\mathbf{x}, t) dt, \quad (43)$$

$$K_\lambda(x) = - \int_0^T \lambda(x) [\nabla \cdot \tilde{\mathbf{U}}(\mathbf{x}, T-t)] [\nabla \cdot \mathbf{U}(\mathbf{x}, t)] dt, \quad (44)$$

$$K_\mu(x) = - \int_0^T \mu(x) \left[ \nabla \mathbf{U}(\mathbf{x}, t) + (\nabla \mathbf{U}(\mathbf{x}, t))^t \right] : \left[ \nabla \tilde{\mathbf{U}}(\mathbf{x}, T-t) + (\nabla \tilde{\mathbf{U}}(\mathbf{x}, T-t))^t \right] dt. \quad (45)$$

$\tilde{\mathbf{U}}(\tilde{u}_x, \tilde{u}_y, \tilde{u}_z)$  is the adjoint displacement vector calculated using as source the time reverse differences between the synthetics displacements and the data at the receivers positions. The adjoint source is activated in the same time in all receiver positions.

The time integration in the previous equations is defined from the initial time  $0$  to the last time  $T$ . To calculate the time integration, one needs to have access to the forward wave  $\mathbf{U}$  at the time  $t$  and the adjoint wave field  $\tilde{\mathbf{U}}$  at the time  $T-t$ , one solution is to save the whole forward model in space and time, and then the adjoint displacement is computed. While performing the time integration that has access to the time  $t$  of the adjoint formulation, the forward modeling stored corresponding to time  $T-t$  can read it. Other solution to reduce the storage requirements is to reconstruct the forward wave field backwards in time from the displacement wave field at the end of the simulation. This can be done if the model is free

from of attenuation. In the case of the absorbing boundary zone, the effect is restored saving the border of the model before the attenuated zone (Figure 44), which requires less storage.

To model the sensitivity kernels, I decided to reconstruct the forward wave field using the backward modeling. Therefore, I save the wave field variables before they arrive at the hybrid boundary zone, this is done in each time step. When the forward modeling ends, the backward modeling starts with the wave field of the last simulation and continues reinjecting the wave field saved in its corresponding time step. The reconstruction of the forward wave field is verified in Figure 47. The model used is the same as that used for the forward modeling test (Figure 45).

Now, the adjoint model is performed using the same scheme of the forward modeling with the difference that the source is collocated at the receiver position and calculated with the differences between the synthetic displacement and the data. To model the adjoint simulation, I am using just one receiver situated 100m from the source in the x-direction, with the P-phase obtained in the synthetic fields as source because for this experiment the data is zero.

Therefore, with the displacement and adjoint fields in memory, one can directly calculate the sensitivity kernels. I use the expressions (40), (41), and (42) for the corresponding kernels. In Figure 50 the kernels are plotted. Despite the kernels have to be tested in more detail and check the results, the characteristic 'banana-doughnut' shape of this kernels can be observed in Figure 48 and can be compared with those calculated by Liu and Tromp in 2006 . Notice that the kernel has a negative sensitivity, this indicate that a positivity anomaly causes advances in the travel time. Other characteristic of this kernels is that the highest sensitivity occurs in the zone where the fields interact.

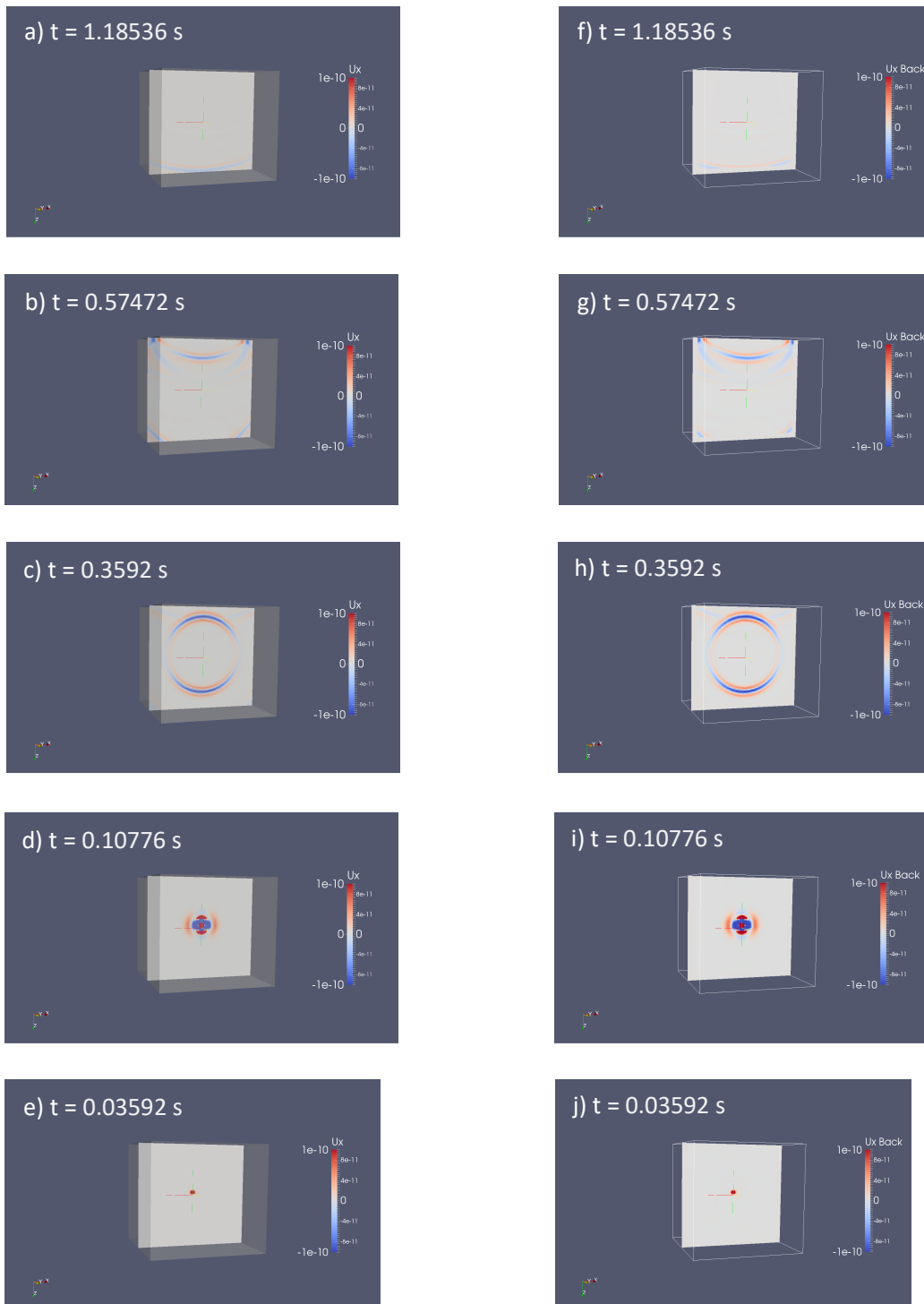


**Figure 47. Backward modeling.** Comparison of the  $u_x$  displacement for the forward modeling (a,b,c,d,e) and the backward modeling (f,g,h,i,j) in the most representative time steps. It is clear, how the wave field and its reflections are recovered.

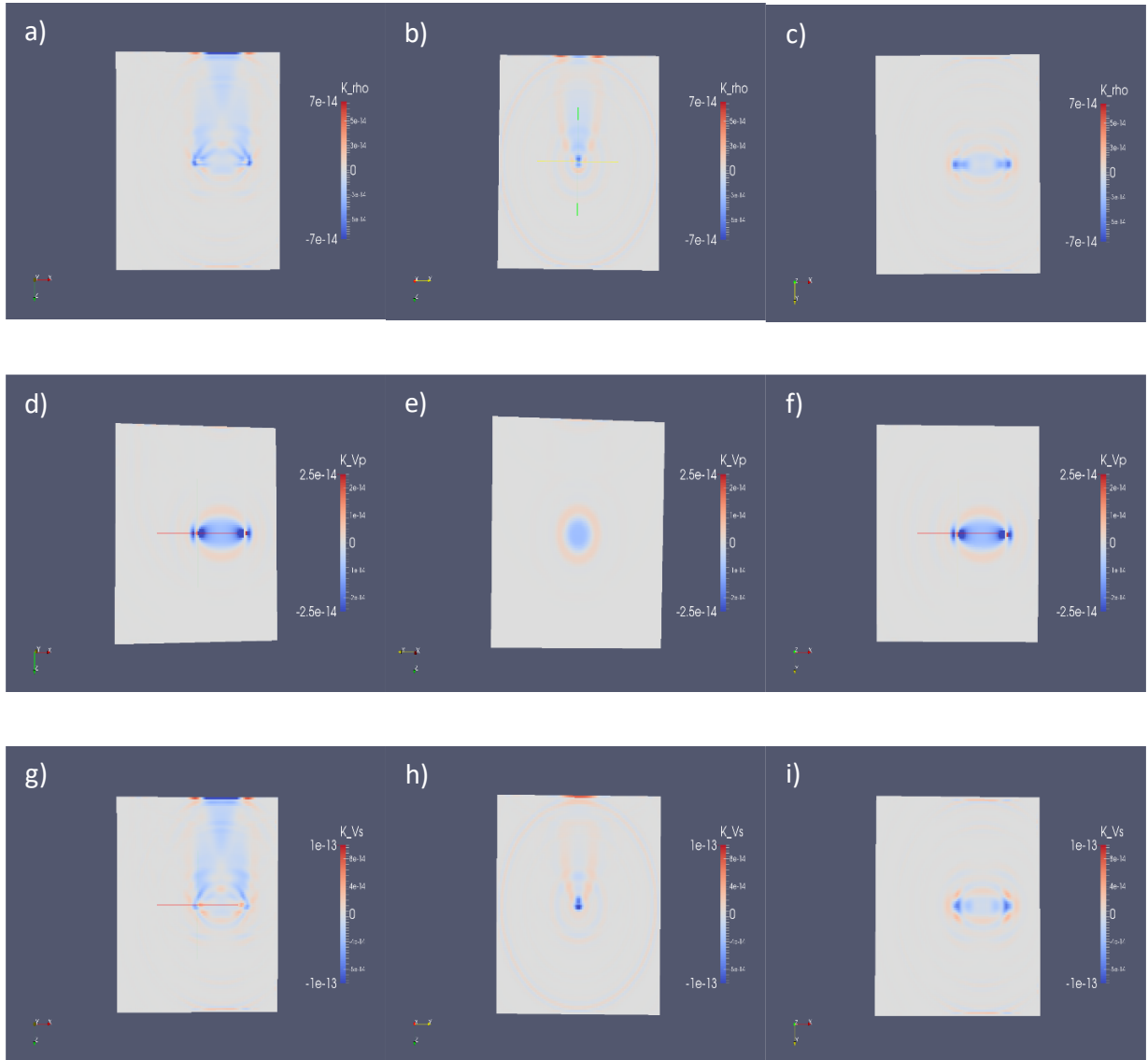


**Figure 48. P-sensitivity kernels.** a) P-sensitivity kernel  $K_\rho$  x-z plane. b) P-sensitivity kernel  $K_\rho$  y-z plane. c) P-sensitivity kernel  $K_\rho$  x-y plane. d) P-sensitivity kernel  $K_{Vp}$  x-z plane. e) P-sensitivity kernel  $K_{Vp}$  y-z plane. f) P-sensitivity kernel  $K_{Vp}$  x-y plane. g) P-sensitivity kernel  $K_{Vs}$  to the x-z plane. h) P-sensitivity kernel  $K_{Vs}$  y-z plane. i) P-sensitivity kernel  $K_{Vs}$  x-y plane.

## Appendix A6 Inverse problem statement

---

### A6.1 Objective function

The objective function to be optimized is divided in four different parts,

$$\varphi = \varphi_{data} + \varphi_{damp} + \varphi_{smooth} + \varphi_{joint}. \quad (46)$$

The first part is the data of the two geophysical methods. For example, the displacement fields  $\mathbf{U}$  are the data for the seismic method and the electric fields  $\mathbf{E}$  for CSEM data. The second term is the jumping function, this function works as a regularization term and controls how far the previous models are from the next models. The third term is the smoothness function, it also works as a regularization term that gives smoothness to the models. Finally, the fourth term is the conjunction function to share the information among the models.

Each part of the objective function is explained in detail as follows:

$$\varphi_{data} = \|\mathbf{d}_i - \mathbf{f}_i(m_j)\|_{C_{d_i}^{-1}}^2, \quad (47)$$

is the geophysical data part, where  $\mathbf{d}_i$  are the data vectors,  $m_j$  are the models to each functional  $\mathbf{f}_i$  and  $C_d$  is the *a priori* data covariance matrix; the subscript  $i$  is to each geophysical method and the subscript  $j$  is to each model. The CSEM functional is defined as  $f_{CSEM}(m_\sigma) = \mathbf{E}(E_x, E_y, E_z)$  and its physical property to be modeled is the conductivity ( $\sigma$ ). While the functional in seismic is defined as  $f_{seis}(m_1, m_2, m_3) = \mathbf{U}(u, v, w)$ ; and the subscript 1, 2, and 3 are the set of elastic properties in the seismic model ( $\rho, \lambda, \mu; \rho, \kappa, \mu$ ; or  $\rho, v_p, v_s$ ).

The smoothness term is given

$$\varphi_{damp} = \alpha_j \left\| m_j^p - m_j \right\|_{C_{m_j}^{-1}}^2, \quad (48)$$

this is the jumping function and says how close the next model is from the previous model, the superscript  $p$  means the previous  $j$  model,  $\alpha$  is the damping parameter, and  $C_m^{-1}$  is the *a priori* model covariance matrix. Subsequently I use this term to test the solver.

The joint term is given by:

$$\varphi_{smooth} = \beta_j \|D m_j\|_{C_{D_j}^{-1}}^2, \quad (49)$$

in this smoothness term, the variable  $D$  is the smoothness operator of first or second derivative.  $\beta$  is the smoothing parameter and  $C_{D_j}^{-1}$  is the derivative covariance matrix of the  $j$ -th model.

$$\varphi_{joint} = \gamma_{jk} \|\tau(m_j, m_k)\|_{C_{\gamma_{jk}}^{-1}}^2, \quad (50)$$

where  $\tau(m_j, m_k) = \nabla m_j \times \nabla m_k$ ,

the  $\varphi_{joint}$  refers to conjunction term to join the models features. I use the cross gradient function  $\tau$  developed by Gallardo and Meju in 2004,  $\gamma$  is the conjunction parameter and  $C_{\gamma}^{-1}$  is the join covariance matrix for the  $j$ -th and  $k$ -th model.

## A6.2 Seafloor topography

In the optimization method a function that depends of the seafloor topography is included in order for the objective function to only take into account the model parameters below the seafloor topography (Figure 49).

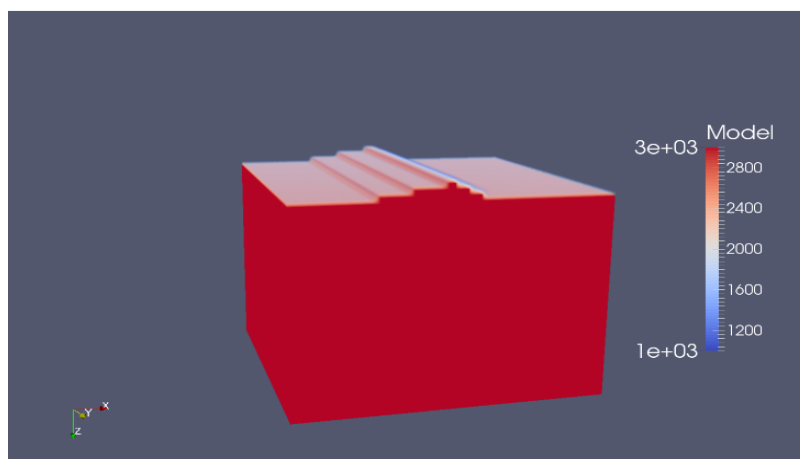


**Figure 49. Topography model.** This is the topography included in the next examples, the values of the models over this topography have been chosen to simulate the sea. The objective function only takes the values below the seafloor because the sea is always constant.

### A6.3 Objective function solver

Once the objective function is defined a numerical optimization method must be selected to obtain an optimal value. The solution of an optimization problem is a set of allowed values of the model parameters for which the objective or the misfit function assumes an optimal value (Gill et al., 1981) in our case the minimal value. Several methods exist to search the minima of the objective function, one idea is going from local minimum until the global minima of the function is reached. These methods are called local optimization methods (Sen and Stoffa, 2013). The most popular local optimization methods based in gradients are the steepest descent method, the Newton's method and the conjugate gradient method (CG). The process in these methods is the same, first a search direction is calculated, then compute the step length on this direction and update the model value with the new direction and step length, if the new model achieves the convergence, it stop, if not all the process is repeated until reach the defined convergence.

To choose the most appropriate method, it is necessary examining the techniques above mentioned. From the point of computational cost, the steepest descent method is the cheapest method, followed by the conjugate gradient method and in the bottom the Newton's method because it needs to calculate the Hessian of the objective function, making it the most costly of the three of them. Other point to analyze is the convergence of the method, to increase it, the search direction must be optimized, and although the search direction of the two first methods have the same philosophy of using the residual of the objective function, the CG method adds the conjugacy of the residuals improving the convergence of the steepest descent method (Shewchuk, 1994).

Taking the previous arguments and the objective function previously defined, I decided to use the nonlinear conjugate gradient method, which is a generalization of the conjugate gradient method to nonlinear functions. Whereas the linear CG seeks a direct solution of the linear equation, the nonlinear CG finds local minimums along of the search direction using the gradient of the objective function; it is a good approximation when the function is quadratic (or approximately) near the minimum. Another change for the nonlinear schemes is to calculate the step size, now an examination of the step size have to be performed to minimize the objective function along a search direction. And lastly to calculate the conjugate direction the Fletcher-Reeves ( $B^{FR}$ ) and Polak-Ribiere ( $B^{PR}$ ) formulas are used.

$$B_{(k)}^{FR} = \frac{\mathbf{r}_{(k)}^T \mathbf{r}_{(k)}}{\mathbf{r}_{(k-1)}^T \mathbf{r}_{(k-1)}},$$

$$B_{(k)}^{PR} = \frac{\mathbf{r}_{(k)}^T (\mathbf{r}_{(k)} - \mathbf{r}_{(k-1)})}{\mathbf{r}_{(k-1)}^T \mathbf{r}_{(k-1)}},$$
(51)

the subscript  $k$  means the iteration and  $r$  the vector of residual. Figure 50 summarizes the nonlinear preconditioned CG algorithm.

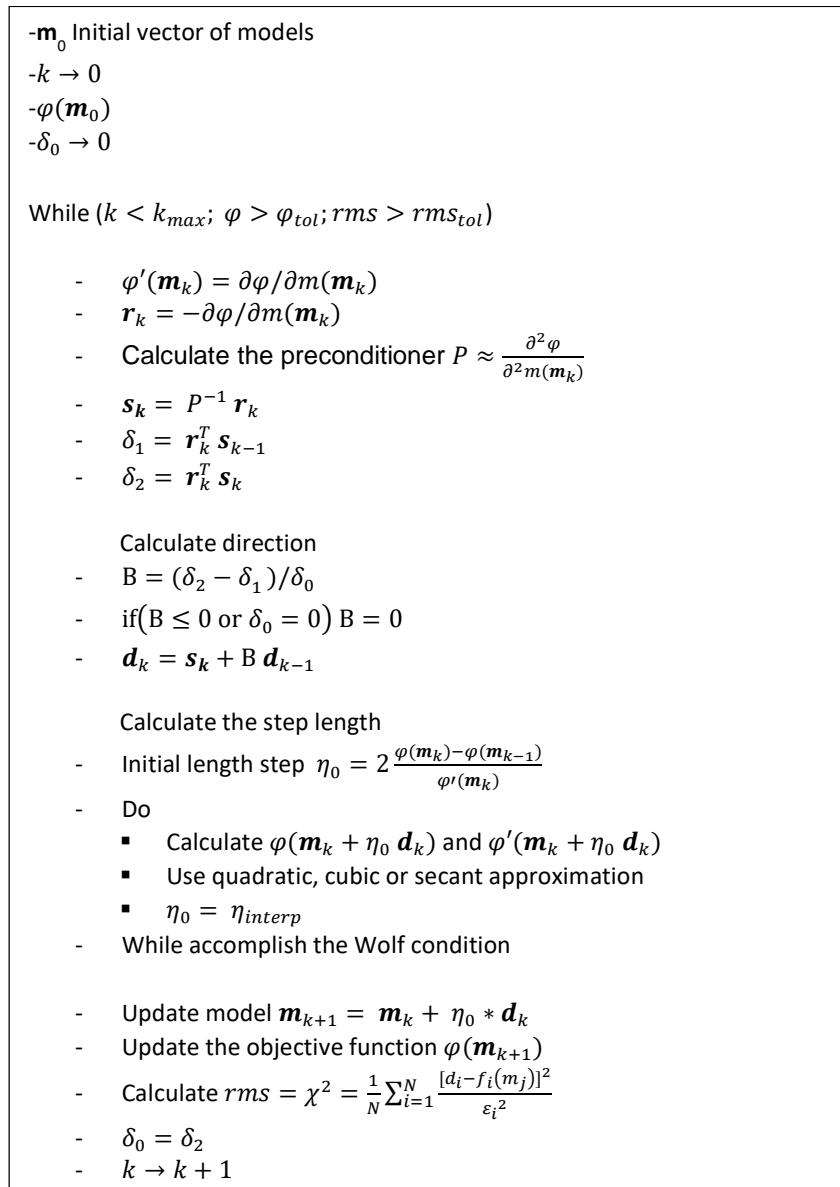


**Figure 50. CG Algorithm.** Preconditioned conjugate gradient method algorithm used to optimize the objective function.

In the previous figure,  $k_{max}$  is the maximum number of iteration,  $\varphi_{tol}$  is the tolerance of convergence of the objective function,  $rms_{tol}$  is the tolerance of fitting of the geophysical data, and  $\varepsilon^2$  is the standard deviation. The first iteration calculates the steepest descent method ( $B = 0$ ); and the conjugate direction is restarted when  $B \leq 0$ . To calculate the Polak-Ribiere formula  $\delta_1 = 0$ . The initial step length is chosen interpolating a quadratic function to the objective function (Nocedal and Wright, 2006), then a loop is done to search the optimal step length that accomplish the Wolf condition. For one iteration of this loop, different step lengths  $\eta_0$  are computed using cubic, quadratic or secant approximations. Finally the model is update with the new direction and the optimal step length, with the new model a new objective function is calculated. All the process is repeated until the convergence parameters are achieved. The most costly process is the search of the length step the others process only require a matrix vector multiplication.

#### A6.4 Test of CG algorithm

To prove the conjugate gradient algorithm I use the damping function (Equation 48) and its respective derivative function,

$$\frac{\partial \varphi}{\partial m} = 2\alpha_j C_{m_j}^{-1} (m_j^p - m_j). \quad (52)$$

Due to its linearity, it has to be solved in one iteration with the step length  $\eta_0 = 0.5$  for the initial step and all the approximations (secant, quadratic and cubic). The results are shown in Figure 51.

#### A6.5 Smoothness term test

The next test is to demonstrate the performance of the smoothness term, to prove this, the objective function and its derivative are defined as

$$\begin{aligned} \varphi &= \alpha_j \left\| m_j^p - m_j \right\|_{C_{m_j}^{-1}}^2 + \beta_j \left\| D m_j \right\|_{C_{D_j}^{-1}}^2, \\ \frac{\partial \varphi}{\partial m} &= 2\alpha_j C_{m_j}^{-1} (m_j^p - m_j) + 2\beta_j D^T C_{D_j}^{-1} m_j. \end{aligned} \quad (53)$$

The idea of this test is to get a solution with smoother models when the value of parameter  $\beta$  increases. A graphical example is exposed in Figure 52 for a first derivative operator,  $\alpha = 1$  and  $\beta = 1 \times 10^{-3}$ . This figure shows the solution is reached with smooth models.

As the objective models only changes in z-direction, the Figure 53 was made to summarize different tests of smoothness with a first derivative operator. All the experiments were gotten with a fixed alpha ( $\alpha = 1$ ). Each color in the curve means that the code converge to a solution for different parameters  $\beta$ 's. When the values of  $\beta$  are greater than  $\alpha$  the smoothness dominates the final models. The orange curve is the most representative example; because it is almost constant in all the model and this value is the average of the objective model values.

The same example is exposed in Figure 54, but in this case a second derivative operator was used. One can notice that it is more difficult get a homogenous model than in the previous example, however the curves start to deflect in the discontinuity zone.

## A6.6 Conjunction term test

The last part to prove is the conjunction term, to do this the equation 50 is added to expression 53, therefore the objective function and its derivatives are defined as

$$\begin{aligned} \varphi &= \alpha_j \left\| m_j^p - m_j \right\|_{C_{m_j}^{-1}}^2 + \beta_j \left\| D m_j \right\|_{C_{D_j}^{-1}}^2 + \gamma_{jk} \left\| \tau(m_j, m_k) \right\|_{C_{\gamma_{jk}}^{-1}}^2 \\ \frac{\partial \varphi}{\partial m} &= 2\alpha_j C_{m_j}^{-1} (m_j^p - m_j) + 2\beta_j D^T C_{D_j}^{-1} m_j + 2\gamma_{jk} \frac{\partial \tau(m_j, m_k)}{\partial m_l} C_{\gamma_{jk}}^{-1} \tau(m_j, m_k) \end{aligned} \quad (54)$$

and the derivative of the cross-gradient function as:

$$\frac{\partial \tau(m_j(x, y, z), m_k(x, y, z))}{\partial m_l(\xi, v, \zeta)} = \frac{\partial [\nabla m_j(x, y, z)]}{\partial m_l(\xi, v, \zeta)} \times \nabla m_k(x, y, z) + \nabla m_j(x, y, z) \times \frac{\partial [\nabla m_k(x, y, z)]}{\partial m_l(\xi, v, \zeta)}. \quad (55)$$

With some algebra the derivative of the objective function for n-models is expressed as:

$$\frac{\partial \varphi_{joint}}{\partial m_l(\xi, v, \zeta)} = 2 \sum_{j=1}^{n_{Models}} \gamma_{jl} \nabla \cdot \left[ \nabla m_j(\xi, v, \zeta) \times C_{\gamma_{jl}}^{-1}(\xi, v, \zeta) \tau(m_j(\xi, v, \zeta), m_l(\xi, v, \zeta)) \right]. \quad (56)$$

In this formula  $\xi, \nu, \zeta$  are the position in x, y, z respectively where the derivative is evaluated, the subscript  $l$  is the model property which is going to share the geometrical similarity with other models, the  $nModels$  variable means the total numbers of model to be optimized.

To see the performance of the cross-gradient formula in the code, I chose only two models ( $nModels=2$ ). The purpose is check if one model pass the structural characteristics to other model. The initial Model 1 has the same change of values in the z-direction that has been used in the previous tests with a slight smoothing. Model 2 is more elaborated, it was calculated with an arctangent function in the x- and z-direction but constant in the y-direction. The models can be observed in detail in Figure 55. The idea to elaborate a complex model was to have a structure with second derivative is also to share the structural characteristics to Model 1.

As the idea is to observe the performance of the conjunction term, hence the conjunction parameter is  $\gamma_{12} = 100$ , the smooth parameter for both models is  $\beta = 1$ , and the damping parameter in Model 1 is  $\alpha_1 = 0.01$  and Model 2 is  $\alpha_2 = 1,000$ . With this damping parameters the Model 1 is the only that is going to change in each iteration while Model 2 will not change.

Figure 58 describes the changes of the models in each iteration. In iteration 10 (Figure 56a) Model 1 changes in the zone where both models share structural changes. For the next iterations, the changes in Model 1 are going to extend in the change direction of Model 2. The values of Model 1 are decreasing in that zone.

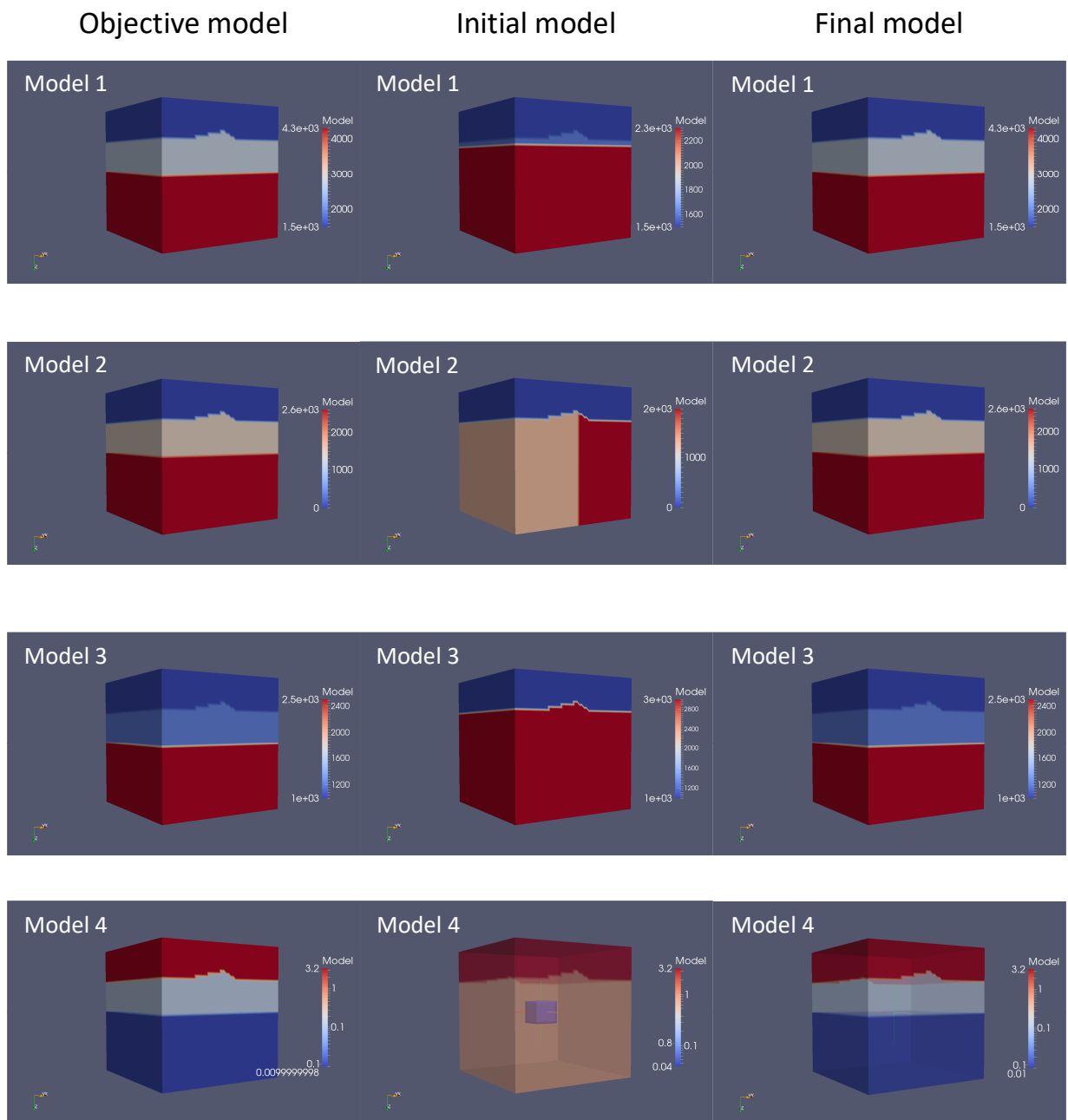


**Figure 51. Regularization test.** The first column are the objective models to be reached, the second column are the initial models and the last column are the solutions after one iteration in the conjugate gradient algorithm. Notice that, the first column and the third columns have the same models. The values given in the models has no a physical meaning.

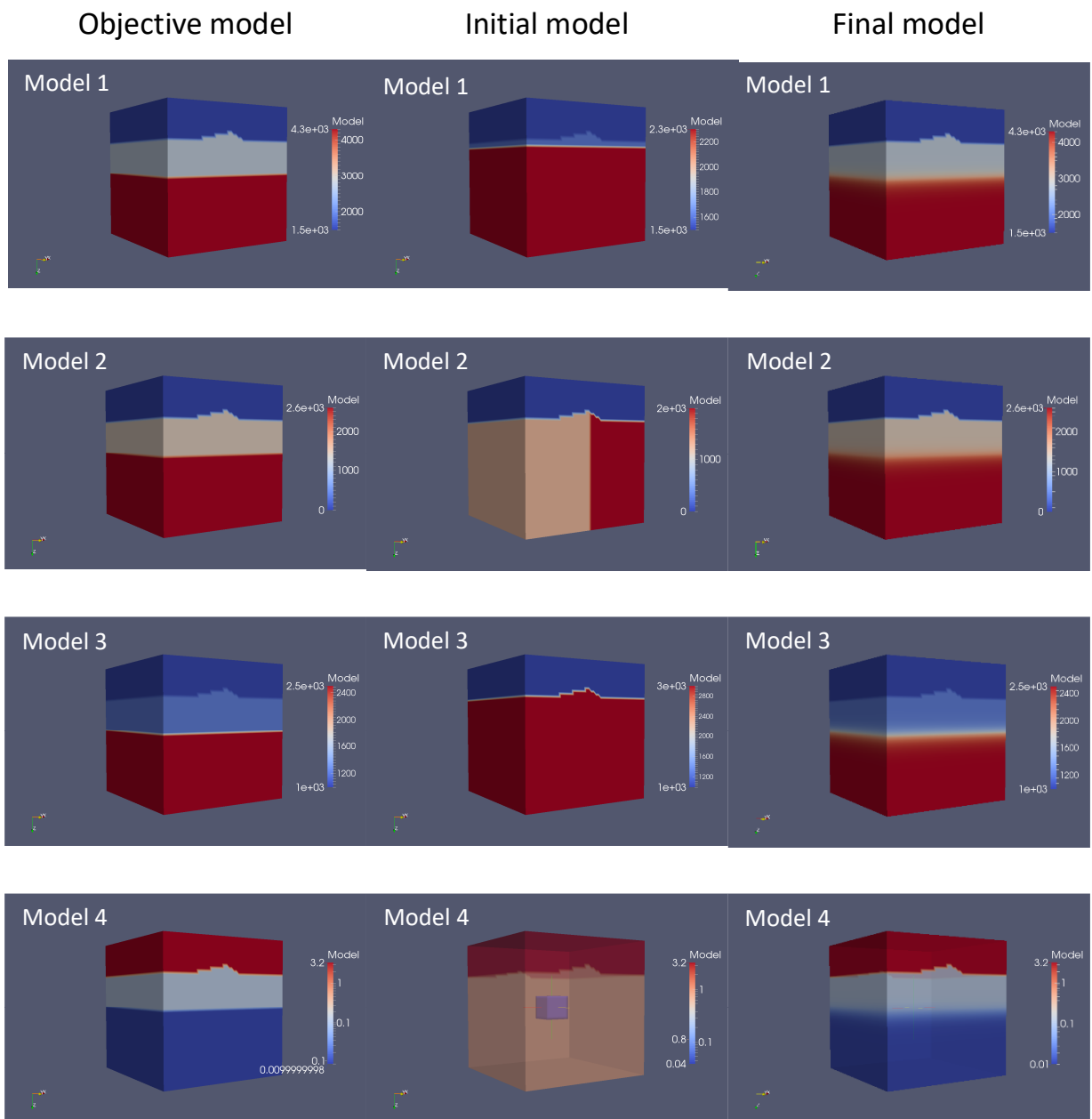


**Figure 52. Smoothness test.** The first column are the objective models to be reached, the second column are the initial models and the last column are the models solutions obtained from the conjugate gradient algorithm using the Equation 53. The operator used in this example was a first derivative operator with  $\beta = 1.0E3$ . Comparing the first and the last column, the objective models are reached but with a smooth transition in the middle of the models, where the values change. The values given in the models has no a physical meaning.

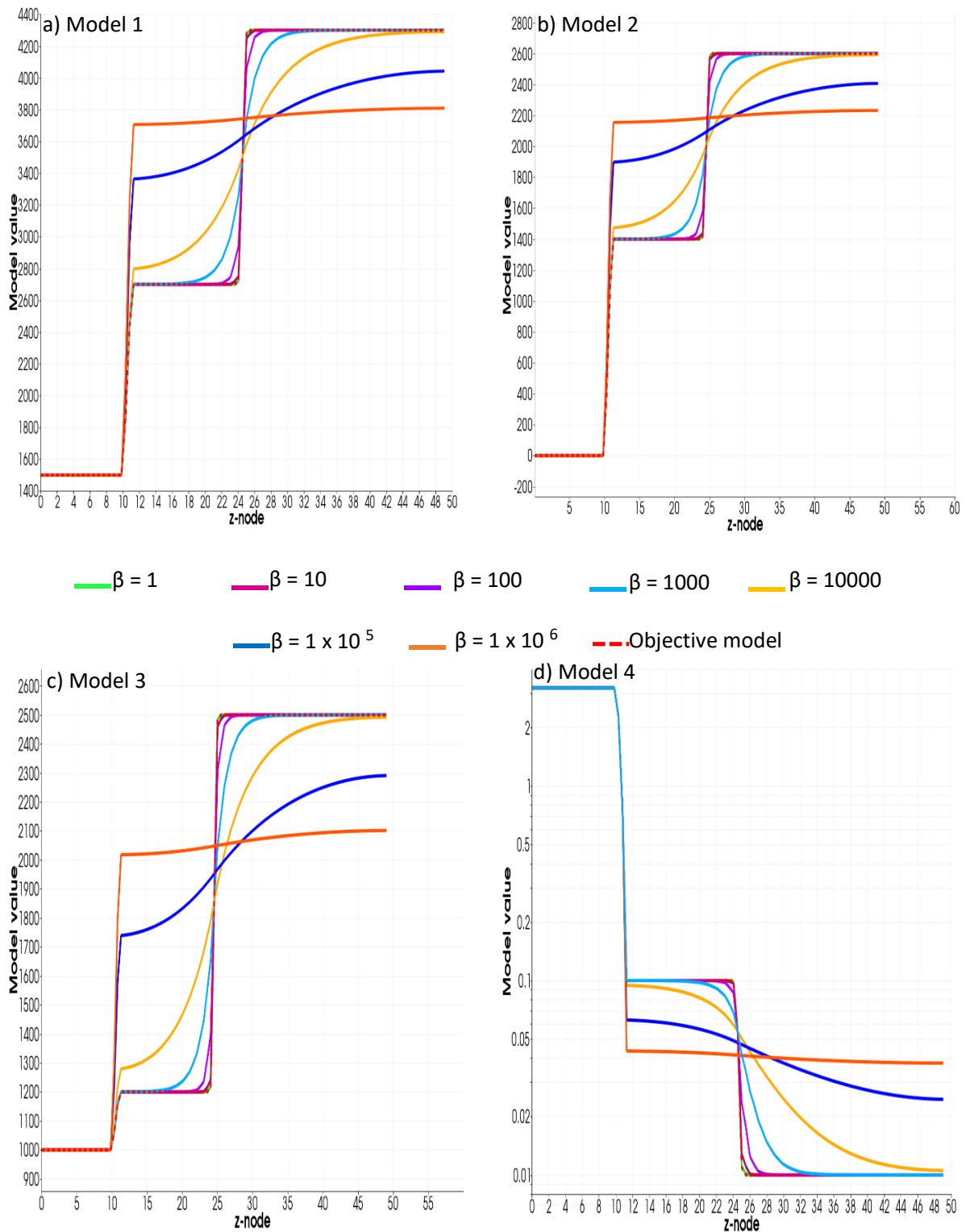


**Figure 53. Smoothness test 1.** Each line is the final model obtained from the conjugate gradient algorithm optimizing the Equation 53 with a first derivative operator and different parameters  $\beta$ 's. When the smooth term of equation 53 increase the final model become smoother, so much that the final model obtained with the largest  $\beta$  is a homogenous model (orange line).

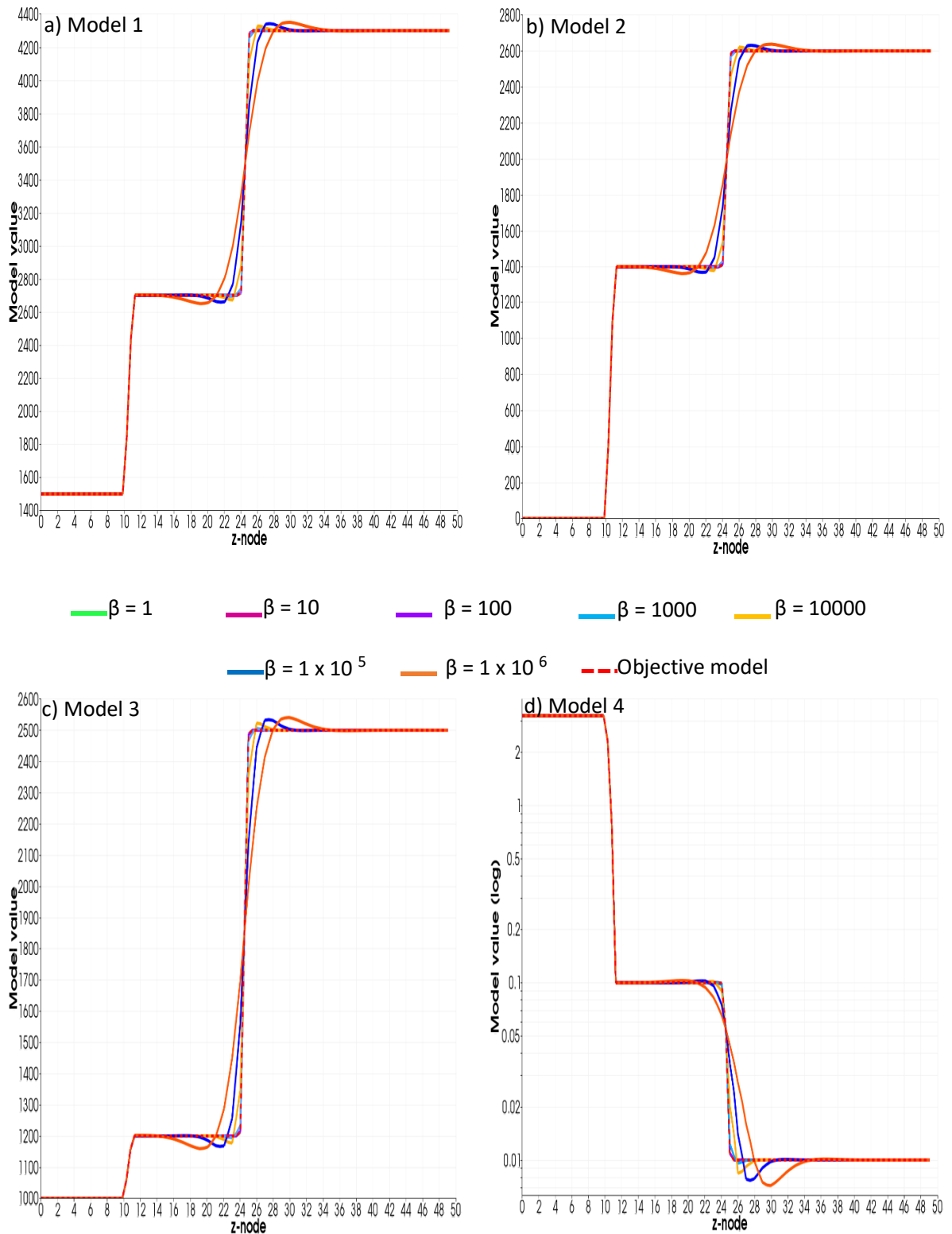


**Figure 54. Smoothness test 2.** Each line is the final model obtained from the conjugate gradient algorithm optimizing the Equation 53 with a second derivative operator and different parameters  $\beta$ 's. The second derivative operator is more robust than the first derivative operator.

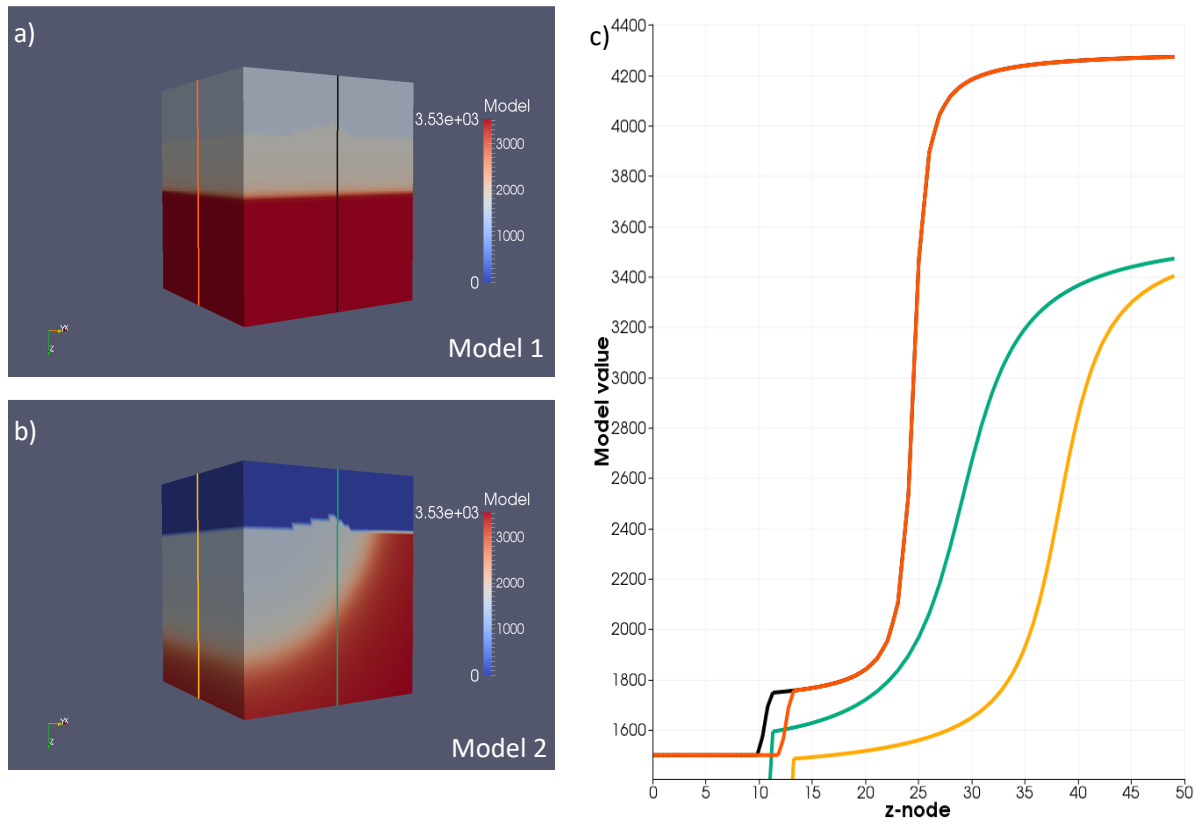


**Figure 55. Initial models of Conjunction test.** a) Model 1, the model proposed is similar to the previous models the only difference is the smooth transition in the middle of the model. b) Model 2, the model was built with an arctangent function in the x- and z-direction but constant in y-direction. c) The value of the curves were extracted from the lines of Model 1 and Model 2 in the z-direction.

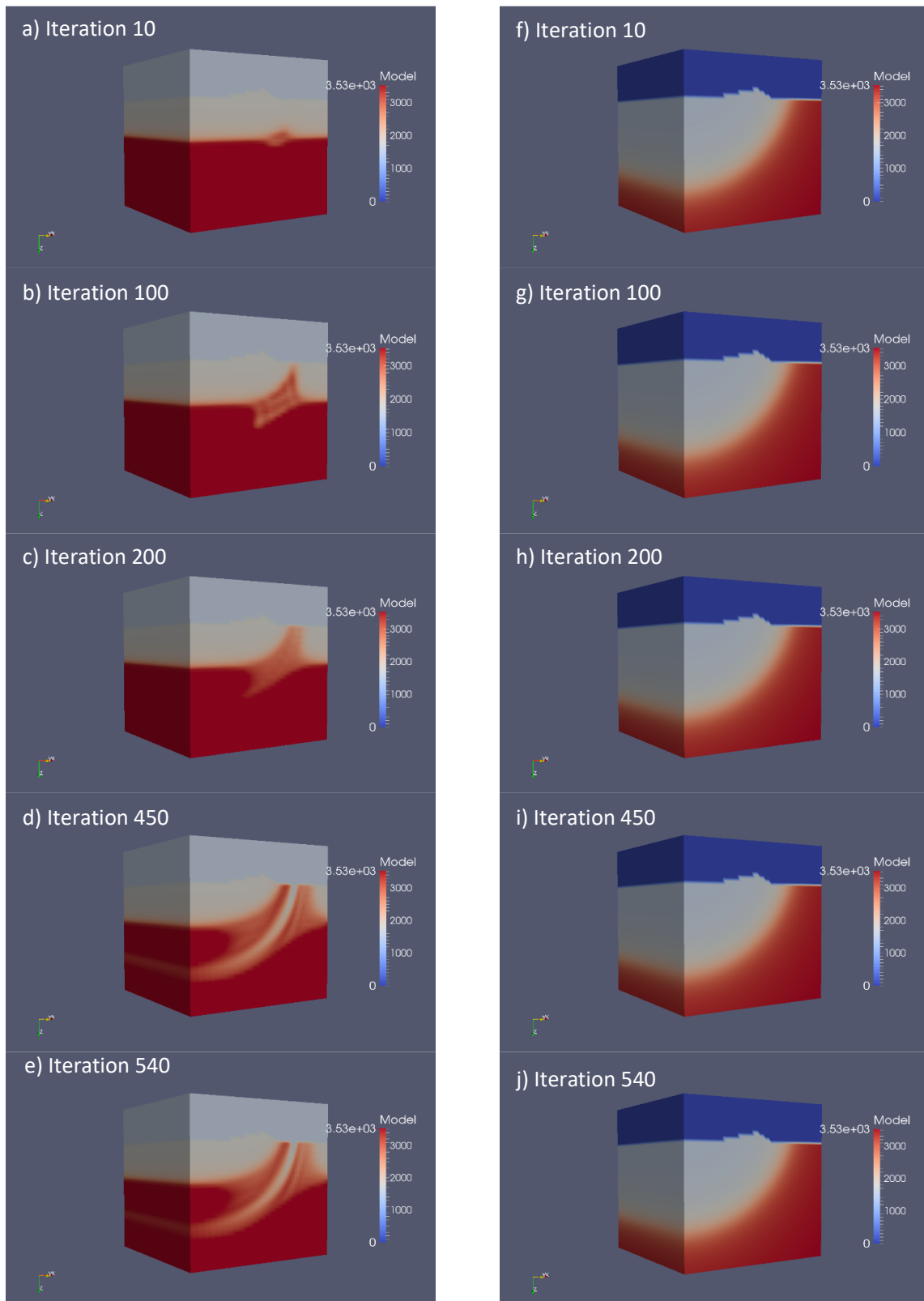


**Figure 56. Conjunction test.** Different iteration to optimize the Equation 54. The parameter used are  $\alpha_1 = 0.01$  for Model 1,  $\alpha_2 = 1000$  in Model 2,  $\beta = 1$  for both models and  $\gamma_{12} = 100$ . The initial are in Figure 55. The objective models are the same that the initial models. The first column is the evolution of Model 1 in each iteration until the reach the solution in 540 iterations.

## Appendix B Boundary Conditions on the interface

---

I will establish here that whenever there is an interface that separates two media with different conductivities the normal component of the electric field must be discontinuous. This is a standard boundary condition that follows from Maxwell's equations (e.g. Grant y West, 1965). Less well known in the geophysical literature, although it is standard in other disciplines, is the physical nature of the discontinuity. The electric field is discontinuous because of a surface density of free charge deposited on the interface. This is also established below using Gauss' law. Let's begin by writing the continuity equation in the frequency domain. The current density  $\mathbf{J}$  and the volumetric charge density  $q$  obey

$$\nabla \cdot \mathbf{J} = -i\omega q . \quad (57)$$

Using Gauss' law this can be written as

$$\nabla \cdot \mathbf{J} = -i\omega\epsilon_0 \nabla \cdot \mathbf{E} . \quad (58)$$

Assuming Ohm's law  $\mathbf{J} = \sigma\mathbf{E}$  this becomes

$$\nabla \cdot \mathbf{J}_T = 0, \quad (59)$$

here  $\mathbf{J}_T = (\sigma + i\omega\epsilon_0)\mathbf{E}$ . Integrating over a given volume we obtain

$$\int_V \nabla \cdot \mathbf{J}_T dv = 0. \quad (60)$$

Using the divergence theorem

$$\int_S \mathbf{J}_T \cdot d\mathbf{a} = 0 . \quad (61)$$

Assuming that the surface is the pillbox of Figure 57, therefore, the previous integral is defined in three surface integrals, two over the top and bottom surfaces and one lateral.

$$\int_{S_1} \mathbf{J}_T \cdot d\mathbf{a} + \int_{S_2} \mathbf{J}_T \cdot d\mathbf{a} + \int_{S_L} \mathbf{J}_T \cdot d\mathbf{a} = 0 . \quad (62)$$

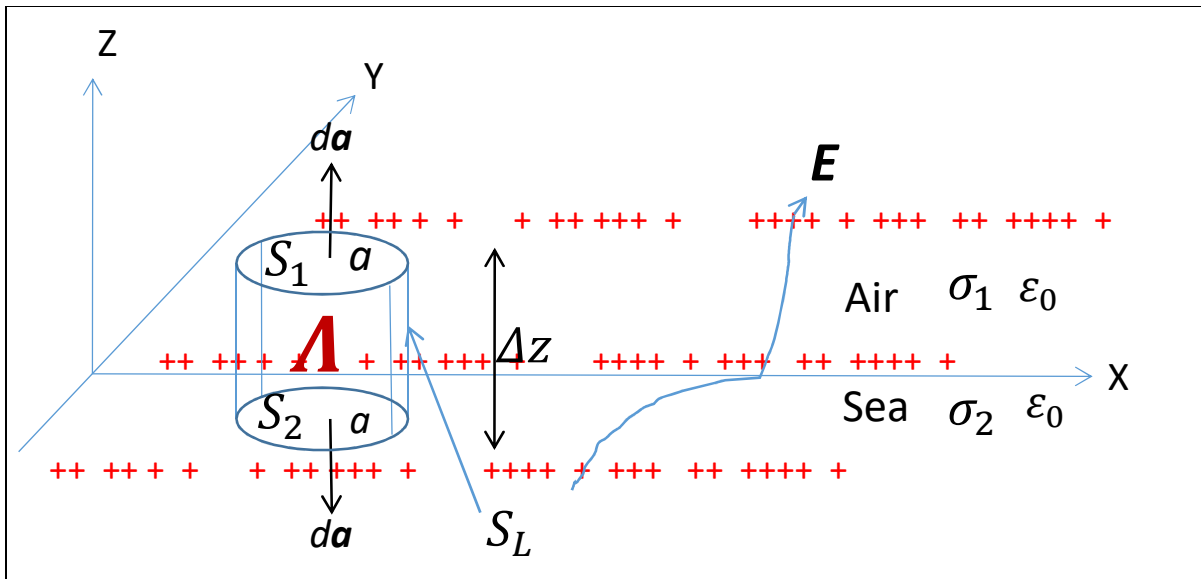


**Figure 57. Boundary condition.** Pillbox used for establishing the boundary condition and its physical nature at the air-sea interface. The plus signs represent electric charges deposited on top of the sea. The symbol  $\Delta$  stands for the surface density of charge and has the units of Coulombs/square meter.

Taking the dot product this reduces to

$$\int_{S_1} J_{z1} da - \int_{S_2} J_{z2} da + \int_{S_L} J_{zL} da = 0. \quad (63)$$

Supposing that the radius of the pill box is small, this can be simplified with the integrals over  $S_1$  and  $S_2$  to products and neglect that over  $S_L$  by assuming  $\Delta z \rightarrow 0$ . The result is

$$(\sigma_1 + i\omega\epsilon_0)E_{z1}a = (\sigma_2 + i\omega\epsilon_0)E_{z2}a. \quad (64)$$

Eliminating the area  $a$  the result is independent of the size of the pillbox. That is

$$(\sigma_1 + i\omega\epsilon_0)E_{z1} = (\sigma_2 + i\omega\epsilon_0)E_{z2}, \quad (65)$$

to compare the electric field on both sides of the interface, it is written as:

$$E_{z2} = \frac{\sigma_1 + i\omega\epsilon_0}{\sigma_2 + i\omega\epsilon_0} E_{z1}. \quad (66)$$

Considering that  $\sigma_1 = 10^{-15} S/m$ ,  $\sigma_2 = 3 S/m$  and  $\epsilon_0 = 8.85 \times 10^{-12} F/m$ , and that in marine CSEM the typical frequencies are of the order of 1 Hz, it follows that the vertical electric field just below the sea surface is many orders of magnitude smaller than that just above the sea. In the quasi-static approximation and assuming  $\sigma_1 = 0 S/m$  the vertical field is identically nil. That is  $E_{z2} = 0$ .

In general, for two given media the difference of the two fields is

$$E_{z2} - E_{z1} = \frac{\sigma_1 + i\omega\epsilon_0 - \sigma_2 + i\omega\epsilon_0}{\sigma_2 + i\omega\epsilon_0} E_{z1}, \quad (67)$$

equivalently

$$E_{z2} - E_{z1} = \frac{\sigma_1 - \sigma_2}{\sigma_2 + i\omega\epsilon_0} E_{z1}. \quad (68)$$

Multiplying by the conjugate of the complex number in the denominator and nominator it is obtained

$$E_{z2} - E_{z1} = \frac{\sigma_1 - \sigma_2}{\sigma_2 + i\omega\epsilon_0} \frac{\sigma_2 - i\omega\epsilon_0}{\sigma_2 - i\omega\epsilon_0} E_{z1}, \quad (69)$$

equally

$$E_{z2} - E_{z1} = \frac{\sigma_1 - \sigma_2}{\sigma_2 + i\omega\epsilon_0} \frac{\sigma_2 - i\omega\epsilon_0}{\sigma_2 - i\omega\epsilon_0} E_{z1}, \quad (70)$$

explicitly

$$E_{z2} - E_{z1} = \frac{(\sigma_1 - \sigma_2) \sigma_2}{\sigma_2^2 + (\omega\epsilon_0)^2} E_{z1} - i \frac{(\sigma_1 - \sigma_2) \omega\epsilon_0}{\sigma_2^2 + (\omega\epsilon_0)^2} E_{z1}. \quad (71)$$

In the quasi-static approximation

$$E_{z2} - E_{z1} = \frac{\sigma_1 - \sigma_2}{\sigma_2} E_{z1}. \quad (72)$$

The analysis above leads to conclude that whenever there is an interface that separates two media with different conductivities, the normal components of the electric field are different on either side of the interface. However, the analysis does not enter into the nature of the discontinuity. That is, into what is happening physically at the interface. This is reviewed below using Gauss' law. I begin by writing Gauss' law in the standard form using the displacement vector  $\mathbf{D}$  as

$$\nabla \cdot \mathbf{D} = q, \quad (73)$$

equivalently

$$\epsilon_0 \nabla \cdot \mathbf{E} = q. \quad (74)$$

Integrating over a given volume we have

$$\epsilon_0 \int_V \nabla \cdot \mathbf{E} dv = \int_V q dv. \quad (75)$$

Applying the divergence theorem on the left hand side and writing the volumetric density  $q = \Lambda/\Delta z$ , where  $\Lambda$  is the surface density, there results

$$\epsilon_0 \int_{S_1} \mathbf{E} \cdot d\mathbf{a} + \epsilon_0 \int_{S_2} \mathbf{E} \cdot d\mathbf{a} + \epsilon_0 \int_{S_L} \mathbf{E} \cdot d\mathbf{a} = \int_V \frac{\Lambda}{\Delta z} dadz. \quad (76)$$

Performing the dot product on the left hand side, it can be written as:

$$\epsilon_0 \int_{S_1} E_{z1} da - \epsilon_0 \int_{S_2} E_{z2} da + \epsilon_0 \int_{S_L} E_L da = \int_V \frac{\Lambda}{\Delta z} dadz. \quad (77)$$

Assuming that the electric field is uniform over the top and bottom of the pillbox we can take the fields outside de integral sign. The same applies for the surface density. That is

$$\epsilon_0 E_{z1} \int_{S_1} da - \epsilon_0 E_{z2} \int_{S_2} da = \frac{\Lambda}{\Delta z} \int_V dadz. \quad (78)$$

Integrating on both sides and noting that the volume integral is simply  $a\Delta z$  there results

$$\epsilon_0 E_{z1} a - \epsilon_0 E_{z2} a = \Lambda a, \quad (79)$$

solving for the surface charge density, it shows that

$$\Lambda = \epsilon_0 E_{z1} - \epsilon_0 E_{z2} . \quad (80)$$

Formally we should take the limit as both the radius and the height of the pillbox tend to zero but in this case the result is obvious. Finally, since the vertical component of the electric field just below the surface of the sea  $E_{z2}$  is nil, we have

$$\Lambda = \epsilon_0 E_{z1} . \quad (81)$$